(1)

NASA CONTRACTOR REPORT



NASA CR-1311

NASA CR-1311
COPY ON MICROFICHE
REFERENCE COPY
DO NOT CHARGE OUT
N69-23450

INITIAL RADIO-FREQUENCY GAS HEATING EXPERIMENTS TO SIMULATE THE THERMAL ENVIRONMENT IN A NUCLEAR LIGHT BULB REACTOR

MAY 5 1969
MCDONNELL LIBRARY
DEPT. 218

by John S. Kendall, Ward C. Roman, and Paul G. Vogt

Prepared by
UNITED AIRCRAFT CORPORATION
East Hartford, Conn.
for

NATIONAL AERONAUTICS AND SPACE ADMINISTRATION • WASHINGTON, D. C. • APRIL 1969

NASA CR-1311

INITIAL RADIO-FREQUENCY GAS HEATING EXPERIMENTS TO SIMULATE THE THERMAL ENVIRONMENT IN A NUCLEAR LIGHT BULB REACTOR

By John S. Kendall, Ward C. Roman, and Paul G. Vogt

Distribution of this report is provided in the interest of information exchange. Responsibility for the contents resides in the author or organization that prepared it.

Issued by Originator as Report No. G-910091-17

Prepared under Contract No. NASw-847 by
UNITED AIRCRAFT CORPORATION
East Hartford, Conn.

for

NATIONAL AERONAUTICS AND SPACE ADMINISTRATION

For sale by the Clearinghouse for Federal Scientific and Technical Information
Springfield, Virginia 22151 – CFSTI price $3.00

Preceding Page Blank

Preceding Page Blank

FOREWORD

An exploratory experimental and theoretical investigation of gaseous nuclear rocket technology is being conducted by the United Aircraft Research Laboratories under Contract NASw-847 with the joint AEC-NASA Space Nuclear Propulsion Office. The Technical Supervisor of the Contract for NASA is Captain C. E. Franklin (USAF). Results of portions of the investigation conducted during the period between September 15, 1967 and September 15, 1968 are described in the following five reports (including the present report) which comprise the required eighth Interim Summary Technical Report under the Contract:

1. Kendall, J. S., W. C. Roman, and P. G. Vogt: Initial Radio-Frequency Gas Heating Experiments to Simulate the Thermal Environment in a Nuclear Light Bulb Reactor. United Aircraft Research Laboratories Report G-910091-17, September 1968. (present report)

2. Mensing, A. E. and L. R. Boedeker: Theoretical Investigation of R-F Induction Heated Plasmas. United Aircraft Research Laboratories Report G-910091-18, September 1968.

3. Krascella, N. L.: Theoretical Investigation of the Composition and Line Emission Characteristics of Argon-Tungsten and Argon-Uranium Plasmas. United Aircraft Research Laboratories Report G-910092-10, September 1968.

4. Marteney, P. J., A. E. Mensing, and N. L. Krascella: Experimental Investigation of the Spectral Emission Characteristics of Argon-Tungsten and Argon-Uranium Induction Heated Plasmas. United Aircraft Research Laboratories Report G-910092-11, September 1968.

5. Latham, T. S.: Nuclear Studies of the Nuclear Light Bulb Rocket Engine. United Aircraft Research Laboratories Report G-910375-3, September 1968.

Preceding Page Blank

Initial Radio-Frequency Gas Heating Experiments to Simulate the Thermal Environment in a Nuclear Light Bulb Reactor

TABLE OF CONTENTS

	Page
SUMMARY	1
RESULTS	2
INTRODUCTION	4
DESCRIPTION OF PRINCIPAL EQUIPMENT	5
UARL 1.2-Megw R-F Induction Heater	5
Plasma Starting System	6
Particle Seeding System	7
DESCRIPTION OF TEST PROCEDURES AND PLASMA DIAGNOSTICS	9
Test Procedures	9
Plasma Diagnostics	10
DISCUSSION OF RESULTS	13
Tests Employing Radiant Energy Source Configurations	13
Tests with Transparent Walls Adjacent to the Radiant Energy Source	19
REFERENCES	23
LIST OF SYMBOLS	25

TABLE OF CONTENTS (Continued)

Page

APPENDIXES

I - TRANSPARENT-WALL MODEL DEVELOPMENT PROGRAM. 28

II - SUMMARY OF PRELIMINARY R-F EXPERIMENTS. 30

III - WATER VORTEX TESTS WITH LUCITE MODELS 34

IV - SUPPORTING EXPERIMENTAL INVESTIGATION OF CONTAINMENT IN CONSTANT-TEMPERATURE RADIAL-INFLOW VORTEXES 36

TABLES. 44

FIGURES 46

Initial Radio-Frequency Gas Heating Experiments to Simulate the Thermal Environment in a Nuclear Light Bulb Reactor

SUMMARY

Initial experiments were conducted to develop an intense radiant energy source which would eventually be capable of producing radiant energy fluxes equal to those expected in a full-scale nuclear light bulb engine. The test program was conducted using the UARL 1.2-megw r-f induction heater at d-c input power levels up to approximately 250 kw to supply energy to the simulated fuel-containment region of a vortex. The primary objective of the experimental program was to determine the effect of various parameters on the power radiated from the vortex, the power deposited in the peripheral wall of the vortex tube, and the power carried away by convection from the vortex. Both argon discharges with no seed and argon discharges seeded with submicron carbon and tungsten particles were employed. Tests were conducted at discharge pressures up to 6.0 atm abs and with up to 85 kw of power deposited in the discharge; of this, 35 kw was radiated through a water-cooled transparent wall surrounding the discharge. The 35 kw of radiant energy represents a radiant energy flux of about 12.0 kw/in.^{2} (1.86 kw/cm^2), which corresponds to an equivalent black-body radiating temperature of 7600 R. For comparison, the design radiant flux level at the edge of the fuel-containment region of a representative nuclear light bulb engine is 178 kw/in.^{2}, which corresponds to an equivalent black-body radiating temperature of 15,000 R.

A second objective of the investigation was to design, fabricate, and test thin, internally-cooled transparent-wall models. Several different types of models were tested around the radiant energy source. Additional supporting research was conducted using the UARL 80-kw r-f induction heater, the two-component isothermal gas vortex test facility, and various small water vortex models. This supporting research is described in the appendixes of the report.

RESULTS

1. Initial development of the intense radiant energy source using the UARL 1.2-megw r-f induction heater resulted in attainment of the following levels of performance for unseeded argon discharges:

   a. The maximum power deposited in the r-f discharge was 85 kw. The discharge diameter obtained from photographs was 0.57 in. as compared with the 2.28-in.-dia fused silica peripheral wall surrounding the discharge. The corresponding power density was approximately 220 kw/in.^{3}.

   b. The maximum measured radiated power was 35 kw. Based on estimates of the discharge surface area obtained from photographs, the corresponding radiant energy flux was approximately 12.0 kw/in.^{2}, which corresponds to an equivalent black-body radiating temperature of 7600 R. The radiated power was measured after the radiation passed through two fused silica peripheral walls and an intermediate layer of cooling water. An additional 19 kw was deposited in the cooling water due to the combined effects of radiation absorption, conduction, and convection from the light source.

2. For unseeded argon discharges, simultaneous increases in pressure and r-f discharge power produced the largest increases in the percent of discharge power that was radiated. For example, for constant argon flow rate, simultaneous increases in pressure from 2 to 6 atm abs and in discharge power from 14.4 to 34.1 kw caused an increase in percent power radiated from 33 to 45 percent. For constant discharge pressure, simultaneous increases in argon flow rate and discharge power caused no change in the percent power radiated. At 6 atm abs, the percent power radiated remained constant at 40 percent as the argon flow rate and discharge power were simultaneously increased from 0.01 to 0.25 lb/sec and 24 to 85 kw, respectively.

3. During a test in which a small quantity of submicron carbon particles was injected into an argon discharge, the measured radiation from the discharge was approximately 60 percent greater than that measured in a corresponding test with no carbon particles. No significant change occurred in the amount of heat transfered to the end walls or to the peripheral wall of the test chamber.

4. Significant progress was made in the development of internally cooled transparent-wall models similar to the walls proposed for the nuclear light bulb engine. Models having a 1.26-in. ID and wall thicknesses of 0.060 and 0.020 in. were fabricated entirely from fused silica. These models were of two general types: models employing concentric cylinders to form the peripheral wall with end-wall injection to

drive the argon vortex, and models employing up to 46 axial tubes to form the peripheral wall with peripheral-wall injection to drive the argon vortex. In addition, model components having wall thicknesses of 0.010 in. were fabricated and techniques were developed for assembling complete models from these thinner-wall components.

5. Tests with transparent-wall models surrounding the intense radiant energy source resulted in attainment of the following levels of performance:

a. The maximum power deposited in the r-f discharge for models employing concentric cylinders to form the peripheral wall with end-wall injection to drive the argon vortex was about 26 kw; the maximum power radiated through the wall was about 8.3 kw at 3.8 atm abs. These models had wall thicknesses of 0.060 in. and inside diameters of 1.26 in. The discharge was approximately 1.0 in. in diameter. The maximum power deposited was limited by high heat transfer at the peripheral wall caused by turbulence attributable to the end-wall injection method used to drive the vortex.

b. The maximum power deposited in the r-f discharge in tests of a model employing axial tubes to form the peripheral wall and with peripheral-wall injection to drive the vortex was about 24 kw; the corresponding power radiated through the wall was 5.1 kw at 5.3 atm abs. This model had a wall thickness of 0.020 in. and an inside diameter of 1.26 in. The maximum discharge power was limited by heat transfer to the uncooled vortex injection tubes which caused localized melting. In future tests at higher powers employing models of this type, steps must be taken to improve the cooling of the vortex injection system and to reduce the diameter of the discharge relative to the model diameter so as to reduce the amount of heat transferred by conduction and convection from the surface of the discharge to the peripheral wall of the model.

INTRODUCTION

An experimental and theoretical investigation of gaseous nuclear rocket technology is being conducted by the United Aircraft Research Laboratories under Contract NASw-847 administered by the joint AEC-NASA Space Nuclear Propulsion Office. This investigation is presently directed toward the nuclear light bulb engine concept. The engine would consist of seven unit cavities similar to the one shown schematically in Fig. 1. In this concept, heat is transferred from gaseous fissioning fuel to seeded hydrogen propellant through an internally-cooled transparent wall. A transparent buffer gas such as neon is injected at the inner surface of the transparent wall to form a vortex which isolates the fuel from the wall. Because of the high temperatures obtainable in the gaseous fuel, engines of this type can theoretically provide specific impulses of 1500 to 3000 sec and thrust-to-weight ratios greater than one. The concept is also attractive because the physical barrier between the fuel and propellant offers the possibility of perfect containment of fuel and fission products. Additional details of the nuclear light bulb concept are discussed in Ref. 1, and the fluid mechanics requirements are discussed in Ref. 2.

The research program discussed in this report is concerned with simulating the fluid mechanical containment of the gaseous nuclear fuel, transfer of energy from the simulated fuel to the propellant, and fabrication and testing of internally-cooled transparent walls. Major emphasis was placed on use of the UARL 1.2-megw r-f induction heater to develop a non-nuclear light source that will provide radiant energy fluxes equal to those expected for the engine. Major emphasis was also placed on development of techniques to provide information for fabricating thin, transparent-walled models of walls similar to those proposed for the actual engine. These efforts are designed to lead to heating of a simulated propellant at the full-scale radiant energy flux with a transparent-wall model between the light source and the simulated propellant. Previous investigations of heat transfer to seeded gases are reported in Refs. 3 and 4. However, both of the investigations employed energy sources having radiant energy fluxes much less than the radiant energy fluxes obtained in the tests described in the following sections.

The primary objectives of the research reported herein were: (1) to determine the factors that influence the size and power deposited in confined gas vortex r-f discharges, (2) to increase the percentage of total discharge power that is radiated, and (3) to design, fabricate and test several different types of thin, internally-cooled, transparent-wall models around the radiant energy source and to determine their operating limitations.

DESCRIPTION OF PRINCIPAL EQUIPMENT

The principal equipment employed in the gas discharge tests discussed herein consisted of the UARL 1.2-megw r-f induction heater, various model configurations, the plasma starting system, and the particle seeding system. A complete description of all of this equipment, except the models, is presented in the following subsections. A summary of the various model geometries employed in the gas discharge tests is presented in the section entitled DISCUSSION OF RESULTS. Descriptions of transparent-wall models and test equipment employed in preliminary gas discharge tests, and test equipment employed in supporting fluid mechanics tests, are presented in Appendixes I through IV.

UARL 1.2-Megw R-F Induction Heater

The UARL 1.2-megw r-f induction heater was constructed during 1966 and 1967 as part of a Corporate-sponsored program. This r-f heater was designed to deposit approximately 500 kw of r-f power into a gas discharge approximately 0.4 in. in diameter and 2.0 in. in length. A block diagram showing the primary components of the heater is presented in Fig. 2. The r-f output power is provided by two power amplifier tubes connected in a push-pull configuration which drive a resonant tank circuit of unique design. The grids of the power amplifier tubes are driven by the amplified output of a variable-frequency oscillator at the resonant frequency of the tank circuit. The power levels indicated within the blocks on Fig. 2 correspond to the maximum rated r-f output power for each component. Note that, for each power amplifier tube, 600 kw of d-c input power is required to produce 440 kw of r-f output power. The maximum total d-c input power to the power amplifiers employed in gas discharge tests during this program was about 250 kw. However, as part of a Corporate sponsored research program, the heater has been run routinely at input d-c power levels exceeding 400 kw. To date, the maximum power deposited in a salt water load is 115 kw and the maximum power deposited in a gas discharge is 85 kw (see following section). Details of the resonator section (tank circuit) are shown in Fig. 3. The resonator section consists of two arrays of ten vacuum capacitors, each of which is connected in parallel with a single-turn, silver-plated, 3.06-in.-dia work coil. Each work coil consists of five internally-cooled copper tubes which were soldered together to form a single structure prior to being silver plated (see Fig. 3b). The ends of the capacitors and both work coils are water cooled. R-F chokes are installed in the cooling water lines to prevent current leakage to ground. Figure 3b shows the work coils with a model configuration installed. The gas discharge is produced in the region directly under the work coils and is usually located on the centerline of the coils.

Measurements of important electrical quantities and of cooling water flow rates and temperature rises in certain critical parts of the heater are made during each run to provide information required for performing the overall system energy balance.

Plasma Starting System

The plasma starting system utilizes a d-c arc to provide reliable starting of the gas r-f discharges in tests in the 1.2-megw r-f induction heater. A low power arc discharge is drawn between two electrodes along the centerline of the test chamber between the end walls. The arc is maintained until sufficient coupling of r-f power to the arc plasma occurs to produce a sustained r-f discharge in the test chamber. Figure 4 is a block diagram of the system and Fig. 5 presents photographs of the electrode assemblies which were used. Time sequence photographs of the starting process together with details of the starting system operation are presented in Fig. 6. The electrode composition, size, and shape, electrode insulating materials, d-c current level, position of the electrodes within the test chamber, and speed of electrode withdrawal were all selected to minimize sputtering of material in the test chamber which might result in damage to the transparent walls of the test models.

The electrodes consist of 0.086-in.-OD by 3.5-in.-long rods of 2 percent thoriated tungsten. The electrodes have hemispherical tips. Each electrode was welded to a 1.5-in.-long stainless steel rod which was screwed into the copper drive rod of the starter assembly (see Fig. 5). A ceramic sheath material (Coors AD 99) was used to electrically isolate the electrode starting rods from the test chamber end walls during arc operation. The copper drive rod assembly was electrically isolated from the test chamber end walls by a 0.31-in.-OD by 26-in.-long fused silica tube which was inserted into the end wall assembly. Clearance between the starting rod assembly and the exhaust port in the end wall of the test chamber was provided to allow for removal of hot gases from the test chamber.

To operate the plasma starting system, both electrodes were inserted to the ready-to-start position shown in Fig. 6. In this position Electrode B protrudes 3/16 in. into the test chamber. Electrode A was inserted into the test chamber until it contacted Electrode B. (For the photographs shown in Fig. 6, the contact point of the two electrodes was shifted 7/16 in. from the normal operating location toward Electrode A to permit photographs of the plasma starting process to be taken.) During normal operation the contact point of the electrodes was located near one end wall so that any electrode material that might erode or sputter would be deposited directly on the end wall rather than on the transparent wall of the test chamber. A 50-kw d-c arc power supply was ballasted with a resistor bank to restrict the arc current to less than about 40 amp. This current level was sufficient to ignite and maintain the arc between the electrodes, at test chamber pressures of approximately 1.0 to 2.0 atm, until the r-f discharge was established.

Particle Seeding System

A number of particle seeding systems suitable for use with micron-sized particles are described in Refs. 3 through 7. For this investigation, a particle seeding system utilizing aerodynamic shear (see Ref. 7) to deagglomerate submicron particles was employed. A schematic diagram of the particle seeding system is presented in Fig. 7, and a photograph of the assembled system is shown in Fig. 8a.

Rotating fan blades in the powder storage cannister constantly agitate the particles to minimize agglomeration. Argon carrier gas transports particles from the storage cannister to the dispersal nozzle assembly. In the dispersal nozzle the particles are mixed with a secondary argon flow and the combined streams flow through the dispersal nozzle. The nozzle provides the aerodynamic shear necessary to finely disperse the particles. Downstream of the nozzle, additional argon is added to the dispersed particle stream to minimize the build-up of particles in the transition plenum.

Fiber optic tubes were located downstream of the dispersal nozzle to provide a light path through the transmission duct. The attenuation of a light beam as it passes through the flowing particles is related to the density and particle size distribution of the particles within the duct. The chamber housing the fiber optic tubes was pressurized with argon to reduce the number of particles which enter the chamber and collect on the ends of the fiber optics. However, this technique was not completely effective, and when the fiber optics were used to monitor the particle seed flow the test duration was limited to approximately 30 sec due to deposits of particles in the ends of the fiber optics. To obtain a meaningful indication of the homogenity of the particle stream by this method, the light intensity should be approximately equal to its original value after the flow of particles has ceased. A light intensity trace from a typical test employing carbon particles is shown in Fig. 8b. The trace indicates the amount of light attenuation due to the particle stream. Also, some fluctuation of the particle stream was present as evidenced by the width of the signal trace compared with that of the reference signal (see Fig. 8b).

Tests of the particle seeding system were conducted using submicron tungsten and carbon particles. Electron microscope photographs of particles as sprayed from the particle seeding system are presented in Fig. 9. Samples of the sprayed particles were prepared by passing a glass slide through the particle stream. Samples collected in this manner may not exactly reflect the true distribution of particle sizes in the sprayed stream because the very small particles in the sprayed stream, which always follow the streamlines of the flow, will not be collected on the slide (except for those particles near the stagnation streamline). However, much useful information concerning the presence of large particle agglomerates in the sprayed stream can be obtained using this sampling technique. For the photographs in Fig. 9, the argon flow through the particle seeding system was approximately constant. A photograph taken when the small-

sized carbon particles (particle diameters of 0.004 to 0.012 microns; Carbolac 2) were used is shown in Fig. 9a. There are a few 8-micron-dia agglomerates and numerous smaller agglomerates less than 4 microns in diameter. A photograph taken when medium-sized tungsten particles (particle diameters of 0.02 to 0.06 microns) were used is shown in Fig. 9b. There is at least one large 20-micron-dia agglomerate and a few in the 8-micron-dia range. Another photograph of large-sized carbon particles (particle diameters of 0.250 to 0.462 microns; Sterling MT) is shown in Fig. 9c. There is one large 30-micron-dia agglomerate and several smaller-diameter agglomerates.

The photographs shown in Fig. 9 are consistent with visual observations of the particle stream. In particle seeding tests with the large carbon particles (Sterling MT), fluctuations in the particle stream occurred that were more severe than those which occurred when the tungsten and small carbon particles were tested. When small carbon particles were employed, a relatively uniform flow could be maintained for approximately thirty minutes before random slug flow (puffing) occurred. When tungsten particles were used, relatively uniform flow could be maintained for only fifteen minutes before slug flow occurred. Based on the photographs in Figs. 9a and 9b and visual observations, it was concluded that the small carbon particles produced a more uniform flow than the larger tungsten particles. The presence of the 20-micron-dia agglomerates (see Fig. 9b) and the more numerous but smaller agglomerates shown in Fig. 9a supports this conclusion. Tests of small tungsten particles having diameters of about 0.012 microns are planned.

When the particle seeding system was employed in gas discharge tests in the 1.2-megw r-f induction heater, satisfactory operation was achieved with small carbon particles. However, difficulties were encountered when tungsten particles were used which resulted in repeated plugging of the dispersal nozzle and seed injection duct with agglomerated particles. In the gas discharge tests employing the particle seeding system, the test chamber pressure was equal to 1.8 atm whereas in the tests described above the pressure at the exit of the seed duct was 1 atm. This increased seed exhaust pressure used in gas discharge tests is a possible cause of the difficulties encountered when tungsten particles were used.

DESCRIPTION OF TEST PROCEDURES AND PLASMA DIAGNOSTICS

Test Procedures

A typical gas discharge test was conducted in the following manner. In early tests employing the radiant energy source, the gas discharge was started by evacuating the test chamber to a pressure of approximately 5 to 10 mm Hg abs. Following gas breakdown, the argon weight flow rate was increased until the test chamber pressure reached approximately 1.0 atm. At this point, the r-f drive system was tuned to compensate for the change in resonant frequency due to the presence of the discharge within the r-f coils. With the r-f supply properly tuned, the argon weight flow, test chamber pressure and r-f input power were increased to the level desired for a particular test condition. The r-f input power to the gas is determined by the r-f voltage supplied to the resonator section of the heater and the electrical conductivity of the gas discharge which determines the amount of current drawn. The r-f voltage was set by adjusting the d-c voltage supplied to the power amplifier (see Fig. 2) by means of a saturable reactor in the d-c power supply until the desired r-f voltage was obtained. The r-f voltage supplied to the resonator section was measured with a capacitive type voltage probe.

The primary independent variables in the gas discharge tests are the argon weight flow rate, the test chamber pressure, and the r-f input power. For the tests reported herein, it was not possible to simultaneously fix all of the independent variables except one and maintain a satisfactory discharge over the entire range of test conditions because: (1) the electrical and thermal characteristics of the r-f plasmas are not independent since they both depend on the mechanism of heat dissipation to the environment and (2) the geometrical shape and size of an r-f plasma discharge in a vortex flow field depends on the interaction between the discharge and the magnetic fields which produce the discharge. Due to this interaction, and due to the existence of both stable and unstable operating regions within the range of variables tested, it was usually necessary to vary two of the above variables simultaneously in order to maintain a stable, well defined r-f plasma discharge within the test chamber.

Because of difficulties associated with starting the gas discharge in a vacuum (especially when small-diameter transparent-wall model configurations were employed), the vacuum starting technique was replaced by the plasma starting system described in the preceding section. The d-c arc was used to initiate the gas breakdown at a test chamber pressure of greater than or equal to 1.0 atm.

Gas discharge tests were conducted in the following manner. The weight flow of argon through the test chamber was increased until the desired starting pressure in the test chamber was reached (1.0 to 2.0 atm for the tests reported herein). The r-f drive system was pre-tuned to the proper resonant frequency. Next, the d-c voltage

supplied to the power amplifier was increased to 3.5 kv. At this point the d-c plasma starting system was activated. Following a time delay of 65 msec, during which time the d-c current increases from zero to approximately 40 amp, Electrode A's withdrawal from the test chamber was started (see Fig. 6). The r-f discharge was initiated within approximately 10^{-2} sec after Electrode A began to withdraw. The r-f system was then retuned to compensate for the resonant frequency change due to the presence of the plasma discharge. For tests at low power levels ($Q_T \leq 20$ kw) the electrodes and insulator assemblies were left in their fully retracted positions during tests. At high power levels, the entire electrode assemblies were fully withdrawn from the thru-flow port. Visual observation of the electrode assemblies and tungsten tips after many start-ups indicated negligible erosion. The same electrode tips and assemblies were used repeatedly throughout the test program.

When higher starting chamber pressures and subsequently higher arc voltages are required for future tests, a longer rev time may be required for full transition to the fully established r-f mode. This can be provided with the existing system.

Measurements of the total d-c input power were obtained by monitoring power supply voltage and current. The total power deposited in the discharge was obtained by measuring end-wall and peripheral-wall cooling water flow rates and associated temperature rises. All cooling water and argon weight flow rates were measured with rotameters. In addition, a thermopile radiometer (see following subsection) was used to measure the radiated power escaping from the test chamber. Power dissipated in critical parts of the induction heater was also monitored and an overall energy balance for the system was obtained. In addition to the measurements described above, measurements of spectral emission from the discharge were obtained for a few selected tests.

Plasma Diagnostics

Total Radiation Measurements

A specially constructed radiometer was used to measure the power radiated from the plasma discharge. A block diagram of the radiometer system is presented in Fig. 10a. A synchronous motor drives a chopper wheel containing four apertures. Three apertures contain filters and the remaining one is open. A single filter having upper and lower 50-percent transmission levels of 0.22 and 2.6 microns, respectively, is located behind the chopper wheel. The transmission characteristics of all four filters are shown in Fig. 11. Transmission characteristics, obtained from Ref. 8, for a 0.079-in.-thick layer of water are also shown in Fig. 11. For the tests reported herein, total radiation measurements were obtained in the following wavelength ranges: 0.22 to 1.3, 0.3 to 1.3, 0.72 to 1.3, and 1.0 to 1.3 microns. The lower wavelength cutoff was determined by the 50-percent transmission level of the individual filters

in the radiometer and the upper wavelength cutoff was determined by the 50-percent transmission level of the 0.079-in.-thick water layer which was located between the discharge and the radiometer. A BaF_2 thermopile detector was used. The output of the thermopile was connected to an operational amplifier and displayed on an oscilloscope (see Fig. 10b).

The radiometer was periodically calibrated with a GE-DXW 1000-watt tungsten ribbon lamp with known spectral characteristics. A calibration constant for each wavelength range was determined. The total power radiated from the discharge in each wavelength range was then calculated from the radiometer measurements by assuming uniform radiation in all directions and allowing for the blockage due to the presence of the r-f heater coils. For the case of an ellipsoidal discharge, 54% of the total discharge volume was visible to the radiometer; for the cylindrical discharge, 38% was visible. Radiated power in the 0.22- to 0.3-micron wavelength range was determined by subtracting the power in the 0.30- to 1.3-micron range from the power in the 0.22- to 1.3-micron range. In a similar way, radiated power in the visible (0.30 to 0.72 microns) and near-IR (0.72 to 1.0 microns and 1.0 to 1.3 microns) portions of the spectrum were determined.

Spectral Emission Measurements

The optical system used to obtain spectral emission measurements is shown in Fig. 12. The Jarrell-Ash 0.25-meter Ebert monochromator and EMI 9558 photomultiplier detector were mounted on a traversing table to permit chordwise scans of the discharge to be made. A photograph of the monochromater and traversing table is shown in Fig. 13. The monochromator has 25-micron-wide entrance and exit slits. A 100-micron-wide collimating slit was located 5.3 in. in front of the entrance slit. The wavelength scans were made at 1000 Å/min. The photomultiplier output was processed and recorded on a Visicorder oscillograph. A typical experimental trace of relative intensity as a function of wavelength for argon gas is shown in Fig. 14. All wavelength scans covered the 3500 Å to 8200 Å range, but only those regions in which strong argon lines were found are shown in Fig. 14. The shape of the spectral lines shown in Fig. 14 is only qualitatively correct due to the amount of instrument broadening produced by the monochromator. A 5600 Å filter was placed in front of the monochromator when spectral scans at wavelengths greater than 5600 Å were made to minimize second-order effects from lines at shorter wavelengths.

Determination of Discharge Volume

Because a substantial portion of the discharge region was shielded from view by the r-f heater coils, only an approximation to the true discharge volume can be obtained. The volume of the discharge was determined in the following manner. Several photographs of each discharge were obtained using different neutral density filters. A typical series of photographs is presented in Fig. 15. As shown in this figure, the

measured discharge diameter depended upon the amount of filtering used. The volume of the discharge region was obtained by assuming the discharge to be either an ellipsoid or a cylinder based on visual observations of the discharge region in the vicinity of the test chamber end walls. The discharge volume was then calculated from the apparent discharge diameter as measured from photographs of the discharge.

DISCUSSION OF RESULTS

The gas discharge tests conducted during this program can be separated into two categories. Since the program was developmental in nature, the tests conducted during the latter part of the program are most pertinent to the objectives of the program. These tests are discussed in the main text in the following two sections, "Tests Employing Radiant Energy Source Configurations" and "Tests with Transparent Walls Adjacent to the Radiant Energy Source." Details of the transparent-wall models used in these tests, including discussions of fabrication techniques, fused silica strength characteristics and the results of mechanical tests of model components, are presented in Appendix I. The results of preliminary tests to investigate fluid mechanics techniques for confining the gas discharge and techniques for obtaining r-f gas breakdown and power addition are described in Appendix II. Appendixes III and IV present the results of supporting water vortex and two-component-gas vortex tests, respectively.

Tests Employing Radiant Energy Source Configurations

Gas discharge tests employing radiant energy source configurations were conducted to determine the effects of discharge pressure and total discharge power on the radiating characteristics of confined r-f discharges. Tests were conducted using both unseeded discharges and discharges seeded with small amounts of carbon particles.

Results of Tests with Unseeded Discharges

A sketch of the radiant energy source configuration used in tests with unseeded discharges is presented in Fig. 16 and additional details appear in Table I. This configuration had a 2.28-in.-ID water-cooled peripheral wall and 0.625-in.-dia water-cooled copper end walls. The end walls were 2.0 in. apart and had 0.18-in.-dia thru-flow ports located at their centers. Argon was injected through ten 0.10-in.-ID tubes located near the peripheral wall at one end. The argon flow was removed through the thru-flow ports. Table I also indicates the figures in which the results of tests of each configuration are presented.

Measurements to Determine Temperature

Spectral emission measurements were made to obtain an estimate of the average temperature near the center of typical discharges. The monochromator was aligned so that it viewed across a diameter of the discharge. A Boltzmann plot was used to obtain temperature from the measured line intensities. The intensity of a single line used to construct a Boltzmann plot is given by

$$I = \frac{hc}{4\pi} \ell \rho_o \frac{gA}{Q_o \lambda} e^{-E_n/KT} = 1.58 \times 10^{-20} \ell \rho_o \frac{gA}{Q_o \lambda} e^{-E_n/KT} \qquad (1)$$

From Eq. (1),

$$\log_{10}\left(\frac{I\lambda}{gA}\right) = C - \frac{0.625\, E_n}{T} \qquad (2)$$

Thus, measurement of the intensity, I, and use of known values of the other parameters for a given line permits calculation of the temperature. Equation (2) may be applied by plotting $\log_{10}(I\lambda/gA)$ vs E_n for many lines (the Boltzmann plot) and finding the slope of a straight line through all points.

A plot for one test of an argon discharge is shown in Fig. 17. Values of λ/gA and E_n were obtained from Refs. 9 and 10. These data (Fig. 17) were obtained with a discharge pressure of 3 atm abs and with 15 kw of power deposited in the discharge. The results indicate that the average temperature along the diameter was about 9080 K.

Estimates of the temperature distributions within discharges were made using the observed chordal variation in intensity of the 7635 Å spectral line. The chordal intensity variation for the discharge of Fig. 17 is shown in Fig. 18a. Data from both the upper and lower halves of the discharge are shown, with a faired curve used to represent the chordal intensity profile. The radial intensity profile corresponding to the observed chordal profile of Fig. 18a is shown in Fig. 18b. This profile was calculated using an Abel inversion technique programmed for machine computation. The intensities plotted on Fig. 17 represent the net intensity due to radiation along the discharge diameter. For this reason, the temperature of 9080 K determined from Fig. 17 is an intensity-average mid-chord temperature. It was next assumed that the measured intensity of the 7635 Å line at $r/r_1 = 0$ (see Fig. 18a) corresponds to the intensity-average mid-chord temperature. This permits calculation of the radial distribution of temperature within the discharge by combining the radial intensity profile from Fig. 18b with the variation of intensity with temperature for the 7635 Å argon line determined from Eq. (2). The resulting radial variation of temperature is shown in Fig. 18c. Note that the peak temperature of approximately 9400 deg K occurs away from the discharge centerline. This is due to the combined effects of radiation from the discharge and the mechanism for power deposition; in an r-f discharge, power tends to be deposited more in an annulus rather than along the discharge centerline.

Effect of Several Parameters on Radiated Energy

A series of tests was conducted to determine the effect of chamber pressure on the fraction of total discharge power that is radiated. As indicated schematically in Fig. 16, the discharge was ellipsoidal and was confined to the region between the end

walls. Figure 19 presents the results of tests in which the discharge pressure was varied from 2 to 6 atm. The ordinate in Fig. 19 is the power measured using a radiometer, or the sum of the radiometer measurement and the power deposited in the peripheral-wall cooling water, divided by the total discharge power. The power actually radiated was somewhat greater than that shown by the radiometer data (i.e., the lower data in Fig. 19), since a significant portion of the radiation from the plasma may have been absorbed in the peripheral-wall cooling water. To maintain a satisfactory (i.e., steady and well confined) discharge during these tests with different conditions of pressure, total discharge power, and argon weight flow rate, simultaneous changes in at least two of these parameters were usually necessary. The argon flow rate varied from 0.01 to 0.012 lb/sec and the total power deposited in the discharge varied from 14.4 kw to approximately 34.1 kw as the pressure was increased. These results show an increase in the percent radiated power with increased pressure. The radiometer measurements indicate that the power radiated increased from approximately 33 percent to 45 percent of the total power as the discharge pressure and total discharge power were simultaneously increased from 2 atm to 6 atm and 14.4 to 34.1 kw, respectively. Taking power deposited in the cooling water into account, the increase was from about 40 percent to 65 percent. Further increases in discharge pressure to 30 atm are planned in future tests.

Figure 20 shows the effect of increasing the total discharge power on the percent power radiated. The total discharge power was determined by summing the power measured by the radiometer, the power deposited in the peripheral-wall cooling water, and the power deposited in the end-wall cooling water. These data are for a discharge pressure of 6 atm. The data indicate that the percent of total power that was radiated was essentially independent of the total power deposited in the plasma.

Measurements of discharge diameter obtained from photographs similar to those shown in Fig. 15 are presented in Fig. 21 for a range of discharge pressure from 2 to 6 atm and a range of discharge power from 14.4 to 85 kw. As discussed previously, this method of determining the discharge diameter is somewhat arbitrary, since it depends upon the neutral density filter used when the discharge is photographed. For these data, simultaneous increases in discharge pressure and total power were sufficient to maintain a constant discharge diameter. Also shown in Fig. 21 are scales of constant discharge volume and surface area which were calculated assuming that the discharge was an ellipsoid having a 2-in.-long major axis and a minor axis equal to the discharge diameter. The size of the discharge relative to the location of the peripheral wall and the r-f heater coils can also be seen in Fig. 21.

Figure 22 shows the variation of discharge power per unit volume with total discharge power corresponding to the data presented in Fig. 21, and Fig. 23 shows the variation of radiant energy flux with discharge power for these tests. The power per unit volume increased as the total discharge power increased; the maximum value obtained in these tests was 220 kw/in.^{3}. Emphasis in future tests should be directed toward achieving higher values of discharge power per unit volume. The values of

discharge power per unit volume and radiant energy flux obtained in these experiments are significantly greater than those which have been obtained in previous investigations in which r-f induction heated plasmas were employed. For instance, in the investigation described in Ref. 11, approximately 405 kw of power was deposited in an argon discharge. However, the power per unit volume for this discharge was approximately 28 kw/in.^{3} as compared to 220 kw/in.^{3} obtained in the tests described above. The power density in Ref. 11 was calculated for a discharge volume equal to that of a 4.5-in.-dia by 9.0-in.-long cylinder.

For a total discharge power of 85 kw (the highest obtained to date in any test), the energy carried away in the peripheral-wall cooling water was 19 kw. If this energy were to be deposited uniformly over a 2-in.-long section of the inside surface of the peripheral wall, the resulting heat flux through the wall would be 1.33 kw/in.^{2}. This heat flux would result in a temperature drop through the wall of 2630 R for the wall thickness of 0.059 in. However, the actual temperature drop through the wall is much less than this value because not all of the energy must be conducted through the wall; some of this energy is deposited at intermediate stations through the wall and some is deposited directly in the cooling water.

The test point which provided the highest total discharge power (85 kw) yielded a radiated power through the transparent wall of 35 kw and a total of radiated power plus power deposited in the peripheral-wall cooling water of 54 kw. The discharge volume in this test was 0.36 in.^{3}, and the discharge surface area was 2.9 in.^{2}. Therefore, the power levels of 35 and 54 kw correspond to 97 and 150 kw/in.^{3}, respectively, and 12 and 19 kw/in.^{2}, respectively. These heat fluxes correspond to equivalent black-body radiating temperatures of 7600 R and 8500 R, respectively.

It is now of interest to compare the heat deposition rates and heat fluxes in the model test to those of a full scale engine. The heat flux level for the engine of Ref. 1 is 178 kw/in.^{2}, which corresponds to an equivalent black-body radiating temperature of 15,000 R. The total energy deposited in the fuel-containment region of a full-scale engine corresponds to a power deposition per unit volume of 43.5 kw/in.^{3}. However, the power per unit volume in a model to provide a black-body radiating temperature of 15,000 R would be 1820 kw/in.^{3} (higher due to the difference in the surface-to-volume ratio between the engine and the model). The radiant heat fluxes obtained in these tests were only 7 to 11 percent of those required to simulate the full-scale engine of Ref. 1. However, a nuclear light bulb engine would still be extremely useful even if the radiant flux were considerably less than the value of 178 kw/in.^{2} corresponding to a black-body radiating temperature of 15,000 R; the exact value of radiant heat flux required to justify engine development is a function of the mission to be considered.

Results of Tests with Seeded Discharges

The radiant-energy source configuration shown in Fig. 24 was used in tests with seeded discharges. This configuration had a 2.28-in.-ID water-cooled peripheral wall and 0.80-in.-dia water-cooled end walls. The end walls were 2.0-in. apart and had 0.185-in.-dia thru-flow ports located at their centers. Argon was injected through eight 0.10-in.-ID stainless steel tubes located on a 1.5-in.-dia circle at one end of the test chamber. A copper spacer (see Fig. 24) was located 3 in. back from the face of each end wall. This spacer served as a locating support for the eight swirl injection tubes; it provided a means for adjusting the injection angle and axial location of the tubes. Two 0.040-in.-ID seed ports were located on each end wall at radii of 0.170 in. and 0.270 in. from the centerline. For the tests reported herein, only the innermost seed injection port on one end wall was used. The outer seed port on the same end wall was used as a static pressure tap. The seed ports on the opposite end walls were not used. Stainless steel tubes for seed injection were routed directly out the rear of the end-wall assembly. The particle seeding system (see DESCRIPTION OF PRINCIPAL EQUIPMENT) was connected to these stainless steel tubes so as to minimize the length of the particle seed ducts.

The objective of these tests was to investigate the effectiveness of seeds in increasing the emission from an r-f plasma discharge. Determining the optimum method for seeding an r-f plasma discharge depends strongly on the attainment of a steady-state, long-run-time, and reproducible seeding system in addition to a steady, reproducible r-f discharge. Although significant gains in these areas were achieved during this investigation, additional refinements and modifications to the particle seeding system are still required.

A series of tests with seeded discharges was conducted. Two seed materials were employed. Small amounts of submicron-sized carbon and tungsten particles were injected into the discharge using the particle seeding system. To allow for a more systematic comparison of the tests with the different types of seed material, the tests with each seed material were conducted at the same chamber pressure (1.8 atm) and argon weight flow rate (0.006 lb/sec). During these tests, the saturable reactor controls were set to maintain a constant power amplifier d-c supply voltage. The small change in total discharge power (Q_T increased from 10.1 to 12.7 kw when carbon seeds were added to the discharge) which occurred during these tests may be due in part to a small change in the discharge impedance caused by the presence of the carbon seeds. The exact weight flow rate of seed material used in the tests was not measured; however, the weight flow of seed particles was small compared to the total argon weight flow rate.

Results of tests employing small amounts of 0.012-micron-dia carbon particles (Carbolac 2) are presented in Fig. 25. For comparison, data from tests of an unseeded argon discharge are also presented. During the latter tests, argon was

injected into the test chamber through the innermost seed injection port on one end wall at the same weight flow rate employed in the particle seeding tests. This technique was used because, in a preliminary series of tests with different amounts of argon injected into the discharge through the seed port, an effect of this injection flow on the discharge was noted. For these earlier tests (see Appendix II), a distinct effect on the behavior of the r-f discharge was noted when the argon carrier gas flow rate reached approximately 20 percent of the total argon end-wall injection swirl flow rate. For example, the intensity level began to fluctuate, the luminous boundary of the discharge became more diffuse and turbulent in appearance, and the discharge became unsymmetrical along its major axis with an apprent increase in discharge size in the discharge region farthest from the seed port. For the results shown in Fig. 25, where the argon flow rate through the seed port was approximately 15 percent of the primary argon flow rate, the addition of a small amount of carbon seed resulted in a slightly greater than 60 percent increase in the total radiation over the unseeded case. No measurable change occurred in the amount of heat transferred to the end walls or to the peripheral wall. The wavelength band which increased most significantly was the infra-red band (specifically the 1.0- to 1.3-micron range) in which an increase of approximately 135 percent was measured. Visual observations indicated that many small luminous particles appeared to be rotating rapidly in the circumferential direction around the major axis of the discharge at approximately the mid-plane of the discharge. This may be an indication that some of the injected carbon seed particles did not fully vaporize upon injection.

In addition to the data obtained in the tests employing carbon seeds, much valuable information was obtained on the techniques associated with successful injection of submicron-sized particles into r-f plasma discharges. This is encouraging in light of the difficulty prior investigators have had in injecting micron-sized metal seeds into a plasma discharge (see, for example, Refs. 11 and 12).

In tests employing 0.02- to 0.06-micron (average diameter) tungsten particle seeds, no quantitative data were obtained due to difficulties in obtaining a suitably steady flow of particles from the seeding system into the test chamber.

Upon completion of the tests using the carbon seed and the tungsten seed, a visual inspection was made of the end walls, fused silica tubes, and test section. The results indicated plating of some of the seed material on the face of each end wall, plating on the exterior of the end wall support as far back as the copper spacer, and on the ID of the 2.28-in.-ID fused silica tube from a position approximately 1.0-in. back from the end-wall face to near the copper spacer. The fact that the seeding material did not plate on the peripheral wall of the test chamber within the 2.0-in. length adjacent to the discharge appears to be a result of the type of vortex used (radial inflow; see Appendix III).

The results of tests with seeded discharges have shown that seeds can be effectively used to increase the radiant emission from a plasma discharge. Similar results have been obtained with WF_6 and UF_6 seeds in the tests reported in Ref. 13. In future tests at higher power levels, use of higher seed flow rates should result in even greater increases in radiant emission than those obtained in the present tests.

Tests with Transparent Walls Adjacent to the Radiant Energy Source

Description of Configurations Tested

Model with End-Wall Vortex Injection

A photograph of the transparent-wall model assembly used in tests with end-wall vortex injection is presented in Fig. 26a. Details of the end walls and the transparent-wall model are presented in Figs. 27a and 28, respectively. The transparent-wall configuration had a 1.26-in.-ID water-cooled peripheral wall and 1.25-in.-dia water-cooled copper end walls (Fig. 27a). The end walls were spaced 2.0-in. apart and had 0.185-in.-dia thru-flow ports located at their centers. Argon was injected through eight 0.056-in.-dia ports located on each end wall (see Fig. 28b). The argon injection velocity had both tangential and axial components since the injection ports were drilled at an angle of 30 deg to the plane of the end wall. The argon flow was removed through the thru-flow ports.

The transparent-wall model used in these tests consisted of an inner 1.26-in.-ID by 1.38-in.-OD fused silica tube (nominal wall thickness, 0.06 in.) surrounded by an outer 1.75-in.-ID by 1.93-in.-OD fused silica tube. Both tubes were mounted in a Rexolite sleeve and cap assembly at each end as shown in Fig. 28a. Silicon rubber "O" rings and a high-temperature sealant were used to form the water-tight seals necessary between the fused silica tubes and the Rexolite sleeves. Cooling water flowed in the annulus between the fused silica tubes of the model (see Fig. 28).

Model with Peripheral-Wall Vortex Injection

A photograph of the transparent-wall model assembly used in tests with peripheral-wall vortex injection is shown in Fig. 26b. The configuration consists of two 0.8-in.-dia water-cooled copper end walls located 2.0-in. apart on which the transparent-wall model with axial-coolant tubes and with provision for peripheral-wall vortex injection was positioned. The end walls are shown in Fig. 27b; they were identical to those shown previously in Fig. 24 except that, for these tests, the stainless steel vortex injection tubes used in the radiant energy source tests were removed.

A photograph of the transparent-wall model is shown in Fig. 29a. It consists of forty-six axial coolant tubes with three peripheral-wall vortex injection tubes located at 120-deg intervals around the model circumference. The wall thickness of the axial coolant tubes was 0.020 in. and the wall thickness of the peripheral-wall vortex injection tubes was 0.040 in. A detailed sketch of the model is shown in Fig. 29b. The 0.0125-in.-dia vortex injection ports were ultrasonically drilled and were positioned such that an injection angle of about 11 deg was provided. This model was fabricated by first locally heating the ends of a group of the small axial tubes and one of the fused silica manifolds. Then, while still hot, the group of tubes were quickly pushed into the manifold while air was blown through the tubes. This process of "blowing" the axial tubes into the manifolds produced a completely fused structure. The fused silica coolant tubes leading to and from the manifolds and the peripheral-wall vortex injection tubes were connected to copper tubing with shrinkable teflon tubing which provides a flexible seal between the fused silica and the copper tubing.

Results of Tests

Model with End-Wall Vortex Injection

Tests were conducted to determine the effect of discharge pressure, discharge power, and argon weight flow rate on the overall power balance of the discharge. Results are presented in Figs. 30a, 31a, and 32a. (Results shown in Figs. 30b, 31b, and 32b are discussed in the following subsection.) Photographs taken from both side-on and angled-on directions indicated the discharge had a nearly constant diameter throughout the major portion of its length. Near the end walls, the discharge rapidly decreased in diameter toward the thru-flow exit ports. Thus, the overall shape of the discharge could be described as cylindrical with conical ends; in the earlier tests of the radiant energy source, a very definite ellipsoidal shape was observed.

Figure 30a shows the effect of discharge pressure on the fraction of power radiated from the discharge in the tests with end-wall injection. As previously discussed, to maintain a satisfactory discharge during tests with different conditions of pressure, total discharge power, and argon weight flow rate, simultaneous changes in at least two of these parameters were usually necessary. Curves for both Q_R/Q_T and $(Q_R + Q_W)/Q_T$ are included on the figures as was done previously for the test results with radiant energy source configurations. Since an unknown amount of radiation is absorbed in the annular cooling water, the true radiated power level is somewhere between the two curves shown in Fig. 30a. The difference between the two curves gives an indication of the peripheral-wall cooling water heat load. For the power range of 7 to 28 kw deposited in the discharge, and for argon flow rates from about 0.0012 to 0.006 lb/sec, a relatively linear increase in both Q_R/Q_T and $(Q_R + Q_W)/Q_T$ with increasing discharge pressure was obtained. These results are similar to those obtained in tests of the radiant energy source configuration (Fig. 19).

Approximately 35 percent of the total discharge power was radiated in a test with a discharge pressure of 4 atm, a total discharge power of 15.6 kw, and an argon weight flow rate of 0.003 lb/sec. The maximum measured radiated power was 8.3 kw in a test with a discharge pressure of 3.8 atm, an argon weight flow rate of 0.0066 lb/sec, and a total discharge power of 26 kw. The discharge was approximately 1.0 in. in diameter. The maximum power deposited was limited by high heat transfer at the peripheral wall caused by turbulence attributable to the end-wall injection method used to drive the vortex.

Figure 31a shows the effect of argon flow rate on the power radiated and power deposited in the peripheral-wall cooling water with end-wall vortex injection. A decrease in Q_R/Q_T was obtained when W_A was increased whereas corresponding $(Q_R + Q_W)/Q_T$ data exhibited a minimum point as W_A was increased. These data show that, for the test range covered, when the argon flow rate increased or decreased beyond the minimum point, a substantial increase in $(Q_R + Q_W)/Q_T$ occurred.

Figure 32a illustrates the effect of total discharge power on Q_R/Q_T and $(Q_R + Q_W)/Q_T$. As was found in the tests with the radiant energy source configuration shown in Fig. 20, Q_R/Q_T and $(Q_R + Q_W)/Q_T$ are relatively insensitive to total discharge power.

Attempts to increase the total discharge power level with end-wall injection above 30 kw and the pressure level above 4 atm resulted in a series of model failures. One model cracked because the discharge diameter was almost equal to the model diameter. Attempts to reduce the heat load to the peripheral wall by increasing the argon flow rate were unsuccessful. Instead, the increase in argon weight flow near the peripheral wall caused the peripheral-wall heat load to increase (possibly due to the turbulence from the end-wall injectors). A photograph of a cracked model is presented in Fig. 33a. The inner fused silica tube is discolored, devitrified, and cracked. Microscopic examination of the inner tube of the model and end wall after disassembly indicated that as much as 60 percent of the wall thickness in the central portion of the fused silica tube had ablated away. In addition, a glassy solidified coating was found deposited on the face of both end walls. This coating was subjected to spectrochemical analysis which indicated principally silicon dioxide with small amounts of dissolved copper oxide (most probably from the copper end walls).

A number of transparent-wall models also cracked during lower power tests. At first it was thought that excessive thermal stress had induced the failures. However, examination of the cracked models and of the original fused silica tube from which they were cut indicated a large eccentricity was present in the original tubes. This is clearly shown in the photograph of the failed model in Fig. 33b. This indicates that preferential selection and close quality control of dimensions and purity of all fused silica tubes will be required in future advanced transparent-wall models.

Model with Peripheral-Wall Vortex Injection

Gas discharge tests were conducted using the model with peripheral-wall vortex injection in which the effects of discharge pressure, argon weight flow rate, and discharge power on the fraction of total power radiated from the discharge were investigated. These tests were similar to those employing the transparent-wall configuration with end-wall vortex injection and, for purposes of making a direct comparison of results, the data obtained from these tests are presented in Figs. 30b, 31b, and 32b.

Results of tests to determine the effect of discharge pressure on the fraction of power radiated are presented in Fig. 30b. The increase in Q_R/Q_T with increasing discharge pressure for these data is similar to the trend obtained for the configuration having end-wall vortex injection (see Fig. 30a). However, $(Q_R + Q_W)/Q_T$ for the peripheral-wall injection configuration increases more slowly than Q_R/Q_T. This indicates that as pressure and argon weight flow rate increased, the percent of total power lost to peripheral-wall cooling water decreases. This contrasts with data from the end-wall injection configuration which shows that Q_W/Q_T remained approximately constant ($Q_W/Q_T = (Q_R + Q_W)/Q_T - Q_R/Q_T$). Multiple reflections due to the axial coolant tubes prevented an exact determination of discharge diameter and shape in these tests. The maximum power deposited in test employing a transparent-wall model with axial coolant tubes and peripheral-wall vortex injection was 24 kw; the corresponding power radiated was 5.1 kw at 5.3 atm. The maximum discharge power was limited by high heat transfer which caused localized melting of the uncooled vortex injection tubes to occur. In future tests at higher powers employing models of this type, steps must be taken to reduce the diameter of the discharge relative to the model diameter so as to reduce the amount of heat transferred by conduction and convection from the surface of the discharge to the peripheral wall of the model.

Figure 31b shows the effects of argon weight flow on Q_R/Q_T and $(Q_R + Q_W)/Q_T$ for a wide range of discharge pressure . There was a large increase in Q_R/Q_T with W_A while $(Q_R + Q_W)/Q_T$ increased only slightly over the same range. However, there was a corresponding rise in pressure as argon weight flow was increased. The steep slope of the Q_R/Q_T curve in Fig. 31b may be due in part to a pressure effect.

Figure 32b shows the effect of total discharge power on Q_R/Q_T and $(Q_R + Q_W)/Q_T$. These data show that, as total discharge power was increased, Q_R/Q_T increased and then leveled off. The data points which make up the level portion of the curve were obtained in tests at a nearly constant pressure of 5 atm. The initial increase in Q_R/Q_T at low power levels is attributed to the effect of pressure on Q_R/Q_T shown in Fig. 30b. The effects of total discharge power on $(Q_R + Q_W)/Q_T$ were very slight, i.e., $(Q_R + Q_W)/Q_T$ was essentially independent of total discharge power. This indicates that the percentage of power deposited in the peripheral wall at the higher pressure remains approximately constant with increasing discharge power. This result is similar to the results obtained in tests of the radiant energy source configuration and the transparent-wall configuration with end-wall vortex injection.

REFERENCES

1. McLafferty, G. H. and H. E. Bauer: Studies of Specific Nuclear Light Bulb and Open-Cycle Vortex-Stabilized Gaseous Nuclear Rocket Engines. United Aircraft Research Laboratories Report F-910093-37, prepared under Contract NASw-847, September 1967. Also issued as NASA CR-1030, 1968.

2. Clark, J. W., B. V. Johnson, J. S. Kendall, A. E. Mensing, and A. Travers: Summary of Gaseous Nuclear Rocket Fluid Mechanics Research Conducted Under Contract NASw-847. United Aircraft Research Laboratories Report F-910091-13, May 1967. Also AIAA Paper No. 67-500, presented at AIAA 3rd Propulsion Joint Specialist Conference, Washington, D. C., July 17-21, 1967.

3. Lanzo, C. D. and R. G. Ragsdale: Heat Transfer to a Seeded Flowing Gas from an Arc Enclosed by a Quartz Tube. NASA Technical Memorandum X-52005, June 10-12, 1964.

4. Williams, J. R., A. S. Shenoy, and J. D. Clement: Radiant Propellant Heating in the Gaseous Core Nuclear Rocket. AIAA Paper No. 68-572, presented at the AIAA 4th Propulsion Joint Specialist Conference, Cleveland, Ohio, June 10-14, 1968.

5. Lanzo, C. D. and R. G. Ragsdale: Experimental Determination of Spectral and Total Transmissivities of Clouds of Small Particles. NASA TN D-1405, September 1962.

6. Burkig, V. C.: Thermal Absorption in Seeded Gases. Douglas Report DAC-59985, January 1967.

7. Marteney, P. J.: Experimental Investigation of the Opacity of Small Particles. United Aircraft Research Laboratories Report C-910092-2, prepared under Contract NASw-847, September 1964. Also issued as NASA CR-211.

8. International Critical Tables. Volume V, McGraw-Hill Book Company, Inc., 1930.

9. Adcock, B. D. and W. E. G. Plumtree: On Excitation Temperature Measurements in a Plasma-Jet, and Transition Probabilities for Argon Lines. Journal of Quantitative Spectroscopic Radiative Transfer, Vol. 4, 1964.

10. Coates, P. B. and A. G. Gaydon: Temperature Measurements in Shock Tubes, Transition Probabilities for Argon Lines. Proceedings of the Royal Society of London, Vol. 293, 1966.

11. Thorpe, M. L.: RF Plasma Simulation of Gas Core Reactor. AIAA Paper No. 68-712, Presented at the AIAA Fluid and Plasma Dynamics Conference, Los Angeles, California, June 1968.

REFERENCES (Continued)

12. Thorpe, M. L.: Induction Plasma Heating: System Performance, Hydrogen Operation and Gas Core Reactor Simulator Development. NASA CR-1143, prepared under Contract NAS 3-9375, August 1968.

13. Marteney, P. J., A. E. Mensing, and N. L. Krascella: Experimental Investigation of the Spectral Emission Characteristics of Argon-Tungsten and Argon-Uranium Induction Heated Plasmas. United Aircraft Research Laboratories Report G-910092-11, prepared under Contract NASw-847, September 1968.

14. Travers, A: Experimental Investigation of Radial-Inflow Vortexes in Jet-Injection and Rotating-Peripheral-Wall Water Vortex Tubes. United Aircraft Research Laboratories Report F-910091-14, prepared under Contract NASw-847, September 1967. Also issued as NASA CR-1028.

15. Anderson, O.: Theoretical Solutions for the Secondary Flow on the End-Wall of a Vortex Tube. United Aircraft Research Laboratories Report R-2494-1, prepared under Contract AF 04(611)-7448, November 1961.

16. Travers, A. and B. V. Johnson: Measurements of Flow Characteristics in a Basic Vortex Tube. United Aircraft Research Laboratories Report C-910091-2, prepared under Contract NASw-847, September 1964. Also issued as NASA CR-278.

17. Douglas, F. C. and R. M. Gagosz: Experimental Investigation of Thermal Annealing of Nuclear-Reactor-Induced Coloration in Fused Silica. United Aircraft Research Laboratories Report D-910082-7, prepared under Contract NASw-847, March 1965. Also issued as NASA CR-304.

18. Kendall, J. S.: Experimental Investigation of Containment in Constant-Temperature Radial-Inflow Vortexes. United Aircraft Research Laboratories Report F-910091-15, prepared under Contract NASw-847, September 1967. Also issued as NASA CR-1029.

19. Kendall, J. S., A. E. Mensing, and B. V. Johnson: Containment Experiments in Vortex Tubes with Radial Outflow and Large Superimposed Axial Flows. United Aircraft Research Laboratories Report F-910091-12, prepared under Contract NASw-847, May 1967. Also issued as NASA CR-993.

LIST OF SYMBOLS

A	Absolute transition probability of emission between two energy levels, sec^{-1}
A_j	Simulated buffer gas injection area, sq in.
A_s	Discharge surface area, sq in.
c	Velocity of light, 3×10^{10} cm sec^{-1}
C	Constant, dimensionless
D	Diameter of vortex tube or transparent-wall model, ft or in.
d	Discharge diameter, $2r_6$, ft or in.
E_N	Upper energy level, cm^{-1} or ev
g	Statistical weight of energy level, dimensionless
h	Planck's constant, 6.62×10^{-27} erg-sec
I	Total intensity of radiation of a single line, watts cm^{-2} sec^{-1} $ster^{-1}$
I_t/I_i	Transparency of filter, dimensionless
$I(\lambda)/I_o(\lambda)$	Internal transmittance, dimensionless
k	Boltzmann constant, 1.38×10^{-16} erg deg K^{-1}
L	Length of vortex tube or transparent-wall model, ft or in.
ℓ	Length of radiating source (Eq.1), cm
m_c	Molecular weight of carrier gas in simulated-fuel mixture (Eq. (IV-3))
m_F	Molecular weight of simulated fuel
m_I	Molecular weight of iodine, 254 (Eq. (IV-3))
P	Total pressure, atm
P_D	Discharge pressure, atm
P_F	Local simulated-fuel partial pressure, atm

$P_{F(0.9)}$	Local simulated-fuel partial pressure at $r/r_1 = 0.9$, atm
$\bar{P}_F$	Average simulated-fuel partial pressure, $\frac{\bar{\rho}_F \mathcal{R} T_1}{m_F}$, atm
Q_o	Partition function of radiation species, dimensionless
Q_R	Power radiated (as measured by radiometer), kw
Q_T	Total discharge power, kw
Q_W	Power deposited in peripheral-wall coolant, kw
Q_t	Total volumetric flow rate through thru-flow ports, ft^3/sec or gpm
r	Radial distance measured from centerline of vortex tube or transparent-wall model, ft or in.
r_s	Radius of radial stagnation surface, ft or in.
r_1	Vortex tube radius, ft or in.
r_6	Radius of discharge, ft or in.
Re_r	Radial Reynolds number, $Q_t/2\pi\nu L$, dimensionless
$Re_{t,p}$	Tangential Reynolds number based on velocity at peripheral wall of jet-injection vortex tube, $V_{\phi,P}\ r_1/\nu_1$, dimensionless
T	Temperature, deg R or deg K
V	Discharge volume, ft^3 or $in.^3$
V_ϕ	Tangential (circumferential) velocity of flow in vortex tube, ft/sec
$V_{\phi,p}$	Tangential velocity at peripheral wall of vortex tube after injected flow has been slowed down due to peripheral-wall friction, diffusion, and jet mixing, ft/sec
W	Weight flow rate, lb/sec
W_A	Argon weight flow, lb/sec
W_B	Weight flow rate of simulated-buffer gas, lb/sec

LIST OF SYMBOLS (Continued)

$W_{B,TF}$	Weight flow rate of simulated-buffer gas removed through thru-flow port, lb/sec
W_c	Weight-flow rate of carrier gas in simulated-fuel mixture, lb/sec
W_F	Weight-flow rate of simulated-fuel mixture, $W_c + W_I$, lb/sec
W_I	Weight-flow rate of iodine in simulated-fuel mixture, lb/sec
$\mathcal{W}_F$	Total amount of simulated fuel contained in vortex tube, lb
x	Distance from discharge center to chord at radius r, ft or in.
β_t	Secondary flow parameter $(D/L)Re_{t,p}^{0.8}/Re_r$, dimensionless
$\Delta\lambda$	Wavelength range, microns
λ	Wavelength, microns or Angstroms
ρ_B	Density of simulated-buffer gas at injection, lb/ft^3
ρ_F	Local simulated-fuel density at a given radius, lb/ft^3
ρ_o	Particle density, cm^{-3}
$\bar{\rho}_F$	Average simulated-fuel density, lb/ft^3
$(\rho V^2)_F$	Dynamic pressure of simulated fuel at injection, atm
$(\rho V^2)_B$	Dynamic pressure of simulated buffer gas at injection, atm
μ_B	Laminar viscosity of simulated-buffer gas, lb/ft-sec
ν	Kinematic viscosity, ft^2/sec

Subscripts

M	Lower energy level
N	Upper energy level
l	Vortex tube periphery

APPENDIX I

TRANSPARENT-WALL MODEL DEVELOPMENT PROGRAM

The primary purpose of this program is to develop thin, internally-cooled, transparent-wall models similar to those which might be employed in a nuclear light bulb engine. These models are used in tests around radiant energy sources. The walls of the model must be highly transparent to pass thermal radiation for heating the propellant stream. They must be cooled to remove heat deposited by radiation, conduction, and convection. The walls must also have provision for tangential injection to create a vortex flow which provides a buffer layer between the nuclear fuel and the transparent walls. A review of the present status of this program is presented herein.

Physical Characteristics of Fused Silica For Use in Transparent-Wall Models

Table II is a summary of various characteristics of fused silica which is suitable for use in models. Transparent-wall models must be fabricated from fused silica having especially good transmittance in the ultraviolet range to permit passage of the high intensity radiation. Use of high purity grades of fused silica for models instead of the standard grades of fused silica will result in models having improved transmission in the ultraviolet portion of the spectrum (see Table II).

From Table II it can be seen that for Corning 7940 fused silica the coefficient of thermal expansion decreases with increasing temperature. The melting point of fused silica is relatively fixed as is the coefficient of thermal expansion for commercial fused silica (see Table II).

Status of Model Fabrication Program

Transparent-Wall Models for Current Test Program

A number of transparent-wall models have been fabricated using the standard purity grades of fused silica during the current program. Initially, simple models were fabricated and tested adjacent to low-intensity (less than 10 kw) light sources. These models consisted of two-wall and three-wall concentric fused silica cylinders which formed the coolant passages; vortex injectors were located on the end-walls. R-F tests of a model of this type are described in Appendix II.

More advanced transparent-wall models were also fabricated for testing adjacent to medium-intensity (less than about 30 or 40 kw) sources. These models have axial coolant tubes and peripheral-wall vortex injection tubes. An all-fused-silica model of this type which has been tested in the 1.2-megw r-f induction heater is described in the main text of this report. A photograph of another model having axial coolant tubes and peripheral-wall vortex injection tubes is shown in Fig. 34a. This model consists of axial fused silica tubes connected to copper manifolds using shrinkable teflon tubing. The teflon tubing shrinks upon heating and forms a flexible sealed connection between the fused silica and copper manifold. A schematic diagram of the model is shown in Fig. 34b. This design provides for removal and replacement of individual coolant or injector tubes should damage occur. The copper manifold can be reused many times so that only replacement of individual quartz and teflon tubing is necessary for a new model. In addition, this design can easily be adapted to thinner-wall tubes for testing adjacent to higher-intensity light sources.

Advanced Transparent-Wall Models

Advanced models will consist of both axial and circumferential cooled fused silica tubes with peripheral-wall vortex injection. The circumferential-tube models may be fabricated by the following procedure. A closely wound fused silica coil similar to that shown in Fig. 35 would be fabricated. The coil would be about five inches long and would not be fused together around the circumference. The individual tubes would be tacked together along the entire length with grading glass and would then be cut approximately in half (see Fig. 35b). The ends of the cut coils would be heated and bent as shown in Fig. 35c. The bent ends would be "blown" into axial-tube manifolds using the same techniques that were used in fabricating the models with axial coolant tubes.

Mechanical Tests of Transparent-Wall Models

A fused silica model similar to that tested and described above is shown in Fig. 36a. This model was fabricated, without the vortex injection tubes, for the purpose of determining the structural failure point for this design.

The model was hydrostatically tested with water at ambient temperature. Model failure occurred at a pressure of 300 psi in the location shown in Fig. 36b. The The failure started as a crack in one of the coolant manifolds and then spread until about one-third of the manifold had been broken. The wall of the manifold in the vicinity of the crack was approximately 0.02 in. thick due to the manner in which the manifold was fabricated. Assuming the manifold to be a ring of constant thickness, the hoop stress at the point of failure was calculated to be 4800 psi.

APPENDIX II

SUMMARY OF PRELIMINARY R-F EXPERIMENTS

Preliminary Experiments on Gas Breakdown and Power Addition

The primary objective of these tests was to obtain preliminary information on the factors that determine the size and power deposited in confined r-f discharges. A second objective was to develop experimental techniques at low power levels which could be used in future tests at higher power levels. Flowing systems with and without swirl at pressures of about 1.0 atm were investigated. Several different geometric configurations were employed. Sketches of the two principal configurations used are presented in Figs. 37 and 38 along with photographs of typical discharges. Except where noted otherwise, all of the tests discussed in this Appendix were conducted using the UARL 1.2-megw r-f induction heater.

Simple Gas Load Configuration

The simple gas load configuration shown in Fig. 37a consisted of two coaxial, thin-walled fused silica tubes. The gas discharge occurred in the region within the inner tube. Cooling water for the inner tube flowed through the annular space between the inner and outer tubes. Tests were conducted without any flow of gas through the inner tube and with pure axial flow (i.e., without swirl).

In the tests without flow, the discharge was started at an inner tube pressure of 5 mm Hg abs. Increases in tube pressure were accomplished by admitting argon until the desired pressure level was obtained and then subsequently shutting off the argon flow. Tests were conducted at inner tube pressures from 0.5 to 1.5 atm and discharge power levels from approximately 2 to 5 kw. Figure 37b shows the type of discharge obtained in these tests. For this discharge, the pressure was 1.5 atm; however, the shape of the discharge region was similar at all pressures. The discharge region was not symmetrical about the centerline of the inner tube but occupied a region nearer the top. This is due to thermal buoyancy effects since the tube was oriented with its centerline horizontal.

In the tests with axial flow, the inner tube pressure was again reduced to 5 mm Hg abs and the discharge was started. The axial flow of argon gas was then started. It was extremely difficult to obtain a steady discharge; in most tests, the discharge oscillated in both the radial and axial directions. The radial oscillation resulted in heating of the inner tube wall due to the presence of the discharge near the wall. Buoyancy effects were also noted.

Simple Gas Load Configuration with Swirl Injection

It was expected that swirl flow would provide the radial force necessary to counteract the buoyancy effects on the discharge and thereby provide improved confinement. The simple gas load configuration was modified as shown in Fig. 38a to include provision for injection of argon gas with swirl (i.e., with both tangential and axial components of injection velocity).

Steady discharges were obtained using argon gas at pressures up to 1.5 atm. A photograph of a typical argon discharge is shown in Fig. 38b. Lines indicating the location of the inner tube wall are shown. The discharge was symmetrical about the centerline; thus, the swirling flow appears to have counteracted the buoyancy effects. The diameter of the discharge region as measured from the photograph in Fig. 38b was approximately 0.7 times the inside diameter of the inner tube. By adding more axial flow to the swirl flow, it was possible to control the axial location of the discharge region. Discharges that were approximately concentric with respect to the heater coils were produced in this manner.

One factor which limited the power that could be deposited in the discharge in tests employing this configuration was heating of the inner tube several inches downstream of the heater coils. This heating appears to have been caused by mixing of the hot gas core in a secondary flow with cooler gas near the wall. A water-cooled copper end wall having a 0.75-in.-dia port at its center was placed immediately downstream of the discharge region. In one test using this end wall with helium as the flowing gas, approximately 16 kw were deposited in the discharge with little wall heating. The helium weight flow rate was 0.0031 lb/sec and the discharge diameter was approximately 0.6 times the inside diameter of the inner tube.

Experiments to Confine Vortex Discharges

Following completion of the preliminary experiments described in the preceding section, experiments to confine vortex discharges were initiated. These experiments were conducted at power levels on the order of 10 to 45 kw and utilized simple vortex tube models.

Four different vortex configurations were employed. They are identified as (1) the vortex configuration with 1.75-in.-dia end walls (Fig. 39a), (2) the vortex configuration with 0.40-in.-dia end walls (Fig. 39b), (3) the vortex configuration with 0.8-in.-dia end walls (Fig. 39c), and (4) the vortex configuration with 1.125-in.-dia end walls (Fig. 40).

Vortex Configuration with 1.75-in.-dia End Walls

This configuration (Fig. 39a) had a 2.28-in.-ID, water-cooled fused silica inner peripheral wall and 1.75-in.-dia water-cooled copper end walls. The end walls were 6 in. apart and had 0.3-in.-dia thru-flow ports. Argon was injected with a weight flow rate of 0.01 lb/sec through ten tubes located at the periphery of one end wall. For these tests the power deposited in the discharge varied from 9.6 kw to 15 kw and the discharge pressure within the inner tube varied from 1.0 atm to 4 atm. The discharge diameter measured from photographs taken through appropriate neutral density filters was approximately 0.8 in. The discharge diameter remained constant as the pressure and the total discharge power were increased. The results of radiometer measurements indicated that the power radiated increased from approximately 25 percent to 40 percent of the total power deposited in the discharge as the discharge pressure was increased from 1 to 4 atm.

Vortex Configuration with 0.4-in.-dia End Walls

This configuration (Fig. 39b) had a 2.28-in.-ID water-cooled fused silica perhipheral wall and 0.4-in.-dia water-cooled copper end walls. The end walls were 2.0 in. apart and had 0.07-in.-dia thru-flow ports located at the center of each wall. Argon was injected with swirl through eight 0.10-in.-dia tubes located near the peripheral wall at one end. The argon was removed through annular axial-flow ports located at each end and through the thru-flow ports.

Tests were conducted with argon at pressures up to 1.95 atm and weight flow rates from 0.0079 to 0.0153 lb/sec. The discharge was ellipsoidal and was confined to the region between the 0.4-in.-dia end walls; its diameter as measured from photographs varied from approximately 0.75 to 1.0 in. The power deposited in the discharge in these tests varied from 4.4 to 14.9 kw. It was found that the amount of flow that could be removed through the thru-flow ports was not sufficient to provide as much control of the discharge diameter as was desired. For this reason, tests employing this configuration were terminated in favor of a configuration having larger diameter thru-flow ports.

Vortex Configuration with 0.8-in.-dia End Walls

This configuration also had a 2.28-in.-ID water-cooled, fused silica, peripheral wall and water-cooled copper end walls (Fig. 39c). The end walls were 0.8 in. in diameter with 0.125-in.-dia thru-flow ports, and were 2.0 in. apart. A 0.04-in.-dia seed port for injection of submicron particles was located approximately 0.2 in. from the center of one end wall (see Fig. 39c). Argon was injected at one end of the test chamber through eight 0.10-in.-dia tubes near the peripheral wall. The primary objective of tests employing this configuration was to obtain initial information on the effect of submicron tungsten particles on the gas discharge characteristics.

Tests were conducted in which argon alone or a mixture of argon plus submicron tungsten powder was injected into the discharge region through the seed duct. The discharge pressure was 1.0 atm and the power deposited in the gas was approximately 7 kw. The weight flow rate of argon injected through the injector tubes to drive the vortex was 0.01 lb/sec. Approximately one-fifth of the total injected flow was removed through the thru-flow ports and the remainder was removed through annular axial-flow exhaust ports at each end of the test chamber. Argon was injected through the seed duct at weight flow rates of 0.0002, 0.0004, and 0.0007 lb/sec.

The discharge was not visibly disturbed by the injection of argon alone through the seed duct except at the highest argon weight flow rate. At the highest flow rate, the discharge was distorted; it was blown toward the opposite end wall and its diameter was increased. When a mixture of argon and tungsten powder was injected through the seed duct, it appeared that only a small fraction of the injected tungsten actually penetrated into the discharge region. Examination of the fused silica peripheral wall following these tests revealed that tungsten powder had accumulated behind the injection location (away from the discharge). The presence of a recirculation zone in this particular flow pattern is the most likely cause of tungsten powder accumulation at this location. Little or no accumulation of tungsten powder was noted in the region under the heater coils.

Vortex Configuration with 1.125-in.-dia End Walls

The configuration shown in Fig. 40a was designed to be compatible with several 1.25-in.-ID transparent-wall models (see discussion of transparent-wall model designs in the main text and in Appendix I). The 1.125-in.-dia end walls each had a 0.125-in.-dia thru-flow port. In addition, one end wall had twelve 0.020-in.-ID holes near the periphery to provide injection with swirl to drive the vortex.

Figure 40a shows the configuration within the coil of the 80-kw r-f induction heater. (A description of the 80 kw r-f induction heater is given in Ref. 13.) The end walls were sealed directly to the model and no surrounding tube was used. Tests employing this configuration with 1.26-in.-ID transparent-wall model were conducted using the 80-kw r-f induction heater. Figure 40b shows the location of the discharge with respect to the inner tube wall and gives information from a typical test. Data from the tests are presented in Fig. 41 for two different distances between the end walls. These results indicate that the percent of the total discharge power deposited in the peripheral wall coolant decreased with increasing argon weight flow rate for the configuration with 2.00 in. between the end walls, and was not significantly different for the two models at low argon flow rates.

APPENDIX III

WATER-VORTEX TESTS WITH LUCITE MODELS

Supporting tests were conducted with lucite vortex tubes which are geometrically similar to the transparent-wall models described in the section entitled DISCUSSION OF RESULTS. The models used in these tests are shown in Fig. 42. They consisted of 1.25-in.-dia lucite tubes with end-walls located 2 in. apart. Thru-flow ports were located at the centers of the end walls. Dye injection ports are also shown at each end wall. Figure 42a shows the peripheral-wall injection model with the ten ultrasonically-drilled holes in each injector tube; this model was similar to the transparent-wall model shown in Fig. 29. The end-wall vortex injection model is shown in Fig. 42b; this model was similar to the transparent-wall model shown in Fig. 40.

The particular radial-inflow pattern of interest is illustrated in Fig. 43a and is discussed in Ref. 14. It is characterized by a laminar radial stagnation surface across which there is no radial convection. A central recirculation-cell region occurs inside of the radial stagnation surface, and a region of axial flow toward the end walls occurs outside the radial stagnation surface. At the radius of the radial stagnation surface, all of the radial flow passes through the end-wall boundary layers. Previous flow visualization studies in jet-injection vortex tubes have shown that the flow is essentially laminar at radii less than that of the radial stagnation surface and is turbulent at larger radii. According to the theoretical investigation reported in Ref. 15, radial stagnation surfaces and cells occur when the secondary flow resulting from friction on the end walls and the radial gradient of pressure in the vortex is greater than the flow withdrawn through the thru-flow ports at the centers of the end walls. A secondary-flow parameter

$$\beta_t = \left(\frac{D}{L}\right)\left(\frac{Re_{t,p}^{0.8}}{Re_r}\right) \qquad \text{(III-1)}$$

was introduced in Ref. 15. In this equation, D and L are the diameter and length of the vortex tube, $Re_{t,p}$ is the tangential Reynolds number (a measure of the tangential velocity at the periphery of the tube), and Re_r is the radial Reynolds number (a measure of the mass flow withdrawn through the thru-flow ports). The magnitude of β_t provides an indication of the type of flow pattern that will occur. Thus, an investigation was made, using β_t as a parameter, to investigate the effects of peripheral-wall vortex injection instead of end-wall swirl injection on the radial location of the radial stagnation surface. This investigation differs from previous investigations, e.g., Ref. 16, in that the actual end-wall and peripheral-wall

injection geometries which were used in the r-f tests of the transparent-wall models were also used in the water-vortex tests.

The change in location of the radial stagnation surface obtained in these tests is shown in Fig. 43b for the end-wall and peripheral-wall injection models with different weight flows. A 40 percent increase in the radius of the radial stagnation surface is obtained with peripheral-wall injection compared with end-wall injection. It is also observed from Fig. 43b that the radius of the radial stagnation surface is essentially independent of the weight flow, especially for the model with peripheral-wall vortex injection.

Values of β_t in the range of 36 to 48 were calculated for the peripheral-wall injection model using the theory of Refs. 14 and 15; values of β_t in the range of 21 to 30 were calculated for the end-wall injection model. The radius at which a radial stagnation streamline occurs decreases as β_t decreases (see Ref. 14). Thus the observed differences in flow pattern produced in these two models can be attributed to a change in location of the stagnation streamline due to the fact that the models had different injection areas. In future tests, by varying β_t and thus r_s/r_1, it will be possible to determine the optimum values of these parameters for use in advanced transparent-wall model designs.

APPENDIX IV

SUPPORTING EXPERIMENTAL INVESTIGATION OF CONTAINMENT IN CONSTANT-TEMPERATURE RADIAL-INFLOW VORTEXES

by

Stuart E. Gadbois

Experiments were conducted to investigate the containment of simulated fuel in radial-inflow vortexes. This investigation supplemented similar investigations conducted previously under Contract NASw-847 (Ref. 18). It also provided supporting information for use in the 1.2-megw r-f induction heater program. The effects on containment of changes in the following were investigated: (1) the radial Reynolds number (a measure of the amount of flow withdrawn through the thru-flow port), (2) the molecular weight of the simulated fuel, and (3) the weight flow rate of the simulated fuel at injection.

Test Equipment

Most of the test equipment employed in the present investigation was used in preceding work under Contract NASw-847 and was described in detail in Refs. 18 and 19. The essential features of this equipment and details of new test equipment which was constructed are presented in this section.

High Reynolds Number Test Facility

The high Reynolds number test facility which was employed in the tests of Ref. 18 was modified for use in this investigation. A schematic diagram of the modified facility is shown in Fig. 44. As noted in the diagram, there are three principal flow systems: the simulated-fuel supply system, the simulated-buffer-gas supply system, and the test section and exhaust system.

The simulated-fuel supply system provides a metered quantity of simulated fuel to the test section at the pressure, temperature, and weight flow rate required for a particular flow condition. For the tests reported herein, the simulated fuel consisted of a mixture of gaseous iodine and any one of three carrier gases: helium (molecular weight $m_F \approx 5$ for the mixture), air ($m_F \approx 30$), and sulfur hexafluoride ($m_F \approx 146$). To prevent condensation of the gases, the simulated fuel is heated to approximately 320 F

and the pressure in the vortex tube is maintained between 0.9 to 1.0 atm. The mixtures of iodine and helium, air, or sulfur hexafluoride are heated in the carrier gas preheater (Fig. 44). Gaseous iodine is produced from solid iodine in the specially constructed iodine boiler. Valves in the simulated-fuel supply system provide control of the fraction of iodine in the simulated-fuel mixture.

The simulated-buffer-gas supply system provides a metered quantity of air from an atmospheric inlet to the test section at the pressure, temperature, and weight flow rate required for a particular flow condition. A combination steam and electric heater is used to heat the air to the desired temperature of approximately 300 F.

The test section in which the vortex tube was mounted consists of a 20-in.-ID by 30-in.-long outer cylindrical shell with end flanges. Details of the vortex tube employed in this investigation will be described in a following section. The simulated-buffer gas flows through the outer cylindrical shell and directly into the injection plenum, an annular space between the vortex tube and the outer cylindrical shell (Fig. 44). The exhaust system consists of valves and associated piping necessary to connect the test section to vacuum pumps.

Axial Absorptometer

An axial light beam absorption technique was used to determine the amount of simulated fuel contained and the radial distribution of simulated-fuel density and partial pressure within the vortex tube. Figure 45 is a schematic diagram of the axial absorptometer showing the optical system. Further details of the absorptometer and a discussion of the principle of operation are presented in Ref. 19. In addition to the scanning system shown, a light beam from a fixed source was passed along the axis of the vortex tube.

Using this absorptometer, the amount of light absorbed by the iodine at a given radius of the vortex tube was measured. The amount of light absorbed is proportional to the axially-averaged iodine density and, hence, provides a measurement of the simulated-fuel density. The scanning light beam was continuously traversed along the vertical diameter of the vortex tube to determine the radial distribution of simulated fuel. The amount of simulated fuel stored in the vortex was determined from the radial distribution of simulated-fuel density.

Vortex Tube

The vortex tube employed in this investigation was the directed-wall-jet tube used in the investigations reported in Refs. 18 and 19. A photograph of the directed-wall-jet vortex tube partially installed in the test section of the high Reynolds number test facility is shown in Fig. 46a. It consists of a 10-in.-ID by 30-in.-long steel tube which has provision for installation of up to 900 directed-wall-jet inserts in the

peripheral wall. The details of the directed-wall-jet geometry that was used are shown in Figs. 46b and 47a. The inserts were distributed in three axial rows of 10 jets each spaced at 120-deg intervals around the periphery of the vortex tube. All inserts were oriented such that the direction of simulated-buffer-gas injection was circumferential. The injection area per insert was 0.015 sq in.; hence, the total simulated-buffer-gas injection area was $A_j = 0.45$ sq in.

The simulated-fuel injection configuration which was employed consisted of two 0.1-in.-ID by 0.125-in.-long tubes located at a radius of 5 in. on one end wall (see Fig. 47b). This resulted in a total fuel injection area of 0.0157 sq in. These tubes provided simulated-fuel injection in the axial direction only. The thru-flow was removed through a 1.0-in.-dia port at the center of the opposite end wall.

Test and Data Reduction Procedures

Test Procedures

The flow condition for a typical containment test was specified by a fixed Reynolds number and fixed weight flow rates and molecular weights of the simulated-buffer gas and simulated fuel.

For tests described herein, the temperature of the simulated-buffer gas at injection was approximately 300 F and the total pressure was between 0.9 and 1.0 atm. Air was used as the simulated-buffer gas in all tests. The Reynolds number was varied by changing the simulated-buffer-gas weight flow rate. The flow rate of the mixture of simulated-buffer gas and simulated fuel through the thru-flow port was expressed in terms of the radial Reynolds number which is defined as

$$Re_r = \frac{W_{B,TF}}{2\pi\mu_B L} \qquad \text{(IV-1)}$$

where $W_{B,TF}$ is the total weight-flow rate (assumed to be entirely simulated-buffer gas) through the thru-flow port, μ_B is the laminar viscosity of the simulated-buffer gas at injection, and L is the length of the vortex tube. Radial Reynolds numbers in this investigation were varied from approximately 100 to 360.

The containment tests were conducted in the following manner. For a given simulated-fuel molecular weight, both the simulated-fuel and simulated-buffer gas flow rates were set. The light beam of the axial absorptometer was traversed along the vertical diameter of the vortex tube at least twice to verify that the total amount of simulated

fuel within the vortex tube was constant (i.e., that a steady-state condition had been reached). The time required for a single traverse of the axial light beam was approximately 20 sec (many times the average residence time for the simulated fuel within the vortex tube). After the existence of steady-state conditions had been verified, repeated traverses were made to measure the radial distribution of simulated fuel in the vortex tube. The flow rates were then reset for the next flow condition and the process was repeated.

Data Reduction Procedures

One measure of the containment characteristics of a confined vortex flow is the average simulated-fuel density, $\bar{\rho}_F$ (i.e., a volume-averaged simulated-fuel density based on the amount of simulated fuel contained within the vortex tube). This average density is given by

$$\bar{\rho}_F = \frac{\mathcal{W}_F}{V} \qquad \text{(IV-2)}$$

where $\mathcal{W}_F$ is the amount of simulated fuel contained in the vortex tube and V is the total volume of the vortex tube. The amount of simulated fuel contained was determined by averaging data obtained from radial traverses both above and below the centerline of the vortex tube. For most data reported herein, the average value of simulated fuel stored differed from the value determined from individual upper and lower traverses by less than $\pm$ 15 percent. A detailed description of the technique employed to determine the amount of simulated fuel contained using this method is presented in Appendix III of Ref. 19.

A second containment parameter, related to the previously discussed average simulated-fuel density, is the average partial pressure of simulated fuel. This parameter was obtained directly from the average simulated-fuel density by employing the equation of state for an ideal gas. The molecular weight, m_F, of the simulated-fuel mixture was determined from the following equation for ideal gas mixtures:

$$m_F = \frac{1}{\frac{W_I}{W_F m_I} + \frac{W_c}{W_F m_c}} \qquad \text{(IV-3)}$$

Then, the average partial pressure of the simulated fuel is given by

$$\bar{P}_F = \frac{\bar{\rho}_F \mathcal{R} T_1}{m_F} \qquad \text{(IV-4)}$$

A third containment parameter, closely related to the average simulated-fuel partial pressure, is the ratio of $\bar{P}_F$ to the total pressure, P_1, in the vortex tube. This ratio is important because it is directly related to the pressure at which a nuclear light bulb engine must operate (i.e., for a given fuel density required for the critical mass, the total pressure necessary in the engine is determined by the ratio of the average fuel partial pressure to the total pressure in the vortex tube). It was assumed that the radial variation of total pressure within the vortex tube was small compared with the absolute total pressure in the vortex tube; hence, a single value of total pressure was used in determining the ratio of the average simulated-fuel partial pressure to the total pressure.

The simulated-fuel radial distribution data are presented as the ratio of the local simulated-fuel partial pressure, P_F, to the average simulated-fuel partial pressure, $\bar{P}_F$. The local simulated-fuel partial pressure is calculated from the density data obtained using the light beam traverse. The ratio $P_F/\bar{P}_F$ is identical to the ratio of the local simulated-fuel density to the average simulated-fuel density, $\rho_F/\bar{\rho}_F$, because the temperature is constant throughout the vortex tube.

Another parameter that is important is the ratio of the dynamic pressure of the simulated fuel at injection, $(\rho V^2)_F$, to the dynamic pressure of the simulated-buffer gas at injection, $(\rho V^2)_B$. The axial distance which the fuel penetrates into the vortex and the amount of free-jet type mixing that occurs is dependent upon this ratio. This ratio is calculated from the simulated-fuel flow rate, simulated-fuel injection area, buffer-gas flow rate, and simulated-buffer-gas injection area.

Discussion of Results

A summary of the results showing the variation of simulated-fuel density ratio with the ratio of buffer-gas weight flow rate to simulated-fuel weight flow rate is shown in Fig. 48. These data are for radial Reynolds numbers from Re_r = 100 to 360 and for three simulated-fuel gases (helium, air, and sulfur hexafluoride). These data are not significantly affected by changes in Re_r or the simulated-fuel molecular weight. The configuration tested was selected to achieve a radial stagnation surface at a radius which is approximately 75 percent of the maximum vortex tube radius, i.e., a flow pattern similar to that shown in Fig. 43a. The data presented in Fig. 17 of Ref. 14 indicate that this can be achieved if the secondary flow parameter, β_t, has a

value of approximately 50 (see APPENDIX III of this report and also Ref. 14). The value of the secondary flow parameter for the tests reported herein varied between 40 and 60. The radial location of the simulated-fuel injectors was selected at 50 percent of the radius of the vortex tube to insure that the simulated fuel would be injected at a radius smaller than that of the stagnation surface. The solid line on Fig. 48 is taken from Fig. 15 of Ref. 18. The current data show slightly higher levels of containment than the data of Ref. 18. The solid line represents results of tests of a vortex tube configuration similar to that employed in the present investigation except that (1) for the configuration in Ref. 18, no stagnation streamlines were present in the flow field because β_t was less than 20 and (2) thru-flow was withdrawn from both ends of the vortex tube which may have caused some of the simulated fuel to flow directly from the injection ports into the end-wall boundary layer and immediately out the adjacent thru-flow port. In the present study, however, it was possible for simulated-fuel to short-circuit to the thru-flow port at the opposite end wall. The simulated fuel could flow down the injection end wall, into the core of the vortex, and axially along the vortex centerline to the thru-flow port.

The results shown in Fig. 49 indicate that changes in radial Reynolds number had little effect on the radial distribution of simulated-fuel provided the ratio of simulated-buffer gas weight flow to simulated-fuel weight flow and the simulated-fuel molecular weight were held constant. The major effect of changes in radial Reynolds number was on the amount of simulated fuel at the centerline of the vortex tube. At the centerline the amount of simulated fuel decreased with increasing radial Reynolds number. However, these differences had little effect on the total amount of simulated-fuel contained in the vortex tube because the volume associated with small radius ratios is very small (only four percent of the vortex tube volume is inside a radius ratio of 0.2). Because of these relatively insignificant changes in fuel distribution with radial Reynolds number, tests with other molecular weight fuels were conducted at only one radial Reynolds number ($Re_r \approx 100$).

The effect of changes in the weight flow rate of simulated fuel on the radial distribution of simulated fuel is shown in Figs. 50 through 52. The radial Reynolds number was maintained constant (for the fixed geometry used in these tests, constant Re_r implies a constant simulated-buffer gas weight flow rate). The simulated fuel consisted of: (1) a helium/iodine mixture ($m_f \approx 5$) for the test results presented in Fig. 50, (2) an air/iodine mixture ($m_f \approx 30$) for Fig. 51, and (3) a sulfur- hexafluoride/iodine mixture ($m_f \approx 146$) for Fig. 52. The radial distribution of simulated fuel flattens out with increasing simulated-fuel weight flow for all simulated fuel molecular weights. This is because the high simulated-fuel weight flow rates increase the free-jet type of mixing with the simulated-buffer gas. The high dynamic pressures associated with these high simulated-fuel weight flow rates disturb the recirculation cells and radial stagnation surface present in the vortex tube . The results presented in Figs. 50 through 52 indicate that the majority of the simulated fuel was contained between the stagnation surface ($r_s/r \approx 0.7$) and the central core region for low

simulated-fuel weight flow rates and dynamic pressures. However, low simulated-fuel dynamic pressures for a fixed simulated-fuel injection area are synonymous with low fuel simulated-fuel flow rates and low total amounts of simulated fuel contained (low values of $\bar{P}_F/P_1$ and $\bar{\rho}_F/\rho_B$). Comparison of the data presented in Figs. 50 through 52 indicate that changes in molecular weight of the simulated fuel do not significantly affect the shape or levels of the radial distribution curves if the simulated-fuel dynamic pressure is used as a common parameter.

The results presented in Figs. 53 and 54 indicate that, if the simulated-fuel injection dynamic pressure is held approximately constant, changes in simulated-fuel molecular weight and simulated-fuel weight flow have relatively small effects on the radial distribution of simulated fuel. For the tests both the weight flow rate of simulated fuel and the molecular weight of simulated fuel were varied simultaneously to monitor a constant simulated-fuel injection dynamic pressure. Additional tests are necessary to separate the effects of changes in each one of these parameters on the radial distribution of simulated fuel. At the simulated-fuel injection radius (r/r_1 = 0.5), the simulated-fuel partial pressure ratio is nearly independent of molecular weight and decreases with increasing values of the simulated-fuel injection dynamic pressure. Higher simulated-fuel dynamic pressure ratios tend to cause distortion of the stagnation surfaces and recirculation cells and, consequently, the corresponding radial distributions are flattended which indicates increased mixing of the simulated-fuel and buffer gases.

The distributions of simulated fuel presented in Figs. 49 through 54 were obtained using the axial absorptometer. The data presented might be more easily interpreted if the axial distribution of fuel were known as well as the axially-averaged radial distribution. It is therefore recommended that future tests include measurements of axial distributions of simulated fuel.

The results presented in Fig. 55 indicate that, for a given simulated-fuel partial pressure ratio, less simulated fuel was near the wall for low molecular weights than for high molecular weights. This indicates that a favorable total density gradient (total density increasing with increasing radius) should tend to suppress mixing of the simulated fuel and buffer gas.

Summary of Results

1. The amount of simulated fuel detected near the wall increased as the molecular weight of the simulated fuel was increased. This result indicates that the favorable radial gradient of density (density increasing with increasing radius) existing when the helium/iodine mixture was used probably reduced mixing of simulated fuel with the simulated buffer gas. If this hypothesis is correct, the favorable gradients that would exist in the buffer region of a nuclear light bulb engine due to radial gradients

of temperature should also reduce the diffusion of fuel radially outward into the buffer-gas region.

2. For a given ratio of simulated-buffer gas weight flow rate to simulated-fuel weight flow rate, changes in the radial Reynolds number had little effect on the percentage of simulated fuel near the peripheral wall.

3. Simultaneous changes in the simulated-fuel molecular weight and the simulated-fuel weight flow rate did not significantly affect the radial distribution of simulated fuel for a given buffer-gas weight flow rate and a given value of simulated-fuel dynamic pressure at injection.

4. The results presented herein are based on axially-averaged radial distributions of simulated fuel. Measurements of axial variations of simulated fuel densities are required to better understand the flow conditions in the vortex tube.

TABLE I

SUMMARY OF MODEL GEOMETRIES EMPLOYED IN TESTS DISCUSSED IN AMIN TEXT

See Appendix II for Details of Configurations Employed in Preliminary Tests

Type of Configuration		Peripheral Wall Geometry			End Wall Geometry			Vortex Injection Geometry			Figures used to Describe Models	Figures Presenting Results of Tests
		Type of Wall	Inner Diameter of Wall	Wall Thickness	Outer Diameter	Thru-Flow Ports	Seed Injection Ducts	Injection Location	Configuration	Total Injection Area		
Radiant Energy Sources	Tests of Unseeded Discharges	Water-Cooled Fused Silica Tube	2.28 in.	0.059 in.	0.625 in.	0.125-in.-dia Ports at the Centers of the End Walls	None	Near Peripheral Wall at One End	10 0.10-in.-dia tubes Equally Spaced on 1.85-in.-dia Circle	0.0078 sq in.	16	19, 20, 21, 22, 23
	Tests of Seeded Discharges				0.80 in.	0.185-in.-dia Ports at the Centers of the End Walls	0.040-in.-dia Duct Located at Radius of 0.170 in. from the Center of one End Wall		8 0.16-in.-dia Tubes Equally Spaced on 1.5-in.-dia Circle	0.0062 sq in.	24	25
Transparent-Wall Models	Tests with End-Wall Vortex Injection		1.26 in.	0.059 in.	1.25 in.		None	Near Peripheral Wall at Both Ends	8 0.10-in.-dia Ports Equally Spaced on a 1.0-in.-dia Circle on each End Wall	0.0125 sq in.	26a, 27a, 28	30a, 31a, 32a
	Tests with Peripheral-Wall Vortex Injection	46-Internally Water-Cooled Fuxed Silica Tubes		0.020 in.	0.80 in.		0.040-in.-dia Duct Located at Radius of 0.170 in. from the Center of One End Wall	Peripheral Wall at 120-deg Intervals Around Circumference	30 0.0125-in.-dia Ports (10 Ports at Each of Three Circumferential Locations)	0.0037 sq in.	26b, 27b, 29	30b, 31b, 32b

TABLE II

SUMMARY OF AVAILABLE TYPES OF FUSED SILICA

Specific Property		Standard Purity Commercial Grades			High Purity Grades			
Manufacturer and Type		General Electric 204	Thermal American Vitreosil	Amersil Inc.	General Electric 151	Thermal American Spectrosil	Corning U.V. Grade 7940	Amersil Inc. Suprasil
Impurities (ppm)	Average	76	80.8	46	28.2	---	---	5
	Maximum	123	---	---	---	42.5*	12.3*	---
Coefficient of Thermal Expansion (α) x 10^{-6} cm/cm/ C	0 - 300 C	0.55	0.54	0.54	---	---	0.56	---
	300 - 600 C	---	0.54	---	---	---	0.40	---
	600 - 900 C	---	---	---	---	---	0.36	---
Infra-Red Cutoff at 50 Percent Transmission (Microns)**		3.6	3.6	3.6	2.4 - 2.9 and 3.6	2.5 - 2.8 and 3.6	2.6 - 2.9 and 3.6	2.5 - 3.0 and 3.6
Ultraviolet Cutoff at 50 Percent Transmission (Microns)**		0.21	0.21	0.21	0.17	0.17	0.17	0.17
Melting Point (C)		1800	1700 to 1800	1750	1800	1700 to 1800	1750	1750
Nominal Tensile Strength for Tubes (psi)***		7000	6500	7000	7000	6500	7160	7000

* Data obtained from Ref. 17

** For 10 mm thickness excluding surface reflection losses

*** Is a function of surface condition

FIG. 1

NUCLEAR LIGHT BULB ENGINE CONCEPT

UNIT CAVITY

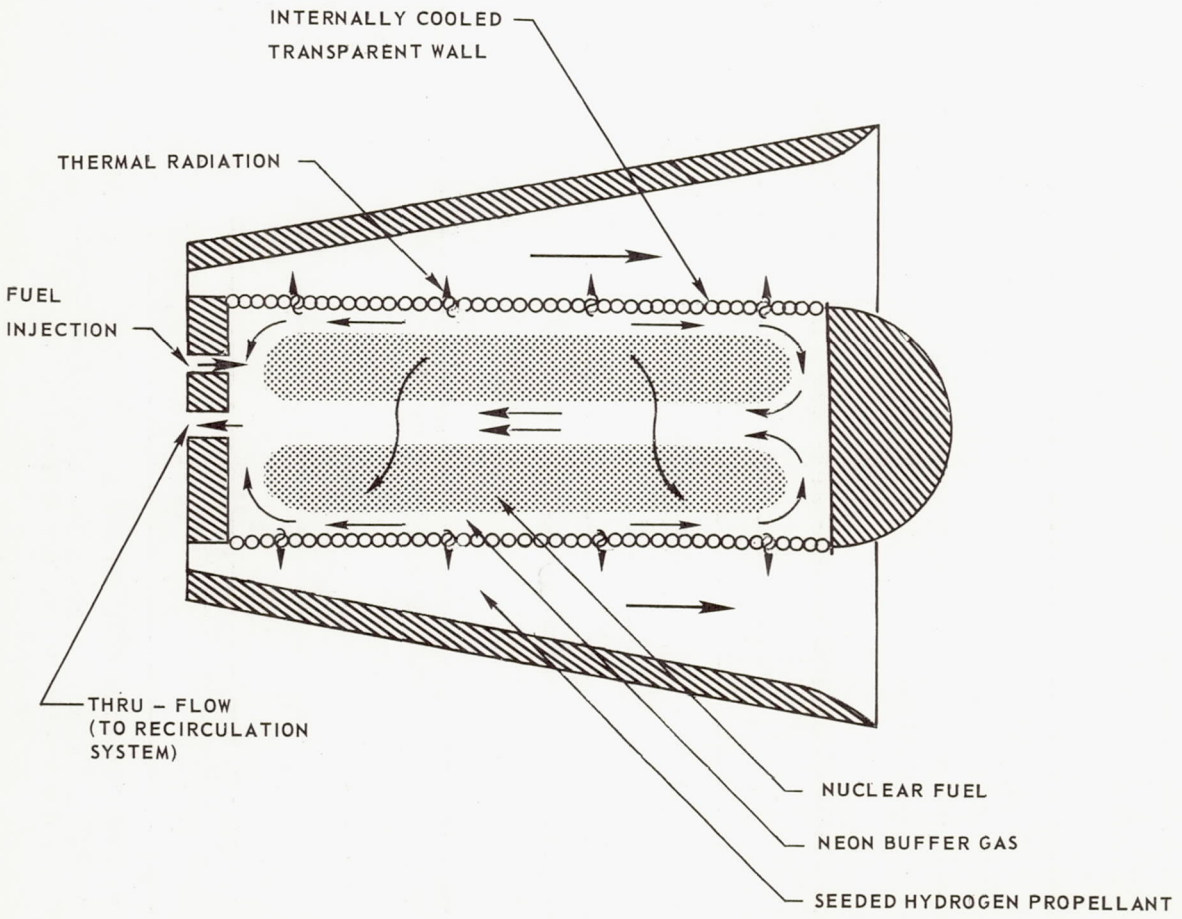

FIG. 2

BLOCK DIAGRAM OF UARL 1.2-MEGW R-F INDUCTION HEATER

POWER LEVELS SHOWN ARE MAXIMUM DESIGN VALUES

MAXIMUM TOTAL INPUT POWER DURING THIS PROGRAM FOR POWER AMPLIFIERS 1 AND 2 WAS APPROXIMATELY 250 KW

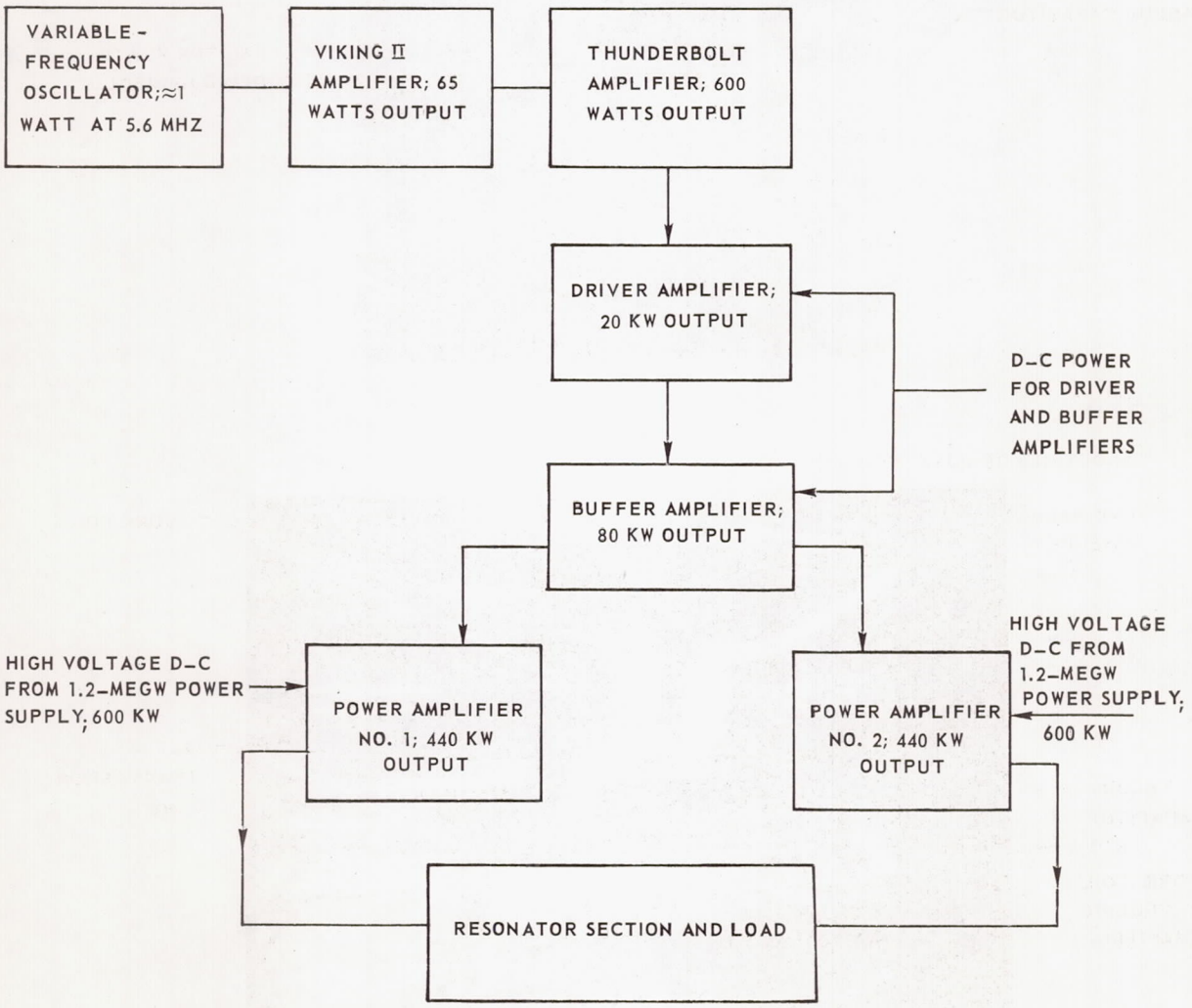

FIG. 3

PHOTOGRAPHS OF 1.2-MEGW R-F INDUCTION HEATER RESONATOR SECTION

a) PARTIALLY ASSEMBLED RESONATOR

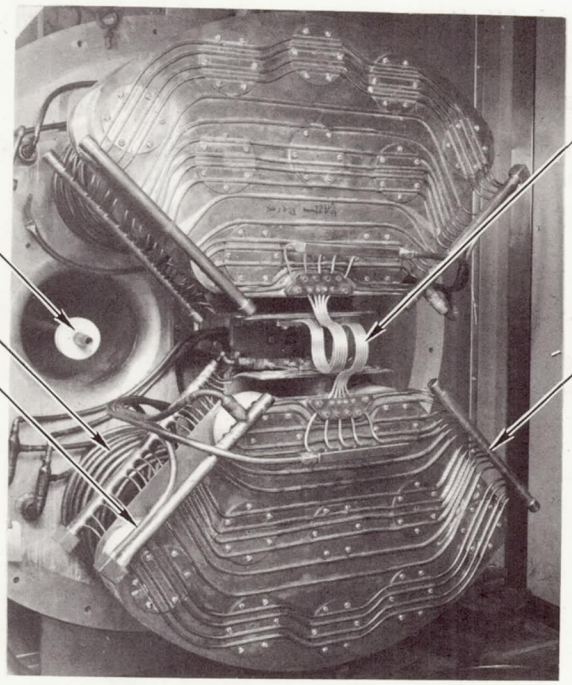

b) DETAILS OF WORK COIL

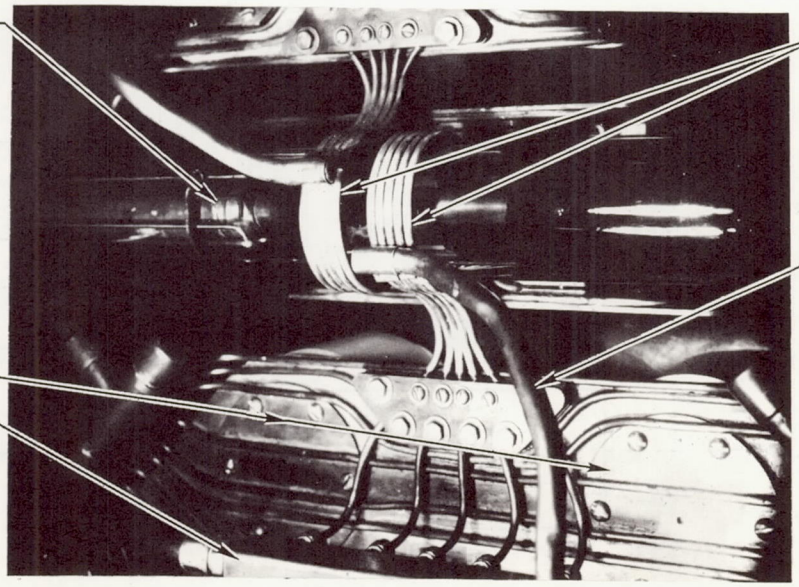

BLOCK DIAGRAM OF PLASMA STARTING SYSTEM

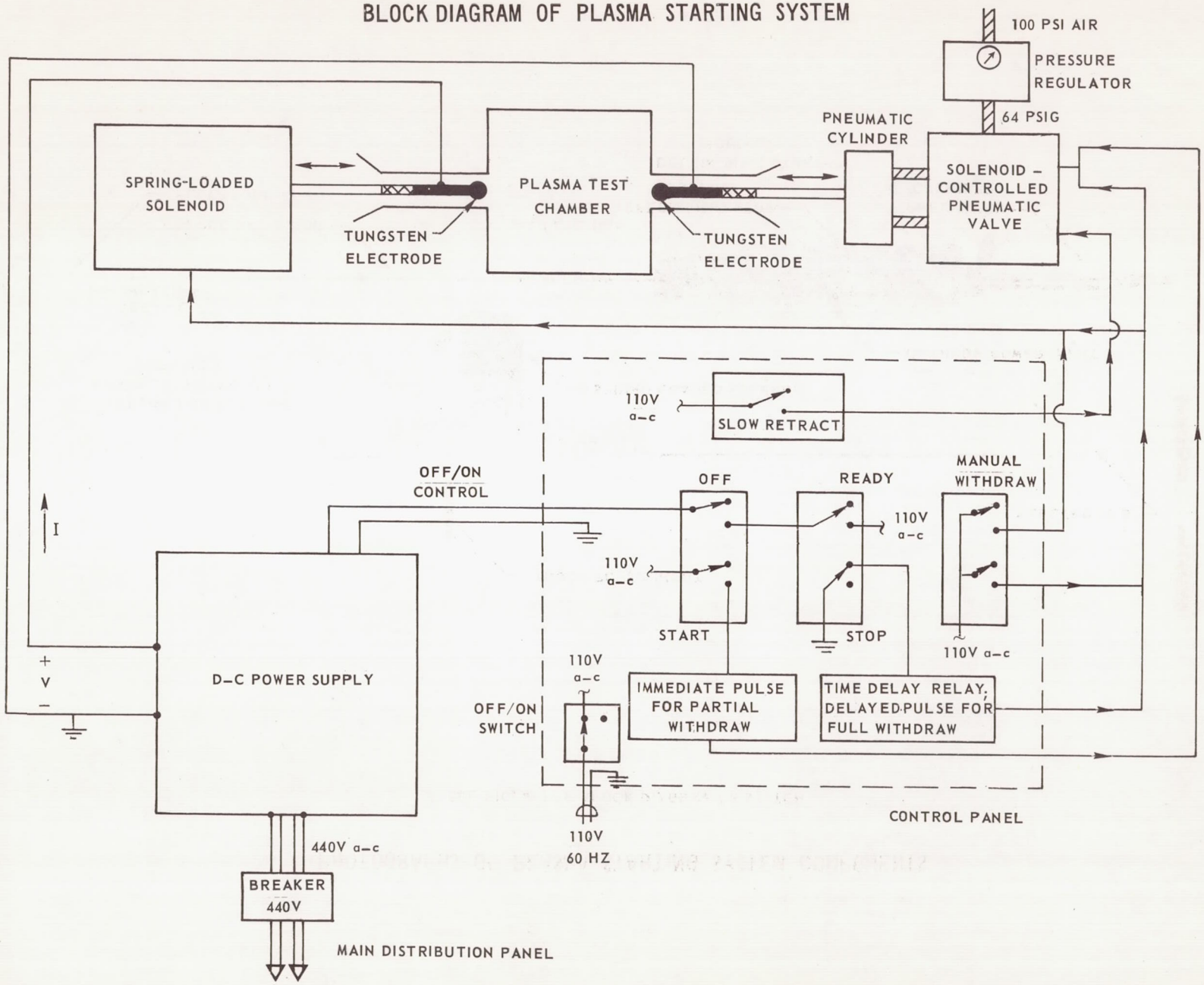

FIG. 4

PHOTOGRAPHS OF PLASMA STARTING SYSTEM COMPONENTS

SEE FIG. 4 FOR BLOCK DIAGRAM OF SYSTEM

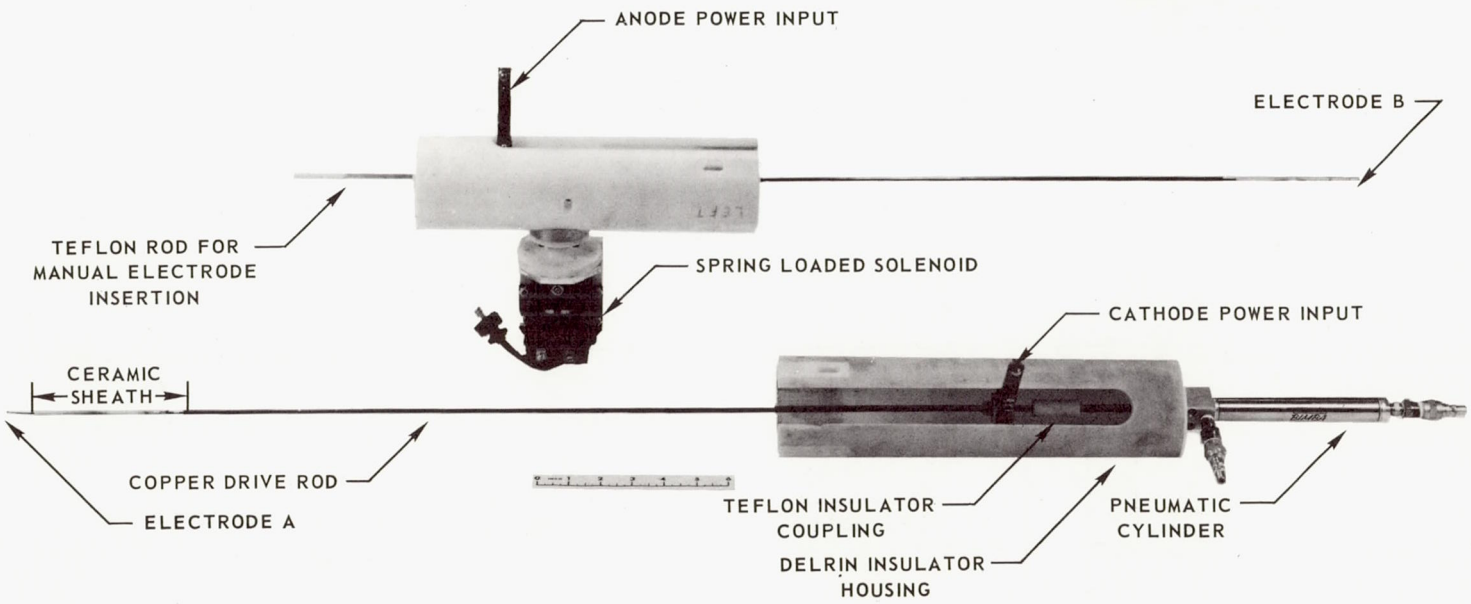

FIG. 5

PHOTOGRAPHS OF PLASMA STARTING SEQUENCE

DETAILS OF PLASMA STARTING SYSTEM GIVEN IN FIGS. 4 AND 5

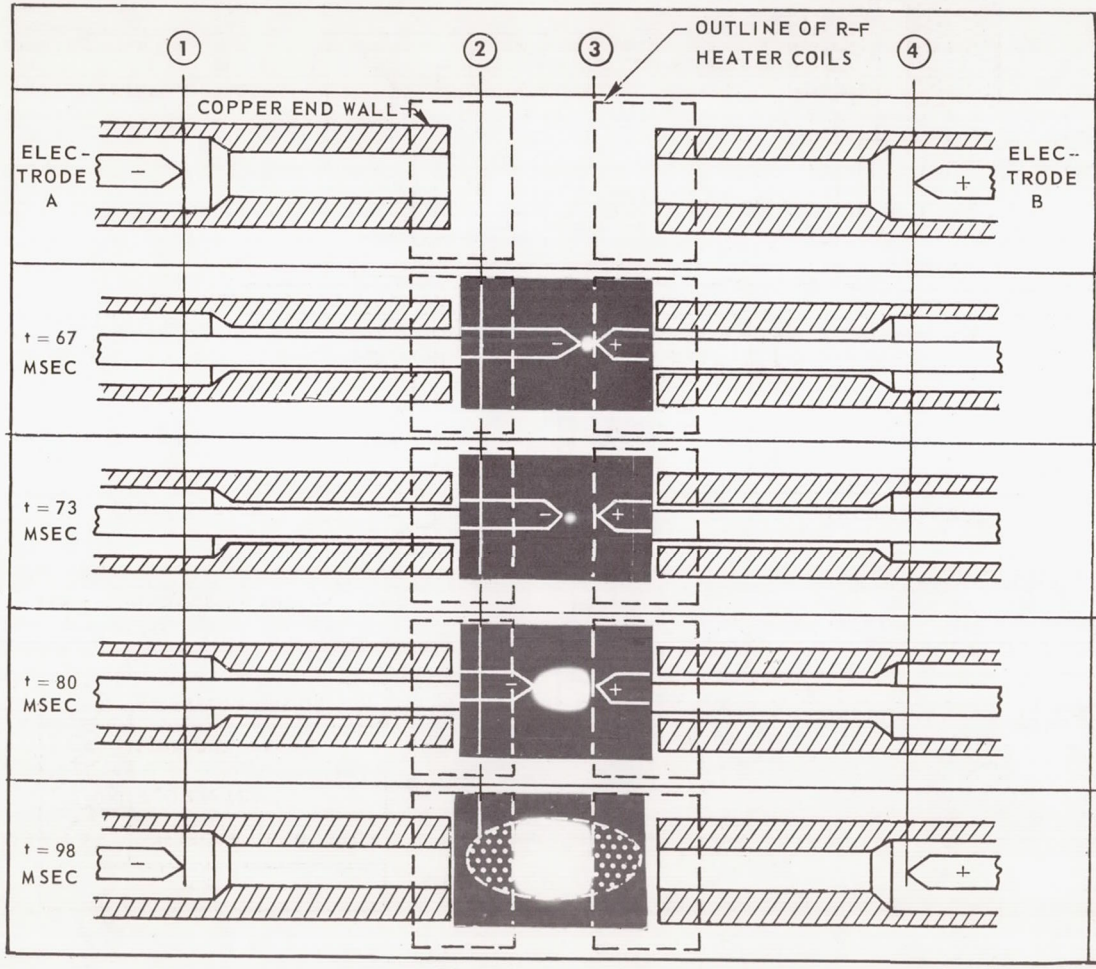

EVENT
NORMAL CONDITION – A AND B ELECTRODES FULLY WITHDRAWN INSIDE END WALLS
READY TO START – A AND B ELECTRODES CONTACT AT ③; AT t = 0 D-C POWER ON; D-C ARC INITIATED
ELECTRODE A WITHDRAWN; ELECTRODE B REMAINS FIXED; D-C ARC IS BEING DRAWN FROM POSITION ③ TO ②
PARTIAL TRANSITION FROM D-C TO R-F MODE; D-C ARC REMAINS UNTIL R-F HEATER CAN MAINTAIN THE DISCHARGE
R-F FULLY ESTABLISHED; D-C ARC POWER OFF – A AND B ELECTRODES FULLY WITHDRAWN

FIG. 6

SCHEMATIC OF PARTICLE SEEDING SYSTEM

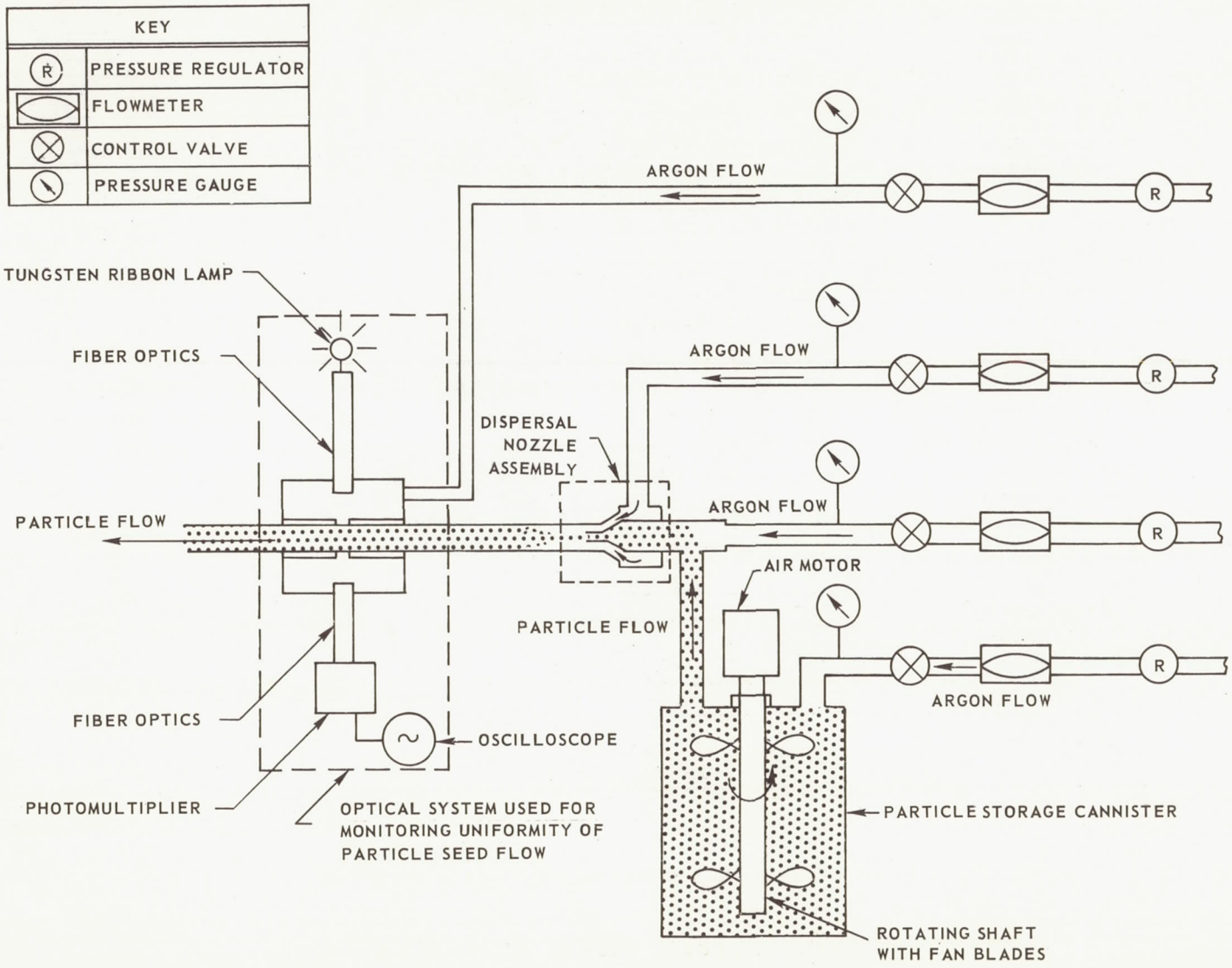

FIG. 7

FIG. 8

DETAILS OF PARTICLE SEEDING SYSTEM

a) PHOTOGRAPH OF SYSTEM

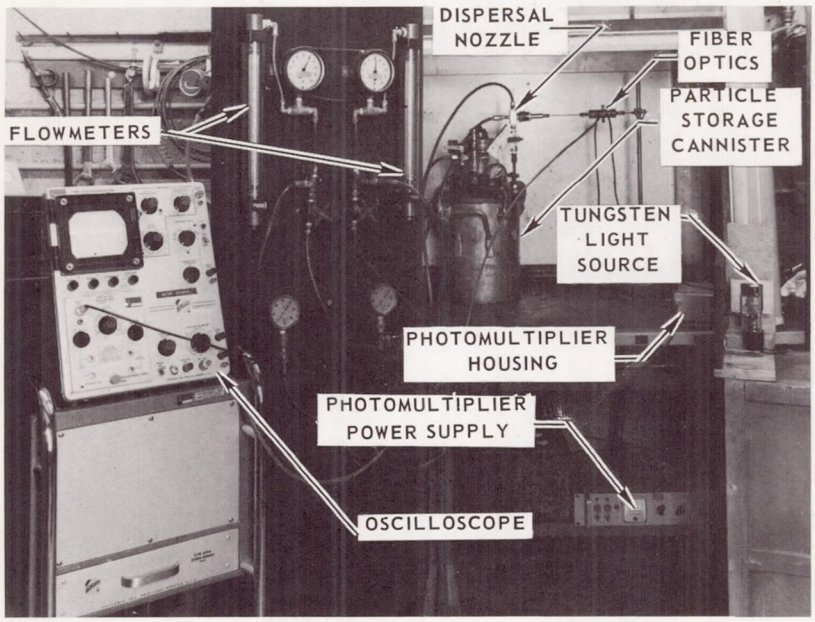

b) TIME VARIATION OF LIGHT TRANSMITTED THROUGH FLOW OF 0.004 TO 0.012-MICRON-DIA CARBON PARTICLES

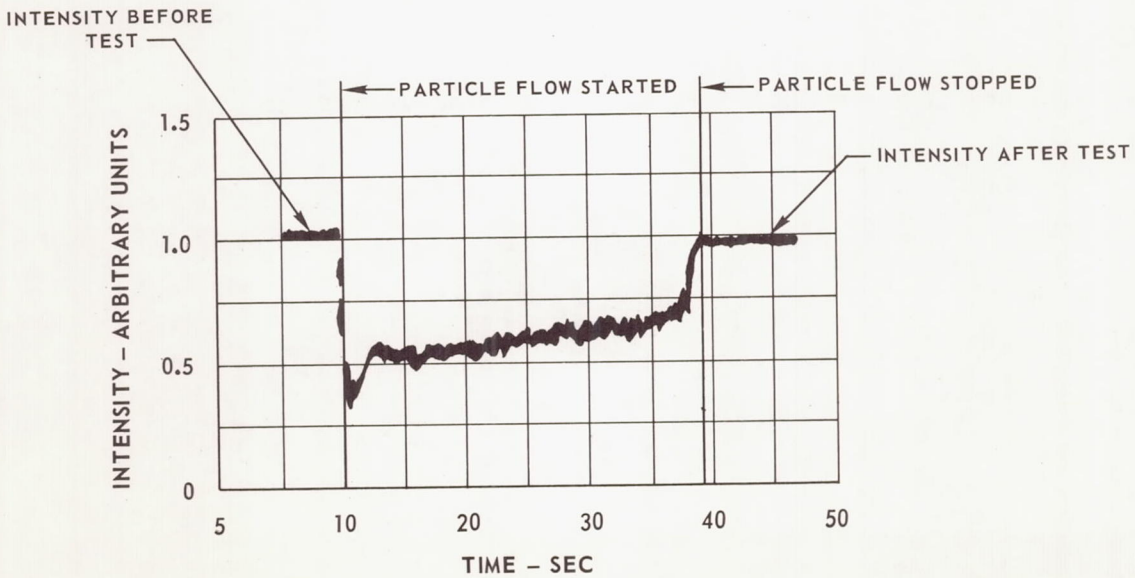

FIG. 9

ELECTRON MICROSCOPE PHOTOGRAPHS OF SUBMICRON PARTICLES

a) CARBON (CARBOLAC 2; 0.004 TO 0.012–μ AVERAGE PARTICLE SIZE)

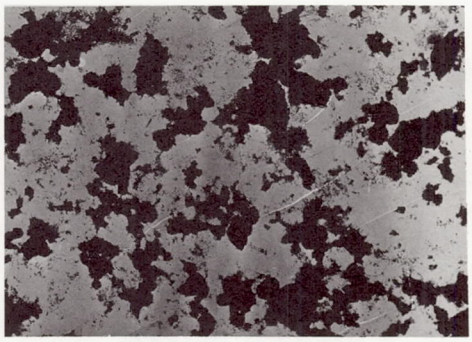

1μ AT 4000X

b) TUNGSTEN (0.02 TO 0.06–μ AVERAGE PARTICLE SIZE)

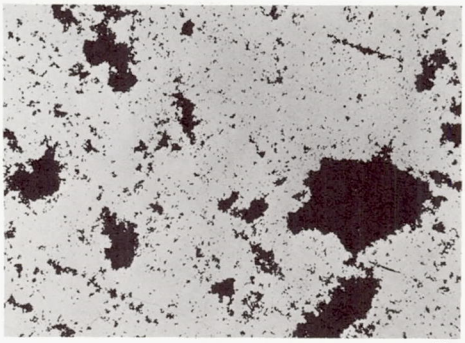

1μ AT 4000X

c) CARBON (CABOT STERLING MT; 0.250 TO 0.462–μ AVERAGE PARTICLE SIZE)

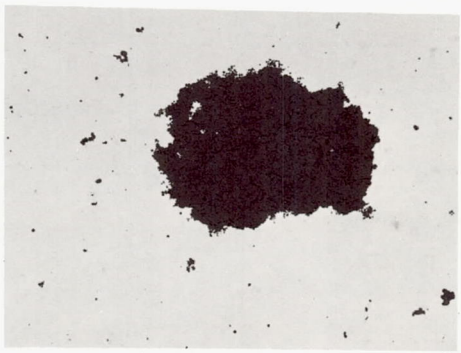

1μ AT 4000X

BLOCK DIAGRAM OF RADIOMETER OPTICAL SYSTEM AND OSCILLOSCOPE TRACE OF TYPICAL OUTPUT

a) BLOCK DIAGRAM

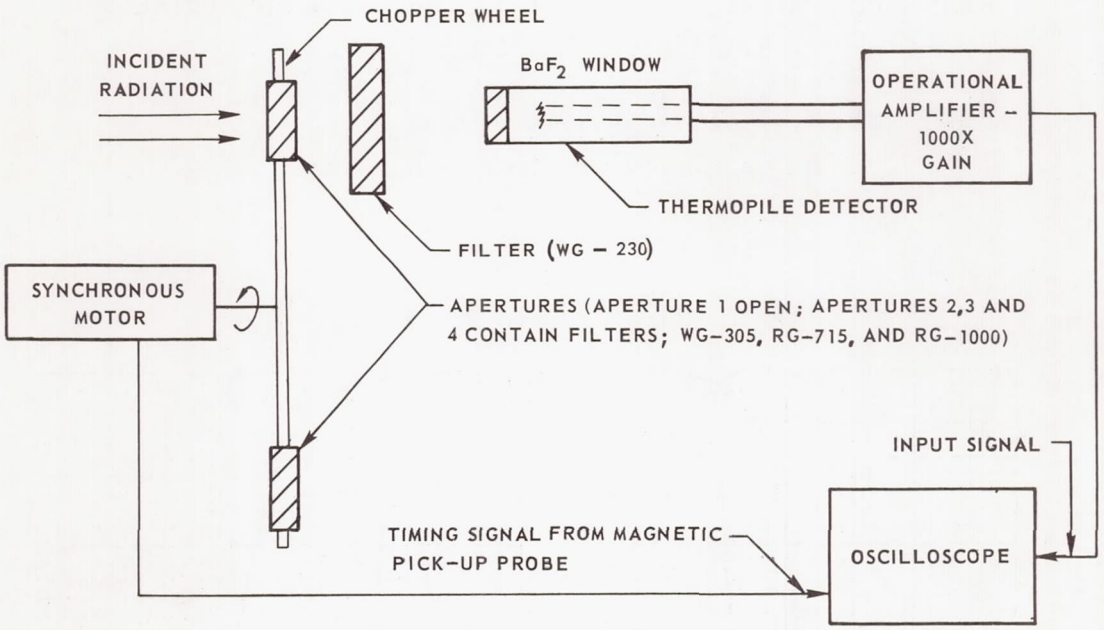

b) OSCILLOSCOPE TRACE

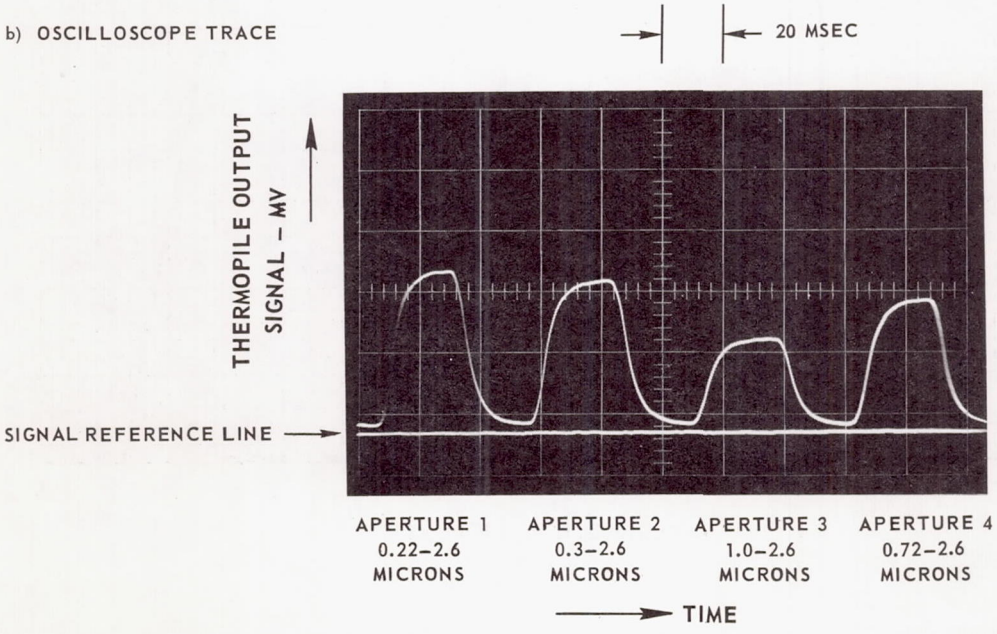

TRANSMISSION CHARACTERISTICS OF FILTERS USED FOR TOTAL RADIATION MEASUREMENTS

FILTER THICKNESS – 0.079 IN.

SEE FIG. 10 FOR RADIOMETER OPTICAL SYSTEM

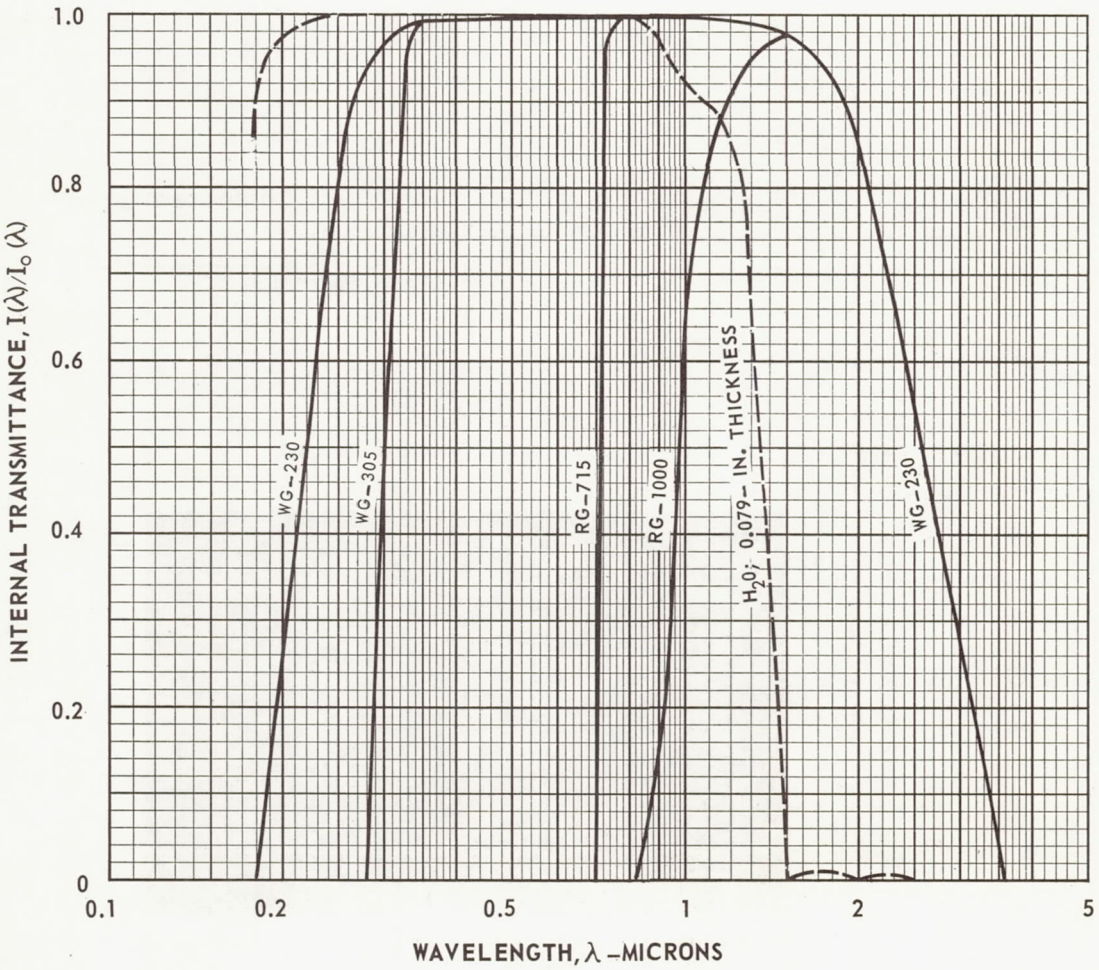

FIG. 12

SCHEMATIC OF OPTICAL SYSTEM USED FOR SPECTRAL MEASUREMENTS

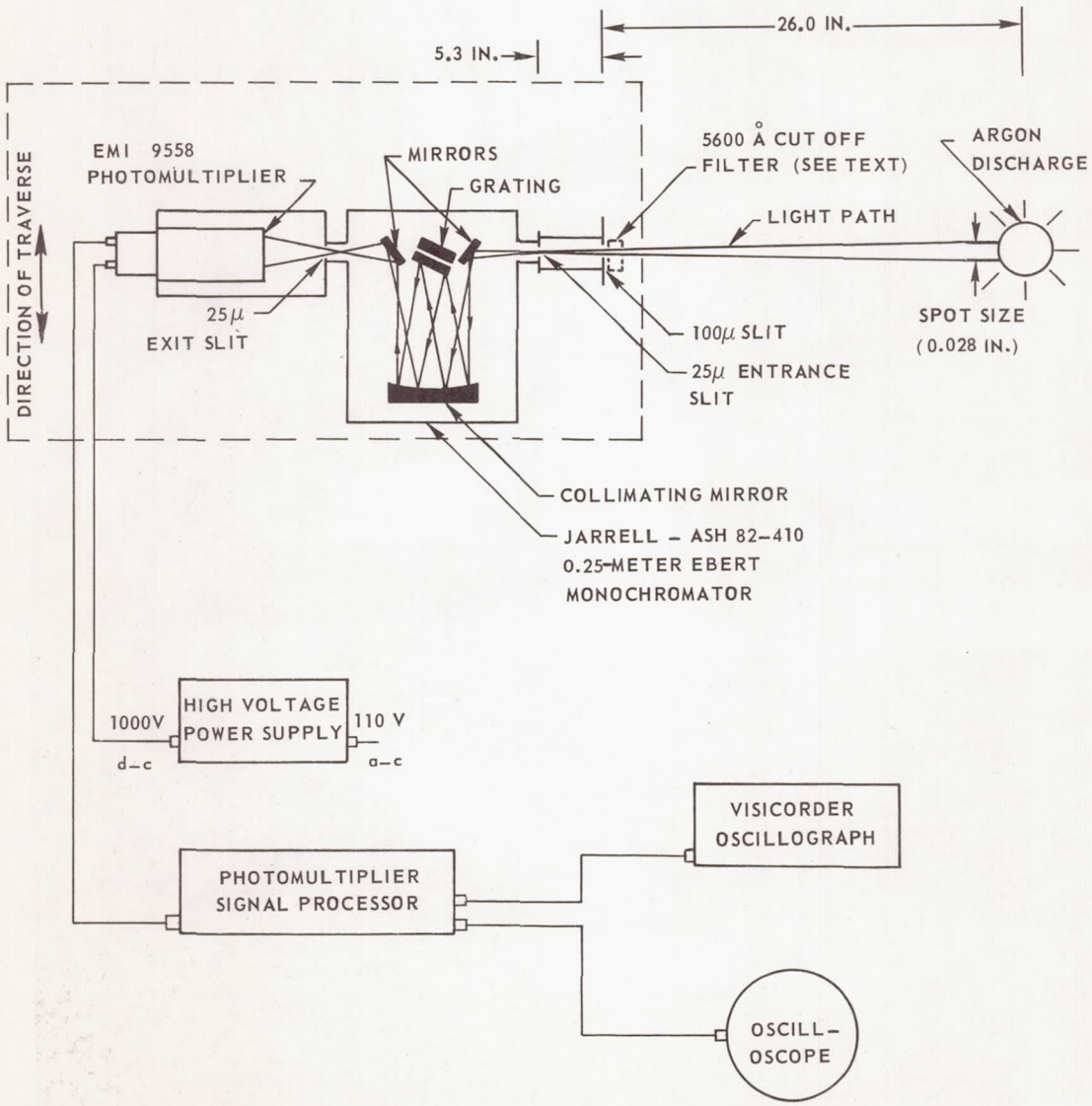

FIG. 13

PHOTOGRAPH OF EQUIPMENT USED FOR SPECTRAL EMISSION MEASUREMENTS

SEE FIG. 12 FOR OPTICAL SYSTEM DETAILS

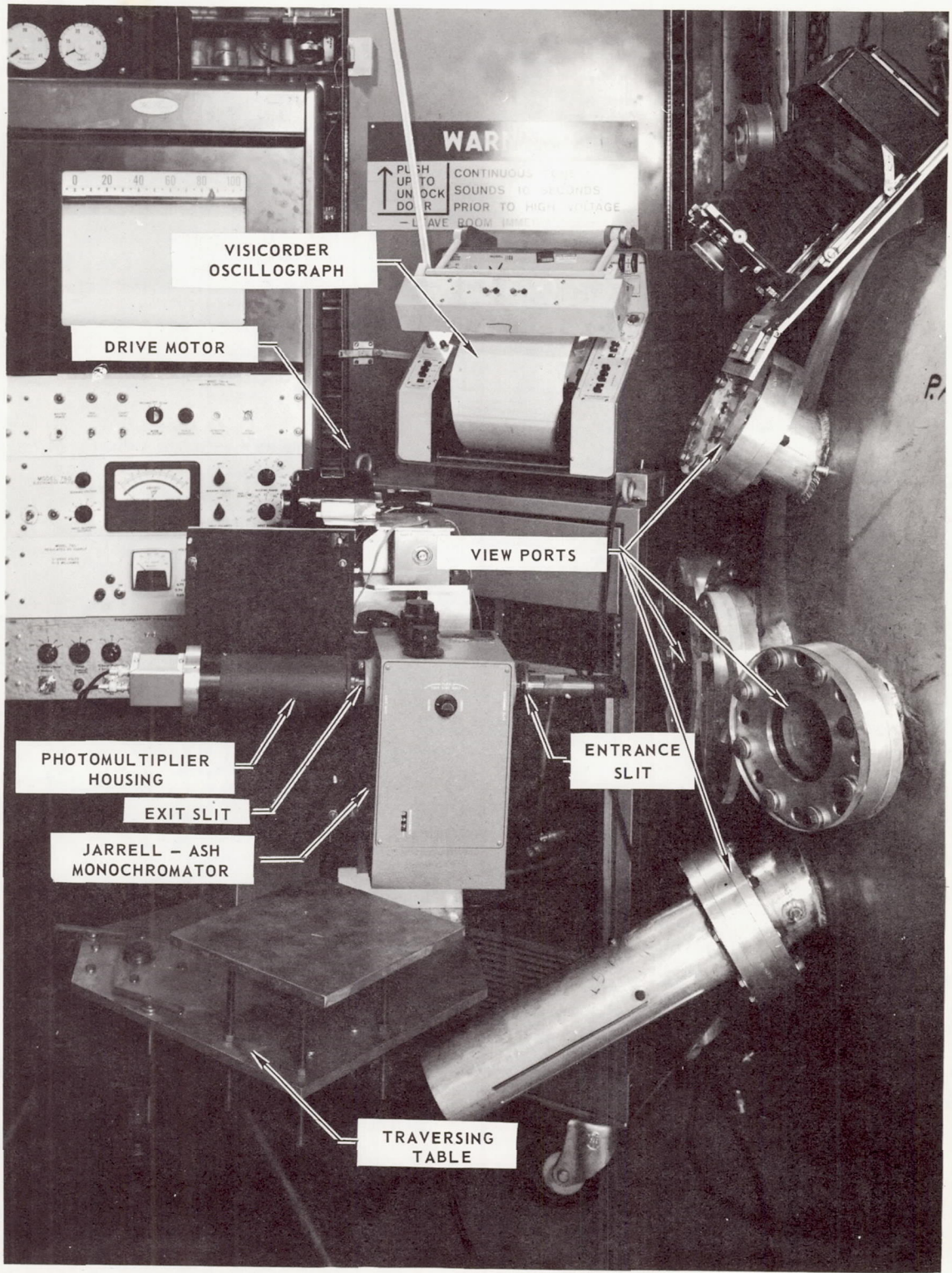

RL–68–207–A

FIG. 14

TYPICAL EXPERIMENTAL TRACE OF RELATIVE INTENSITY AS A FUNCTION OF WAVELENGTH FOR ARGON DISCHARGE

REFERENCE TEMPERATURE = 9080 K

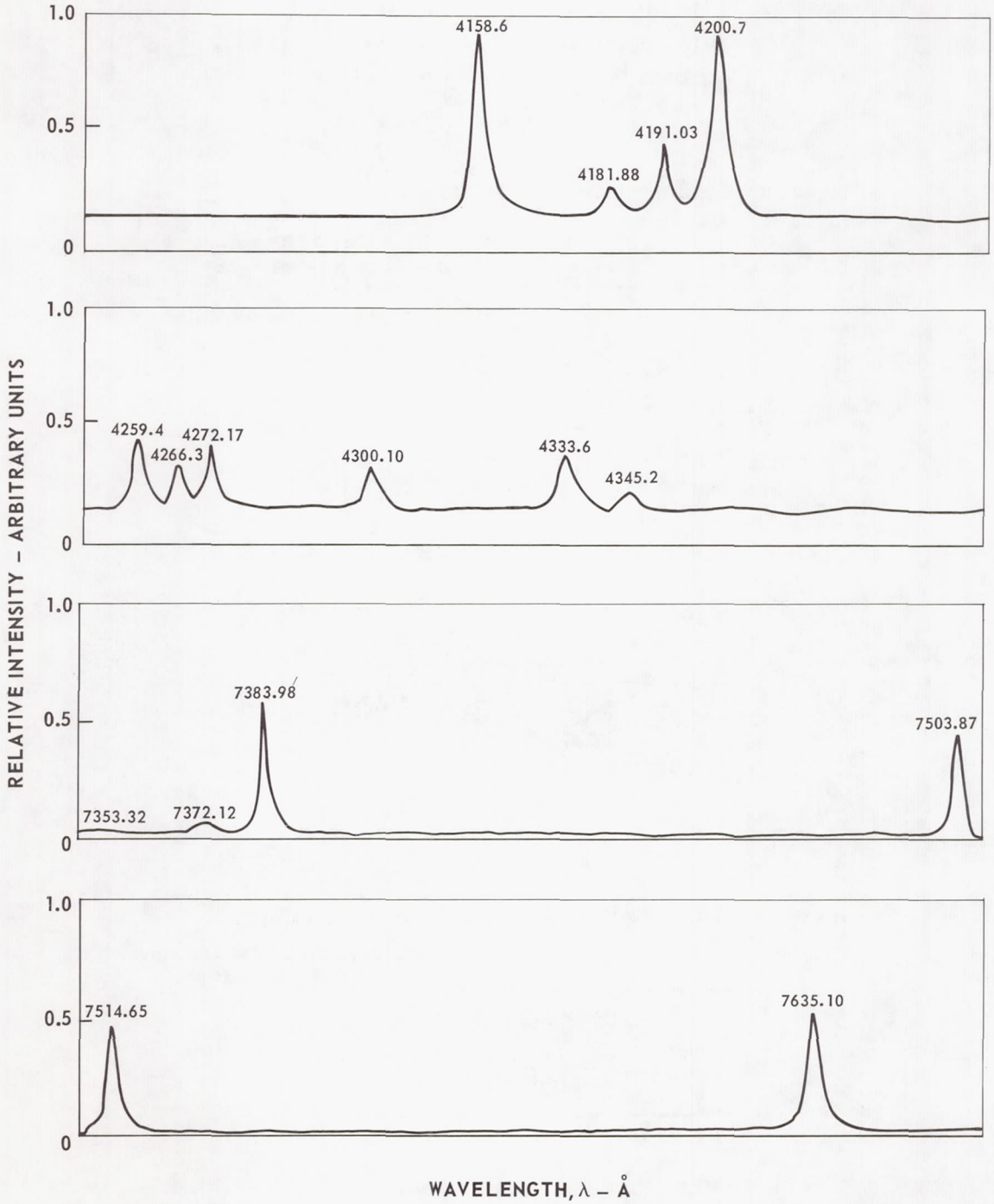

FIG. 15

TYPICAL PHOTOGRAPHS OF ARGON DISCHARGES FOR DETERMINATION OF DISCHARGE DIAMETER

DISCHARGE PRESSURE, P_D = 5.0 ATM

TOTAL DISCHARGE POWER, Q_T = 23.1 KW

EXPOSURE SETTINGS; f 22 AT 1/100TH SEC
FILM SPEED, ASA 3000

a) REFERENCE EXPOSURE (NO. 4.0–N.D. FILTER USED)

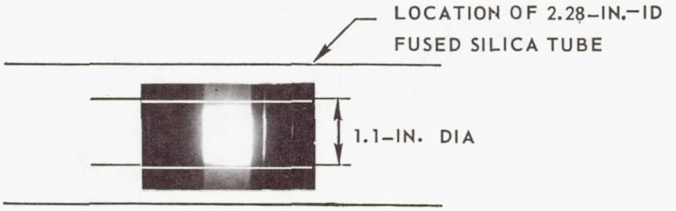

b) EXPOSURE EQUAL TO 1/10 th OF (a) (NO. 5.0–N.D. FILTER USED)

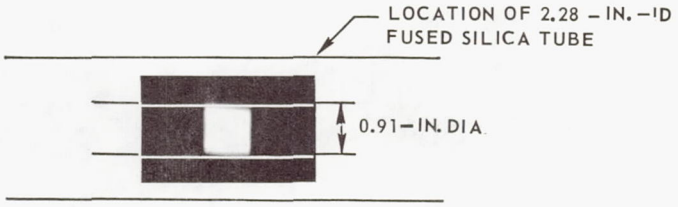

c) EXPOSURE EQUAL TO 1/32 nd OF (a) (NO. 5.5 –N.D. FILTER USED)

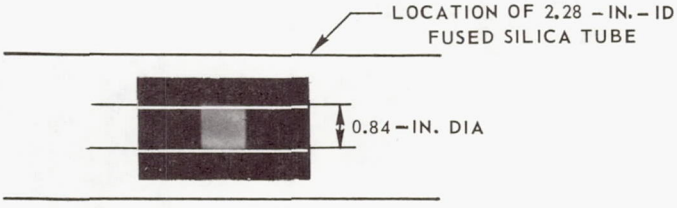

SKETCH OF RADIANT ENERGY SOURCE CONFIGURATION USED IN TESTS WITH UNSEEDED ARGON DISCHARGES

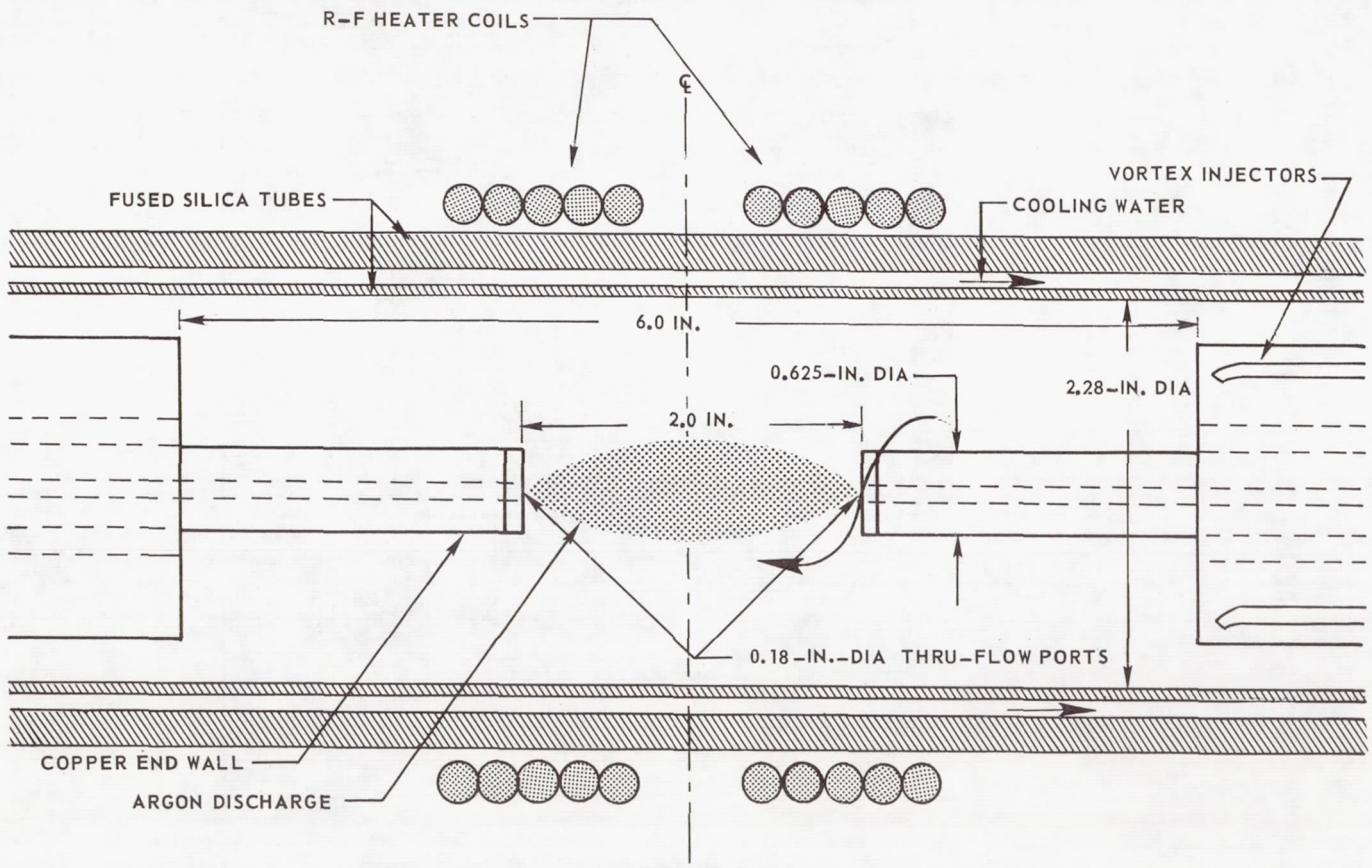

FIG. 16

ATOMIC BOLTZMANN PLOT FOR MEASUREMENTS ALONG DIAMETER OF ARGON DISCHARGE

DISCHARGE PRESSURE, $P_D = 3$ ATM

TOTAL DISCHARGE POWER, $Q_T = 15$ KW

ARGON WEIGHT FLOW, $W_A = 0.01$ LB/SEC

RADIUS OF DISCHARGE, $r_6 = 0.55$ IN.

VORTEX TUBE RADIUS, $r_1 = 1.14$ IN.

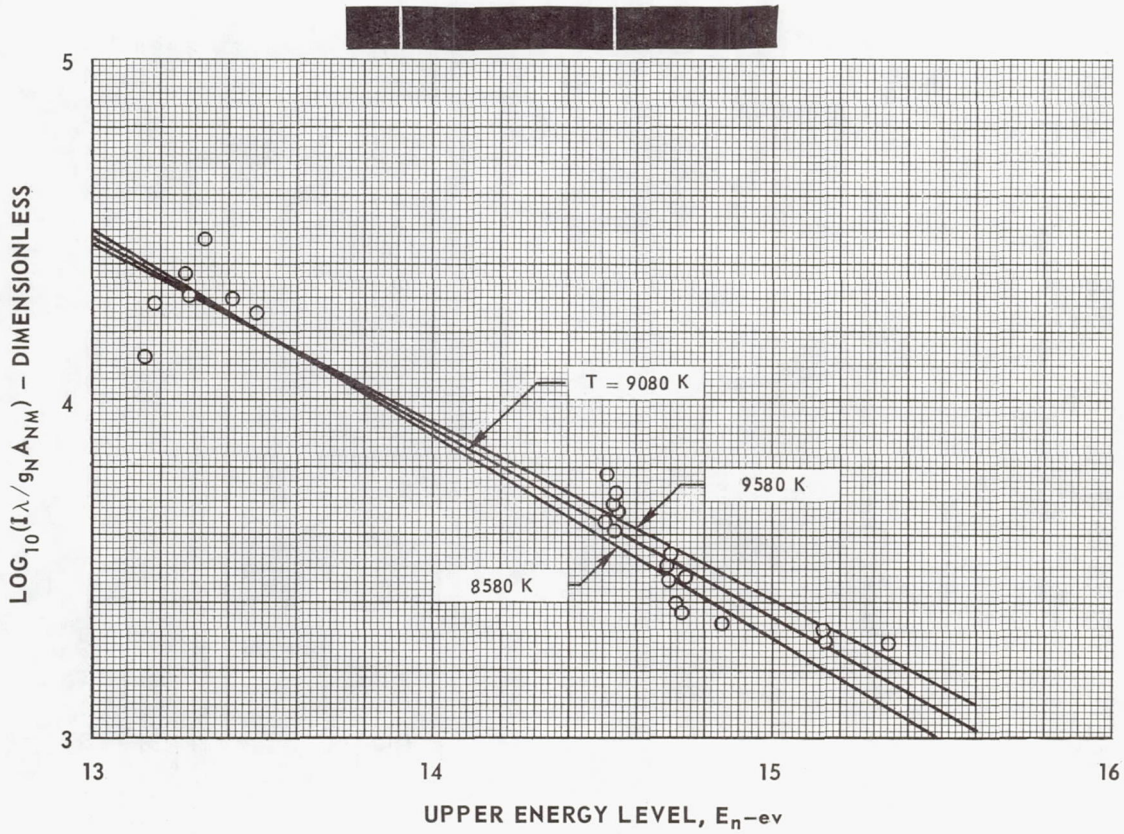

FIG. 18

TYPICAL VARIATIONS OF LINE INTENSITY AND TEMPERATURE IN AN ARGON DISCHARGE

DISCHARGE PRESSURE, $P_D = 3$ ATM

TOTAL DISCHARGE POWER, $Q_T = 15$ KW

ARGON WEIGHT FLOW, $W_A = 0.01$ LB/SEC

RADIUS OF DISCHARGE, $r_6 = 0.55$ IN.

VORTEX TUBE RADIUS, $r_1 = 1.14$ IN.

a) CHORDAL VARIATION OF INTENSITY

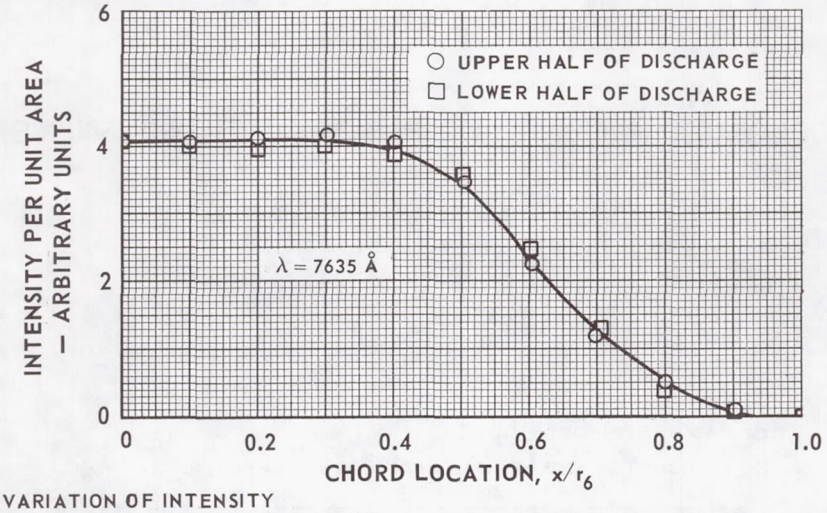

b) RADIAL VARIATION OF INTENSITY

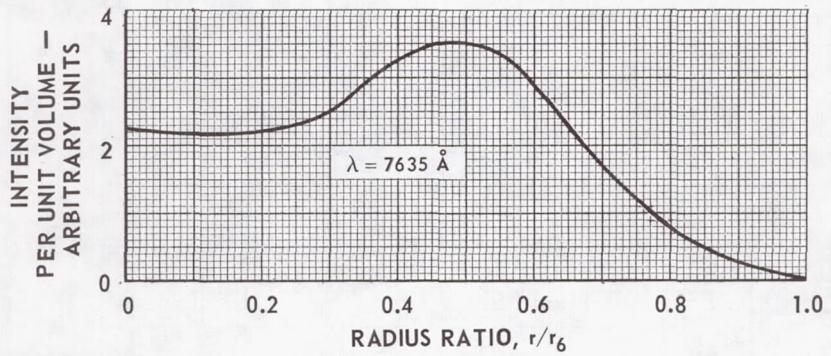

c) RADIAL VARIATION OF TEMPERATURE

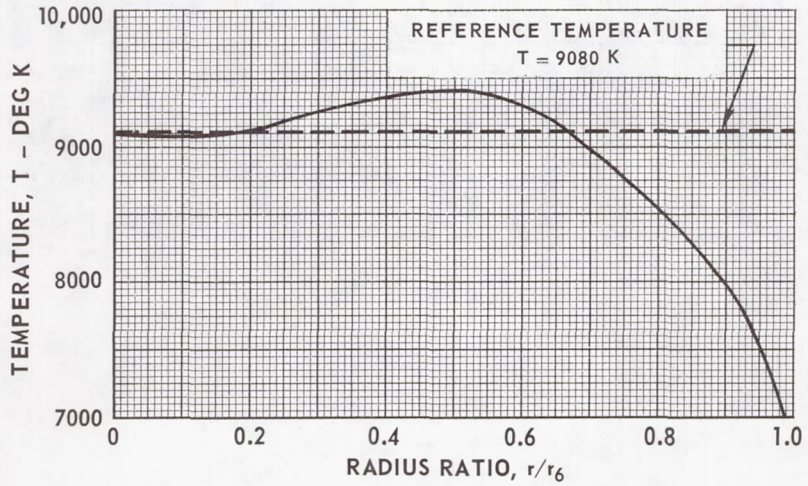

FIG. 19

EFFECT OF DISCHARGE PRESSURE ON POWER RADIATED FROM SOURCE

DETAILS OF TEST CONFIGURATION SHOWN IN FIG. 16 AND TABLE I
RANGE OF ARGON WEIGHT FLOW, W_A = 0.01 TO 0.012 LB/SEC
RANGE OF TOTAL DISCHARGE POWER, Q_T =14.4 TO 34.1 KW
NO SEED

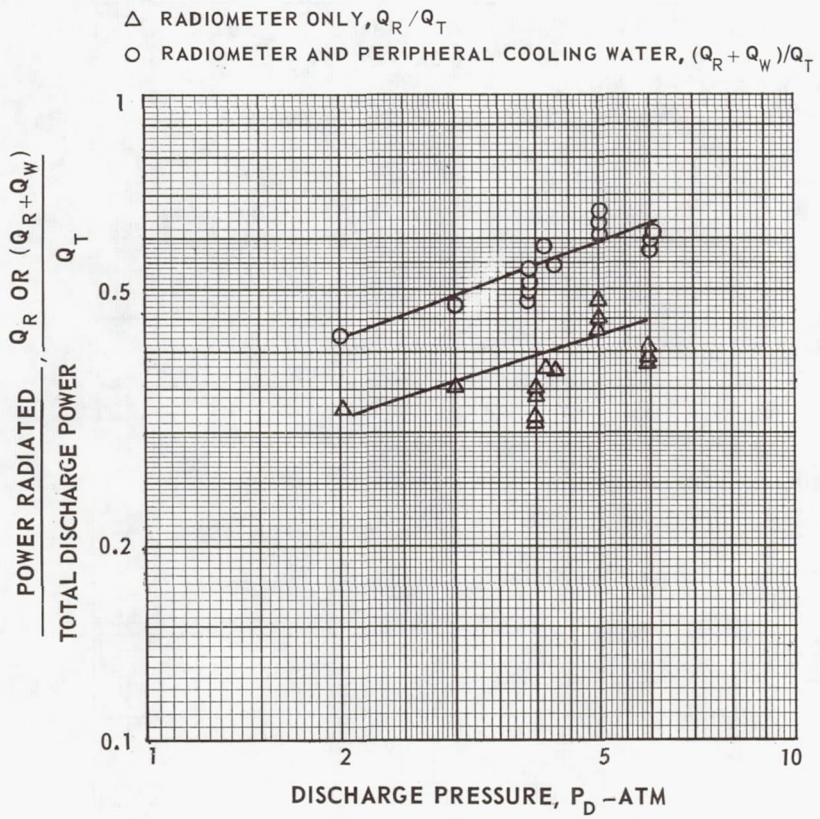

FIG. 20

EFFECT OF TOTAL DISCHARGE POWER ON POWER RADIATED FROM SOURCE

DETAILS OF TEST CONFIGURATION SHOWN IN FIG. 16 AND TABLE I

RANGE OF ARGON WEIGHT FLOW, W_A = 0.01 TO 0.025 LB/SEC

DISCHARGE PRESSURE, P_D = 6 ATM

NO SEED

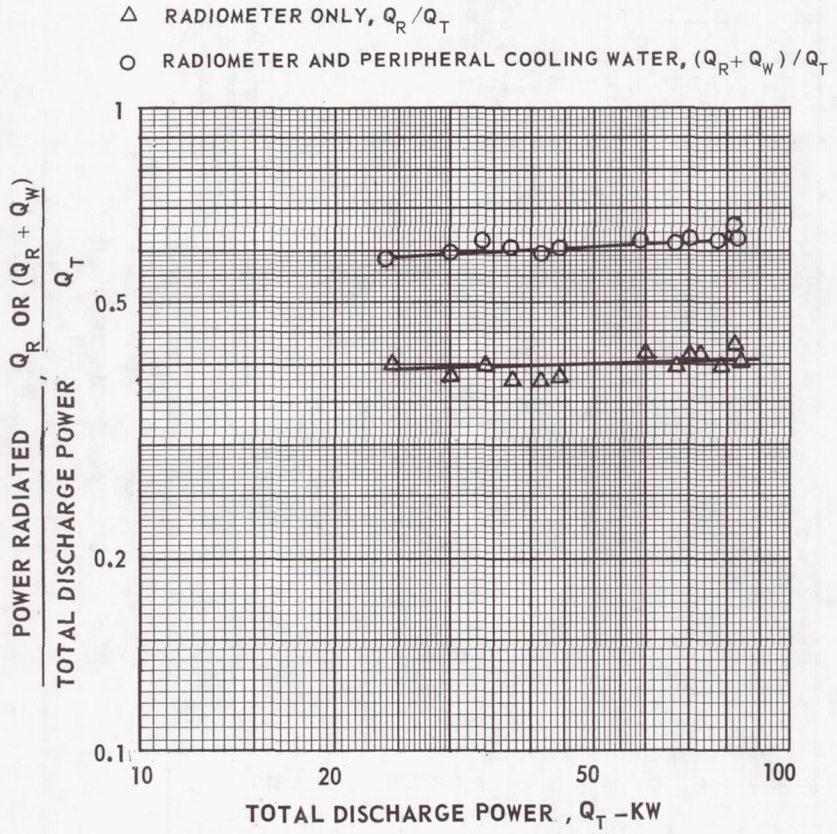

FIG. 21

GEOMETRY OF ARGON DISCHARGES OBTAINED IN TESTS USING THE RADIANT ENERGY SOURCE CONFIGURATION

DETAILS OF TEST CONFIGURATION SHOWN IN FIG. 16 AND TABLE I
DISCHARGE DIAMETER DETERMINED FROM PHOTOGRAPHS– SEE TEXT

SYMBOL	OPTICAL DENSITY OF FILTER USED	TRANSPARENCY OF FILTER, I_t / I_i	RANGE OF DISCHARGE PRESSURE, P_D – ATM	RANGE OF ARGON WEIGHT FLOW, W_A – LB/SEC
○	4.0	10^{-4}	2.0 TO 6.0	0.0094 TO 0.011
△	5.0	10^{-5}	2.0 TO 5.0	
□	5.5	$10^{-5.5}$	2.0 TO 6.0	
◇	6.5	$10^{-6.5}$	6.0	0.023 TO 0.025

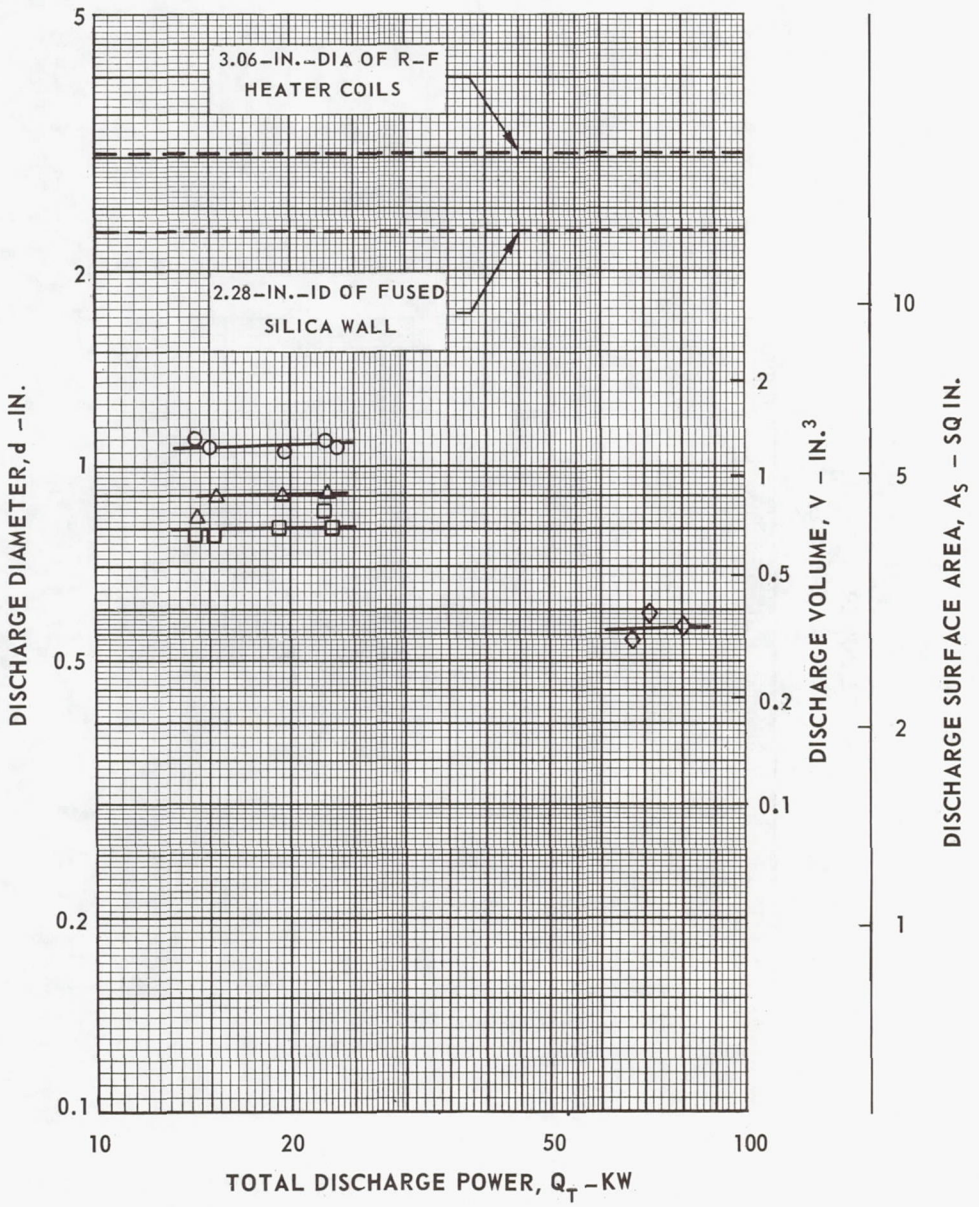

FIG. 22

VARIATION OF DISCHARGE POWER PER UNIT VOLUME WITH TOTAL DISCHARGE POWER

DETAILS OF TEST CONFIGURATION SHOWN IN FIG. 16 AND TABLE I

DISCHARGE VOLUME DETERMINED FROM PHOTOGRAPHS – SEE TEXT

SYMBOL	OPTICAL DENSITY OF FILTER USED	TRANSPARENCY OF FILTER, I_t/I_i	RANGE OF DISCHARGE PRESSURE, P_D – ATM	RANGE OF ARGON WEIGHT FLOW, W_A – LB/SEC
○	4.0	10^{-4}	2.0 TO 6.0	0.0094 TO 0.011
△	5.0	10^{-5}	2.0 TO 5.0	
□	5.5	$10^{-5.5}$	2.0 TO 6.0	
◇	6.5	$10^{-6.5}$	6.0	0.023 TO 0.025

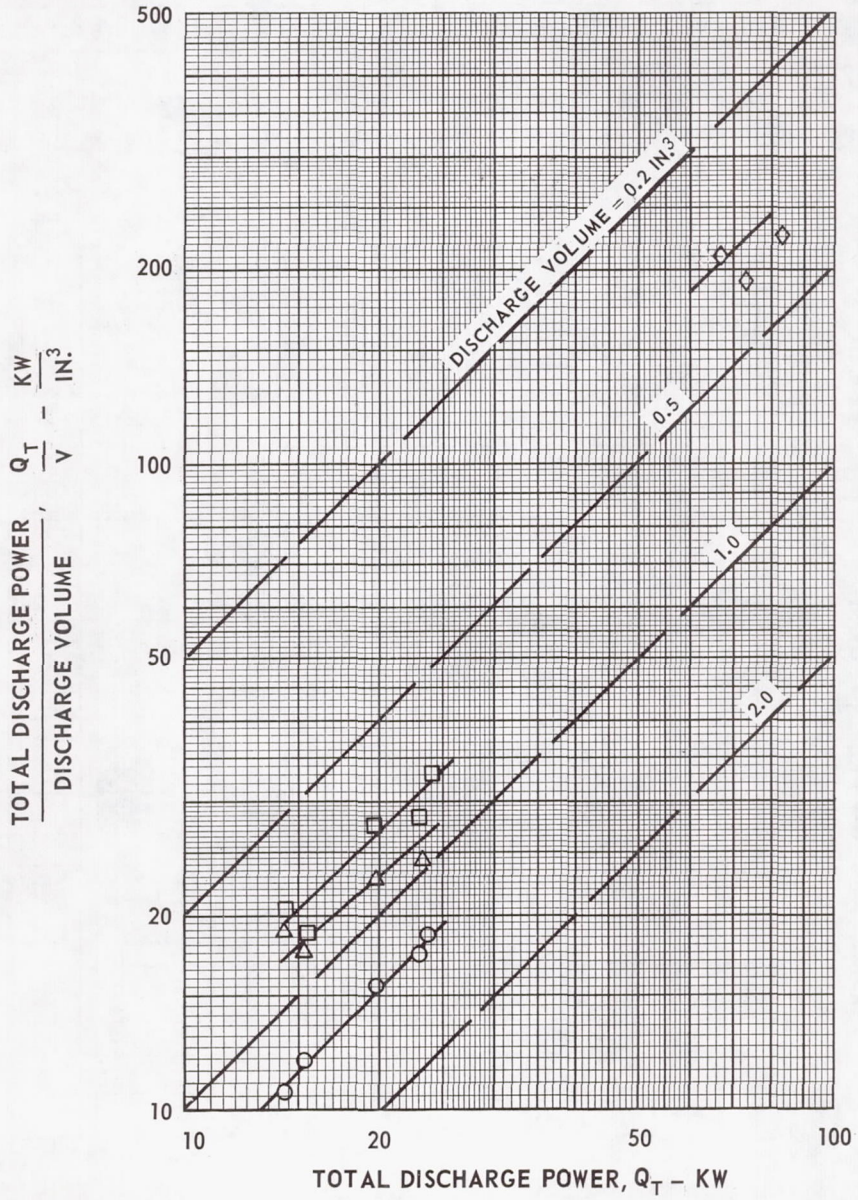

FIG. 23

VARIATION OF RADIANT ENERGY FLUX WITH TOTAL DISCHARGE POWER

DETAILS OF TEST CONFIGURATION SHOWN IN FIG. 16 AND TABLE I

DISCHARGE VOLUME DETERMINED FROM PHOTOGRAPHS – SEE TEXT

SYMBOL	OPTICAL DENSITY OF FILTER USED	TRANSPARENCY OF FILTER I_t/I_i	RANGE OF DISCHARGE PRESSURE, P_D – ATM	RANGE OF ARGON WEIGHT FLOW, W_A – LB SEC
○ ●	4.0	10^{-4}	2.0 TO 6.0	0.0094 TO 0.011
△ ▲	5.0	10^{-5}	2.0 TO 5.0	
□ ■	5.5	$10^{-5.5}$	2.0 TO 6.0	
◇ ◆	6.5	$10^{-6.5}$	6.0	0.023 TO 0.025

OPEN SYMBOLS DENOTE RADIOMETER ONLY, Q_R/A_S – KW/IN.^{2}

SOLID SYMBOLS DENOTE RADIOMETER AND PERIPHERAL COOLING WATER, $(Q_R + Q_W)/A_S$ – KW/IN.^{2}

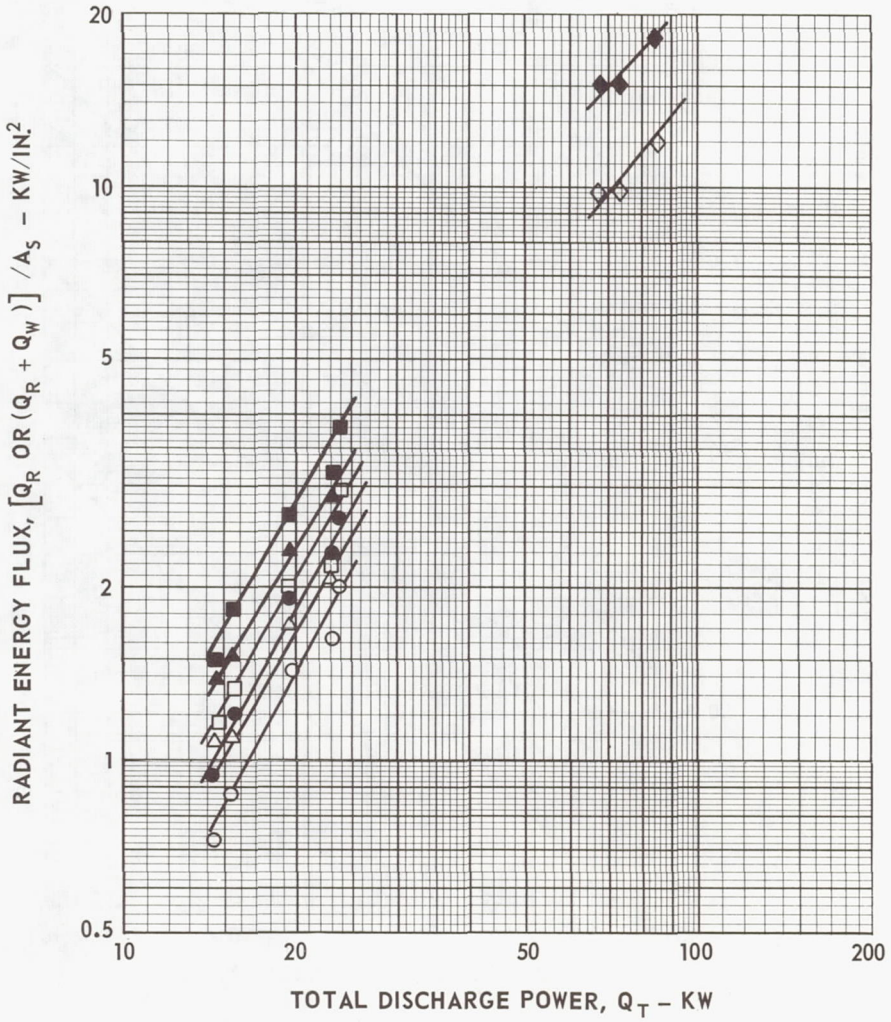

SKETCH OF RADIANT ENERGY SOURCE CONFIGURATION USED IN TESTS WITH SEEDED DISCHARGES

SEE TABLE I FOR DETAILS OF CONFIGURATION

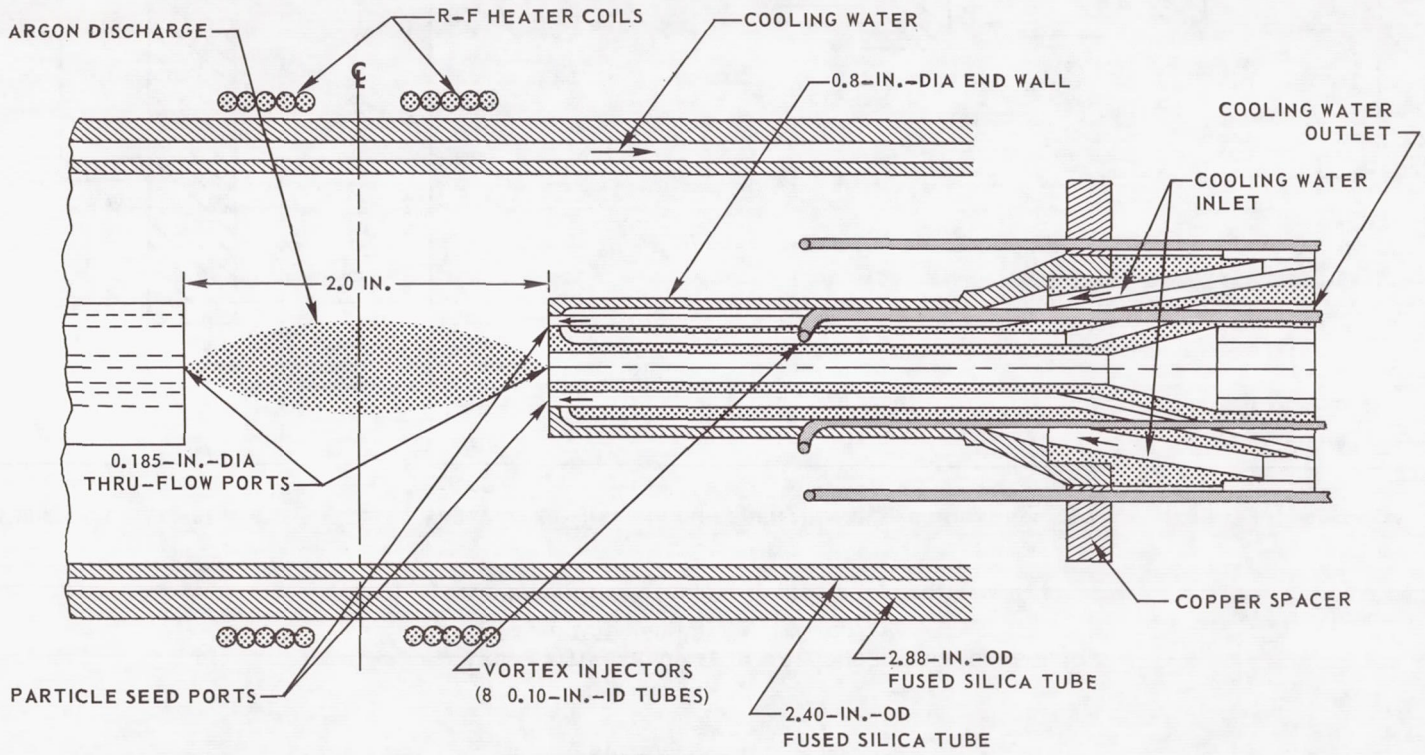

FIG. 24

COMPARISON OF SPECTRAL EMISSION IN DIFFERENT WAVELENGTH BANDS WITH AND WITHOUT CARBON SEED PARTICLES

ARGON WEIGHT FLOW, W_A = 0.0044 LB/SEC

DISCHARGE PRESSURE, P_D = 1.8 ATM

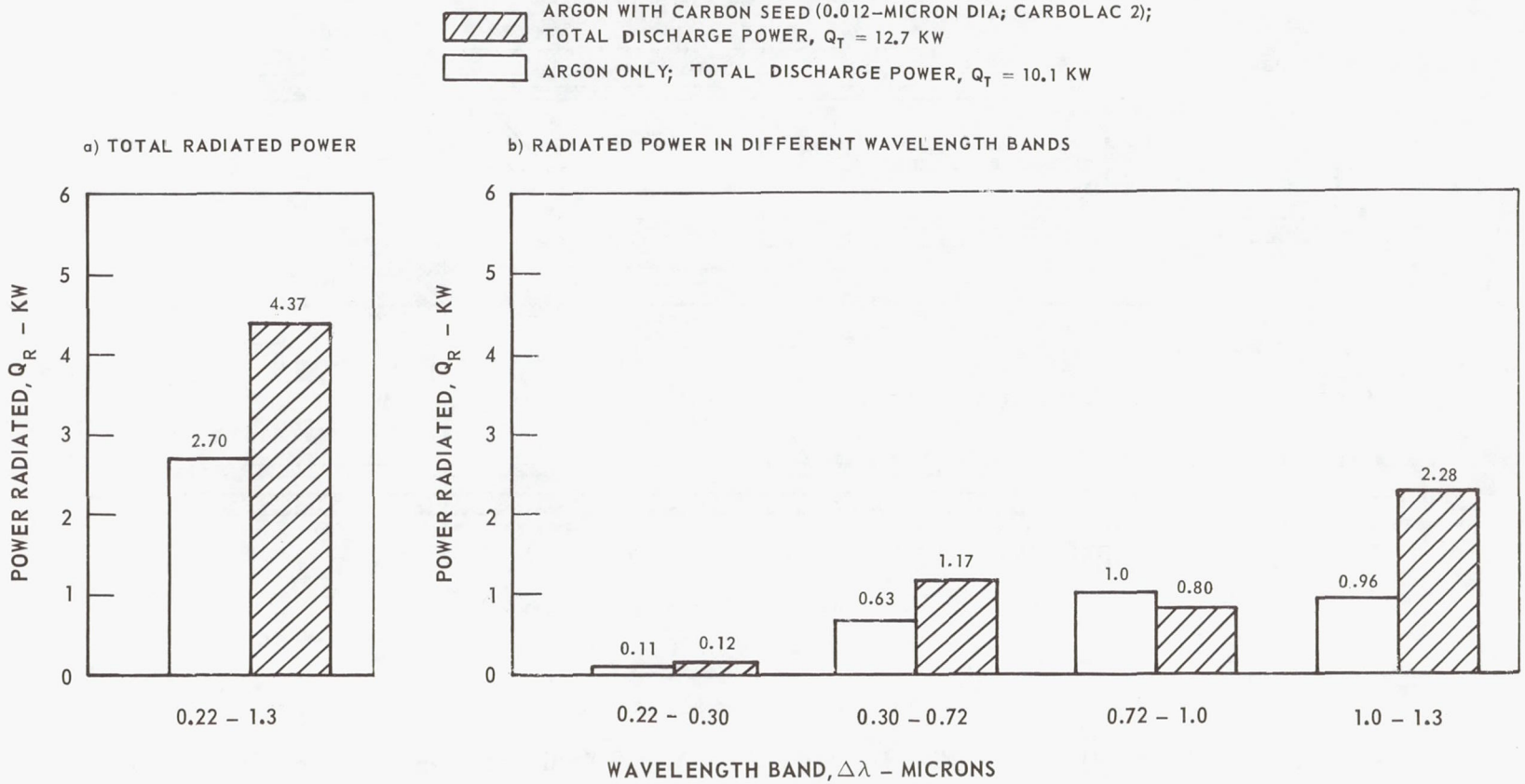

FIG. 25

PHOTOGRAPHS OF MODEL ASSEMBLIES FOR TESTS OF TRANSPARENT-WALL CONFIGURATIONS

SEE FIGS. 27-29 AND TABLE I FOR DETAILS OF TEST CONFIGURATIONS

a) END-WALL VORTEX INJECTION

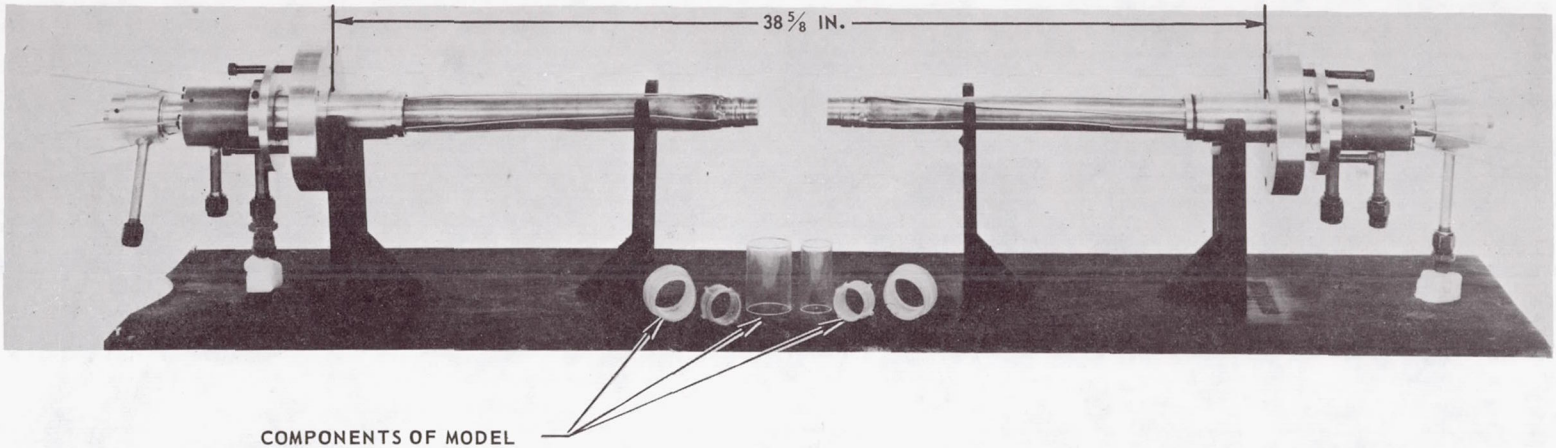

b) PERIPHERAL-WALL VORTEX INJECTION

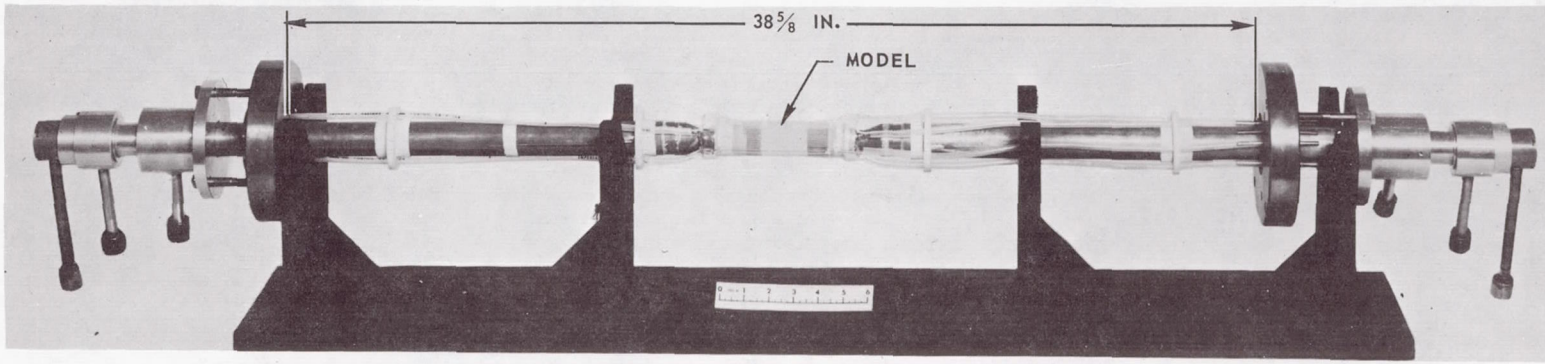

FIG. 26

FIG. 27

PHOTOGRAPHS OF END WALLS FOR TESTS OF TRANSPARENT – WALL CONFIGURATIONS

SEE FIG. 26 FOR PHOTOGRAPHS OF END–WALL AND MODEL ASSEMBLIES

a) END–WALL VORTEX INJECTION

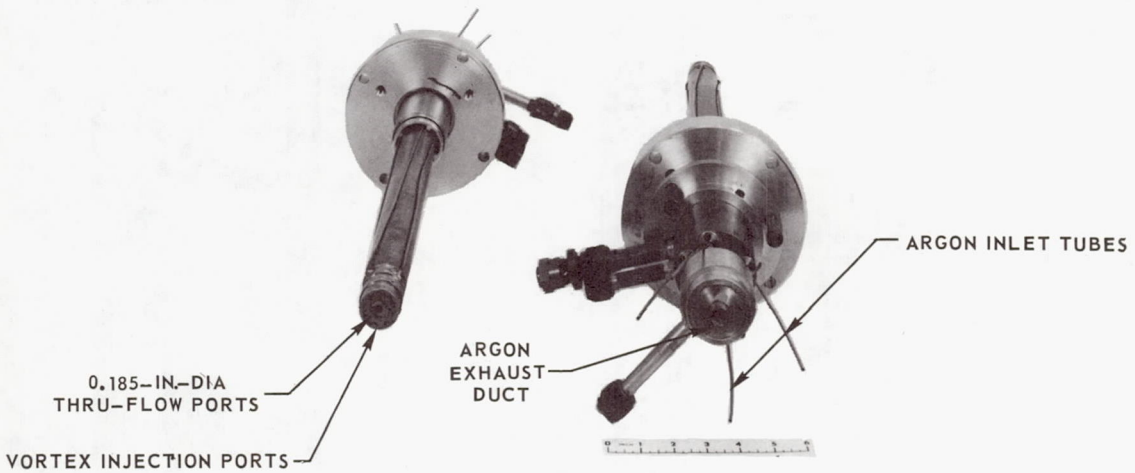

b) PERIPHERAL–WALL VORTEX INJECTION

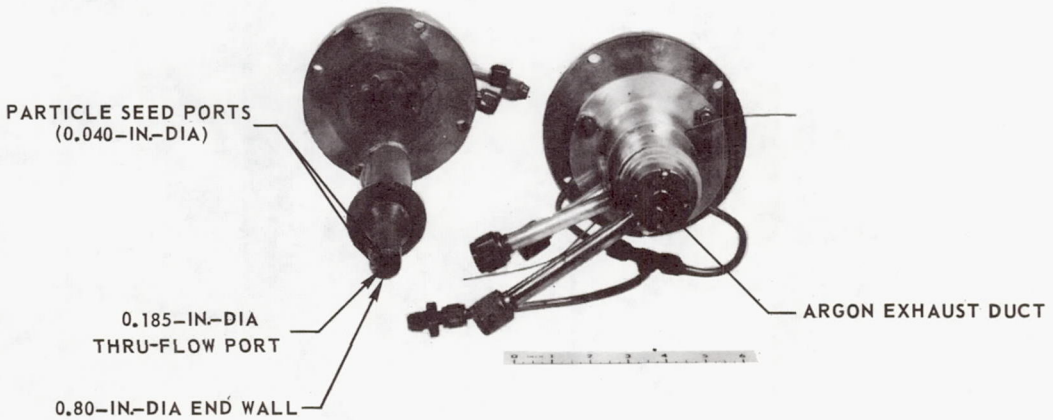

FIG. 28

TRANSPARENT – WALL MODEL USED IN TESTS WITH END–WALL VORTEX INJECTION

a) PHOTOGRAPH OF MODEL

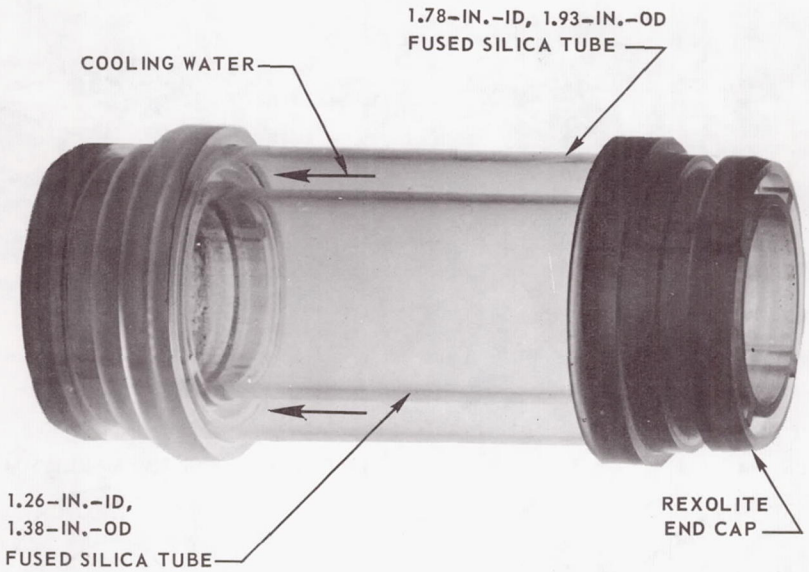

b) SKETCH OF MODEL

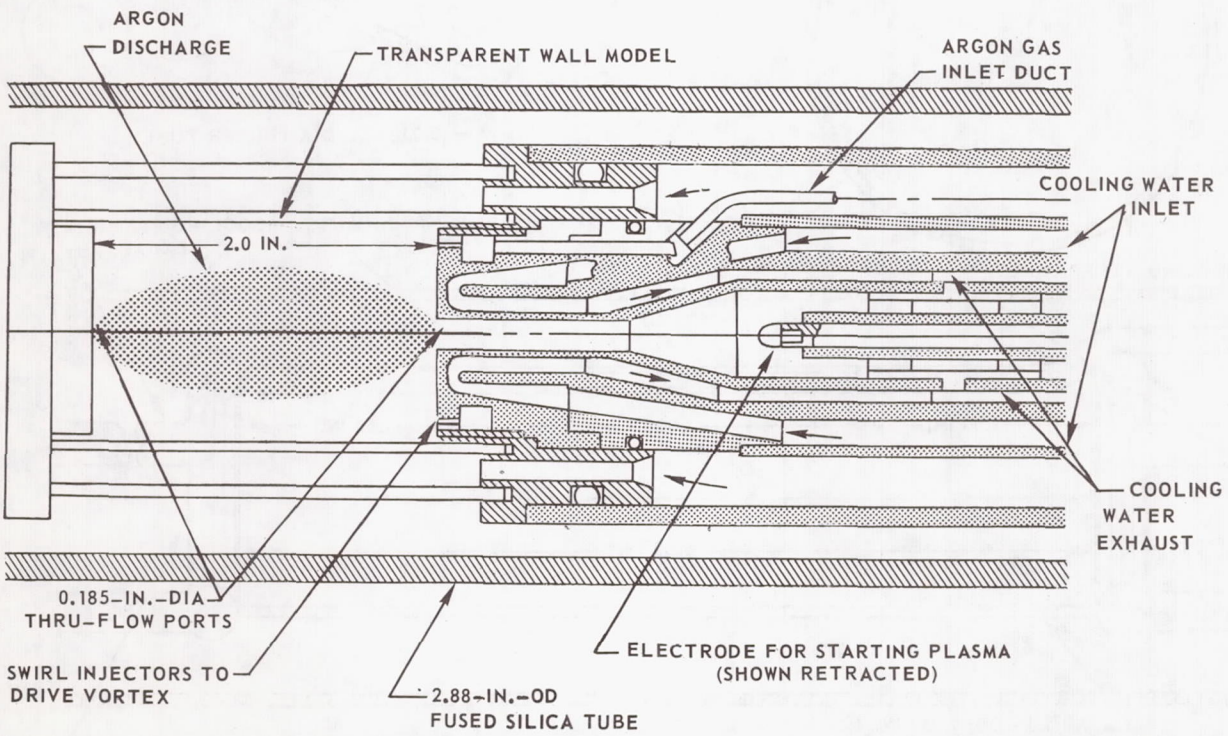

FIG. 29

TRANSPARENT – WALL MODEL USED IN TESTS WITH PERIPHERAL – WALL VORTEX INJECTION

a) PHOTOGRAPH OF MODEL

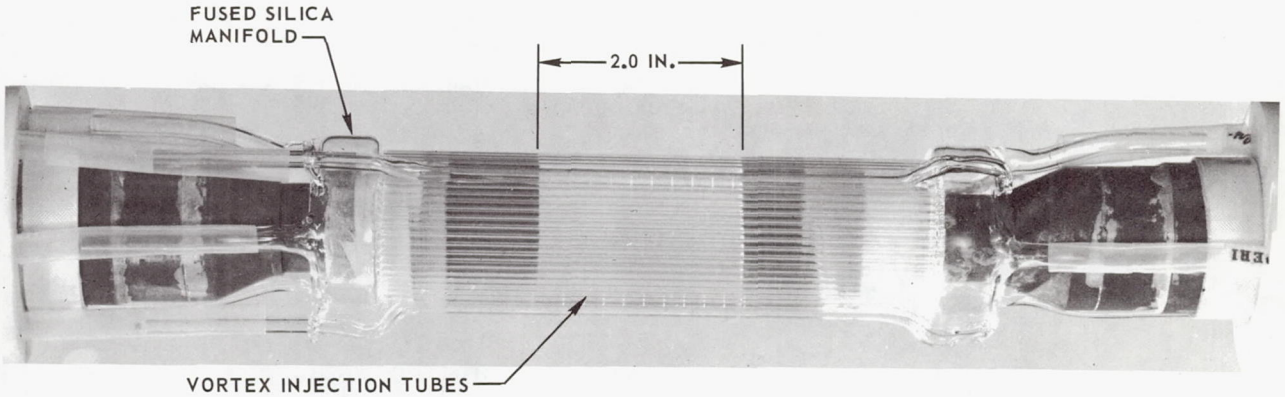

b) SKETCH OF MODEL

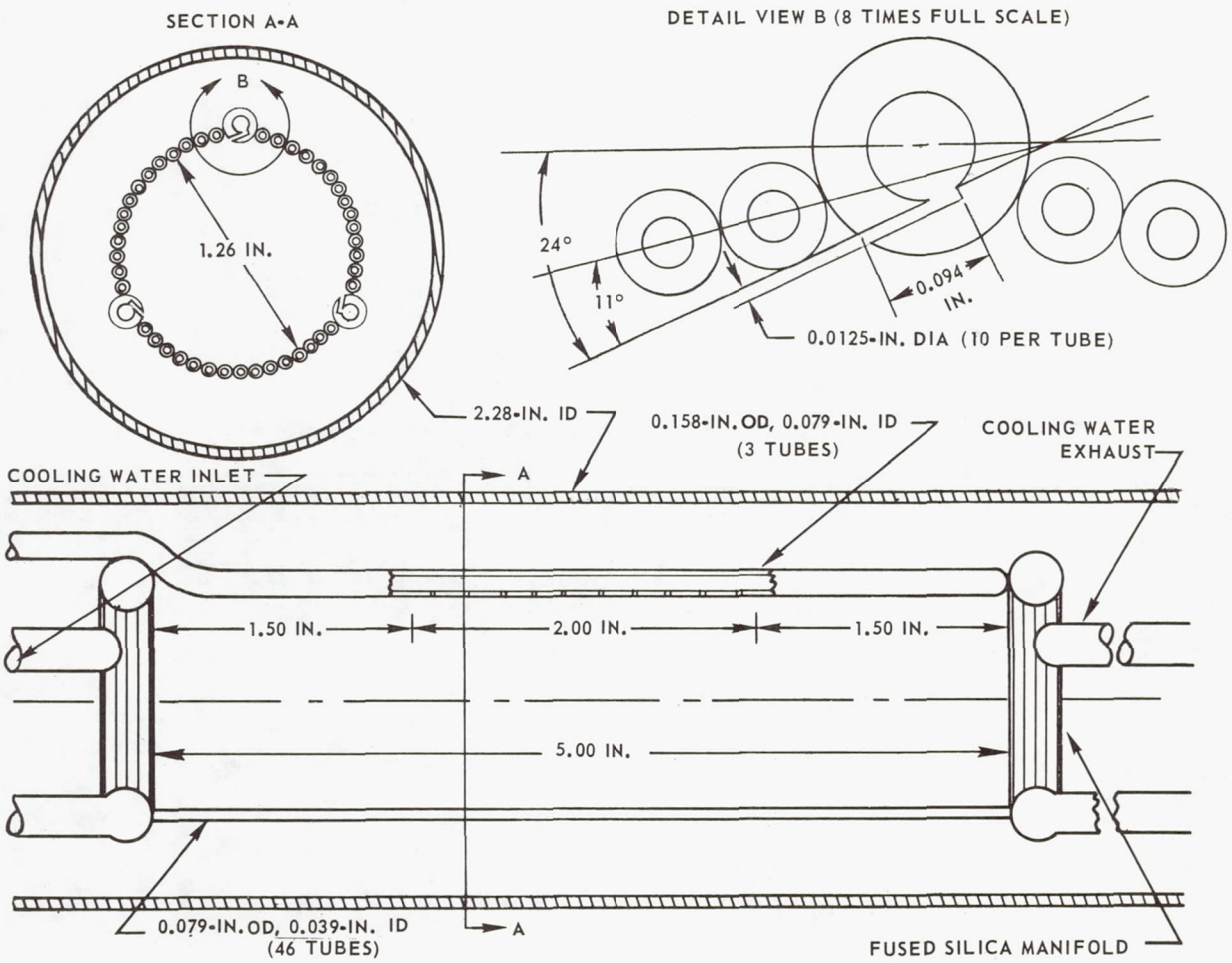

EFFECT OF DISCHARGE PRESSURE ON POWER RADIATED IN TESTS OF TRANSPARENT-WALL CONFIGURATIONS

SOLID SYMBOLS DENOTE RADIOMETER ONLY, Q_R/Q_T

OPEN SYMBOLS DENOTE RADIOMETER AND PERIPHERAL COOLING WATER, $(Q_R + Q_W)/Q_T$

FLAGGED SYMBOLS DENOTE PARTIALLY DISCOLORED AND DAMAGED MODEL

SYMBOL	RANGE OF ARGON FLOW RATE, W_A - LB/SEC	RANGE OF TOTAL DISCHARGE POWER, Q_T - KW
○ ●	0.0009 TO 0.003	7 TO 18
△ ▲	0.004 TO 0.006	18 TO 28
□ ■	0.003 TO 0.012	6 TO 24

a) END-WALL VORTEX INJECTION

b) PERIPHERAL-WALL VORTEX INJECTION

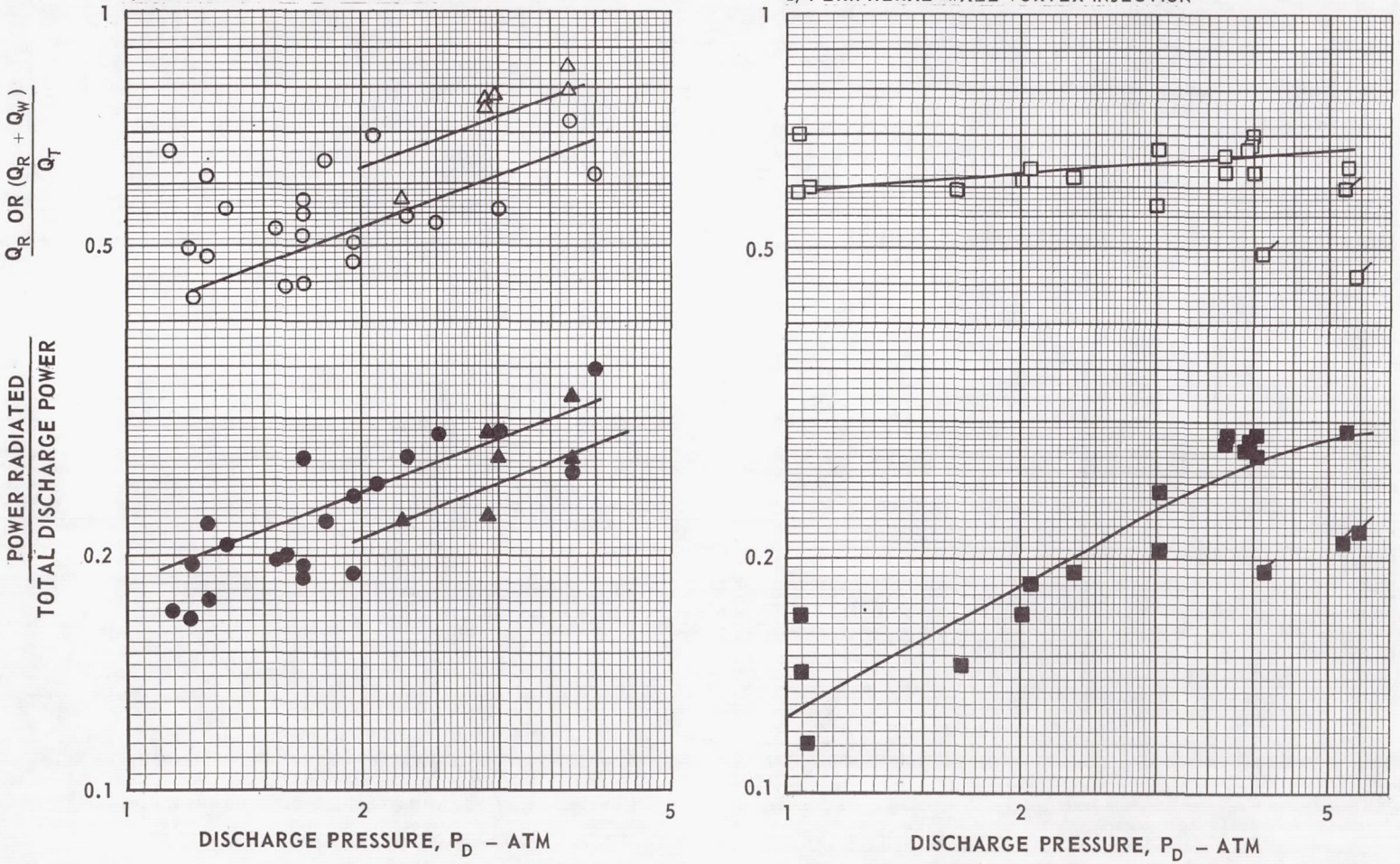

FIG. 30

EFFECT OF ARGON WEIGHT FLOW ON POWER RADIATED IN TESTS OF TRANSPARENT-WALL CONFIGURATIONS

SOLID SYMBOLS DENOTE RADIOMETER ONLY, Q_R/Q_T

OPEN SYMBOLS DENOTE RADIOMETER AND PERIPHERAL COOLING WATER, $(Q_R + Q_W)/Q_T$

FLAGGED SYMBOLS DENOTE PARTIALLY DISCOLORED AND DAMAGED MODEL

SYMBOL	RANGE OF DISCHARGE PRESSURE, P_D – ATM	RANGE OF TOTAL DISCHARGE POWER, Q_T – KW
▽ ▼	1.0 TO 1.5	8 TO 9
△ ▲	1.5 TO 2.5	12 TO 19
○ ●	2.5 TO 3.0	15 TO 28
◇ ◆	3.5 TO 4.0	17 TO 28
□ ■	1.0 TO 5.3	6 TO 24

a) END-WALL VORTEX INJECTION

b) PERIPHERAL-WALL VORTEX INJECTION

POWER RADIATED / TOTAL DISCHARGE POWER $= Q_R$ OR $(Q_R + Q_W)/Q_T$

1
0.5
0.2
0.1

0.001 0.002 0.005

0.005 0.01

ARGON WEIGHT FLOW, W_A – LB/SEC

FIG. 31

EFFECT OF TOTAL DISCHARGE POWER ON POWER RADIATED IN TESTS OF TRANSPARENT-WALL CONFIGURATIONS

SYMBOL	RANGE OF DISCHARGE PRESSURE, P_D-ATM	RANGE OF ARGON WEIGHT FLOW, W_A-LB/SEC
○ ●	1.0 TO 2.2	0.0012 TO 0.0041
△ ▲	2.2 TO 4.0	0.002 TO 0.0066
□ ■	1.0 TO 5.3	0.003 TO 0.0092

SOLID SYMBOLS DENOTE RADIOMETER ONLY, Q_R/Q_T

OPEN SYMBOLS DENOTE RADIOMETER AND PERIPHERAL COOLING WATER, $(Q_R+Q_W)/Q_T$

FLAGGED SYMBOLS DENOTE PARTIALLY DISCOLORED AND DAMAGED MODEL

a) END-WALL VORTEX INJECTION

b) PERIPHERAL-WALL VORTEX INJECTION

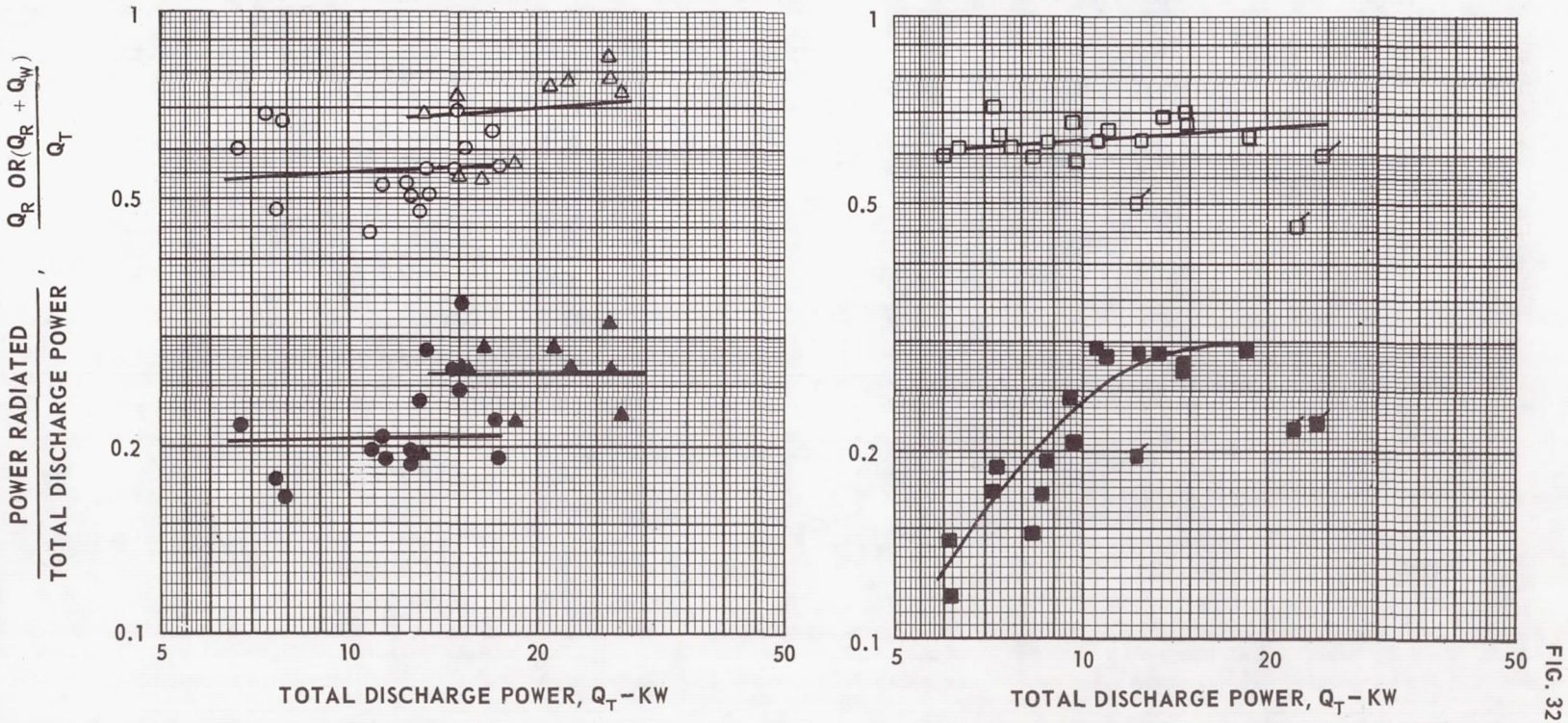

FIG. 32

PHOTOGRAPHS OF TRANSPARENT – WALL MODELS FAILED DURING TESTING

MODELS HAVING END–WALL INJECTION

a) MODEL FAILED DUE TO THERMAL STRESS

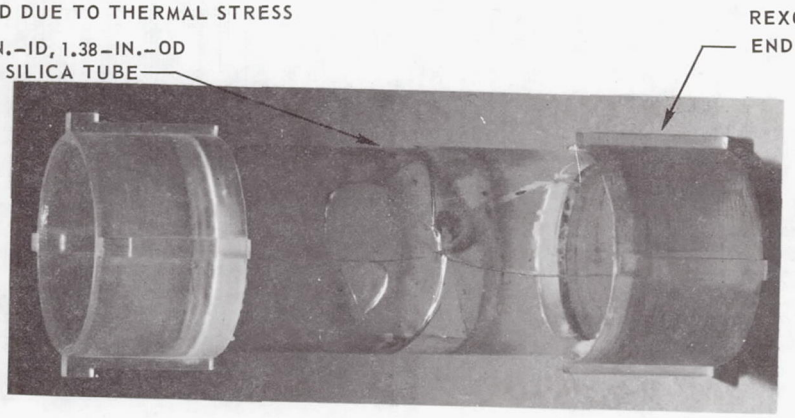

b) MODEL FAILED DUE TO POOR DIMENSIONAL QUALITY

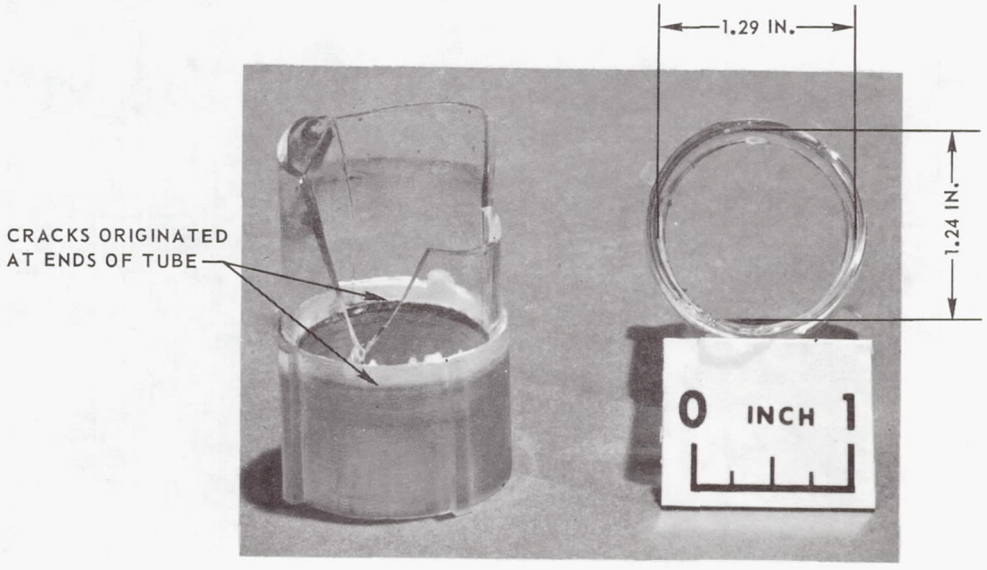

FIG. 34

TRANSPARENT – WALL MODEL WITH AXIAL COOLANT TUBES AND COPPER MANIFOLDS

SEE APPENDIX I

a) PHOTOGRAPH OF MODEL

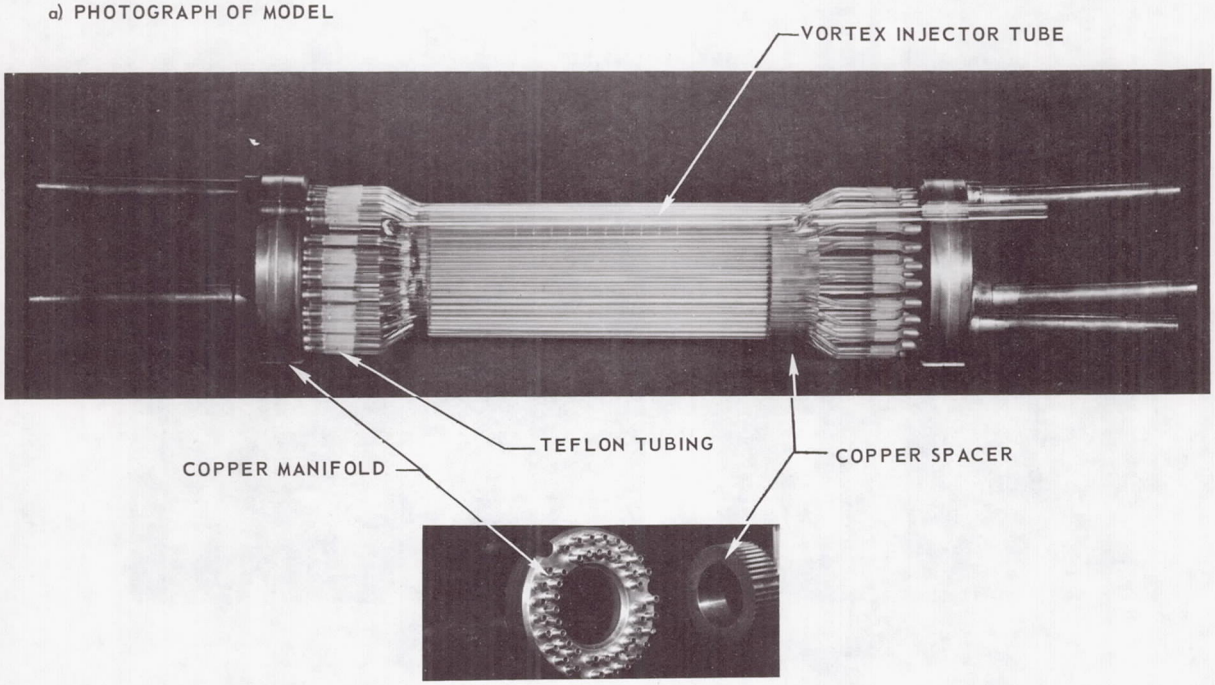

b) SKETCH OF MODEL

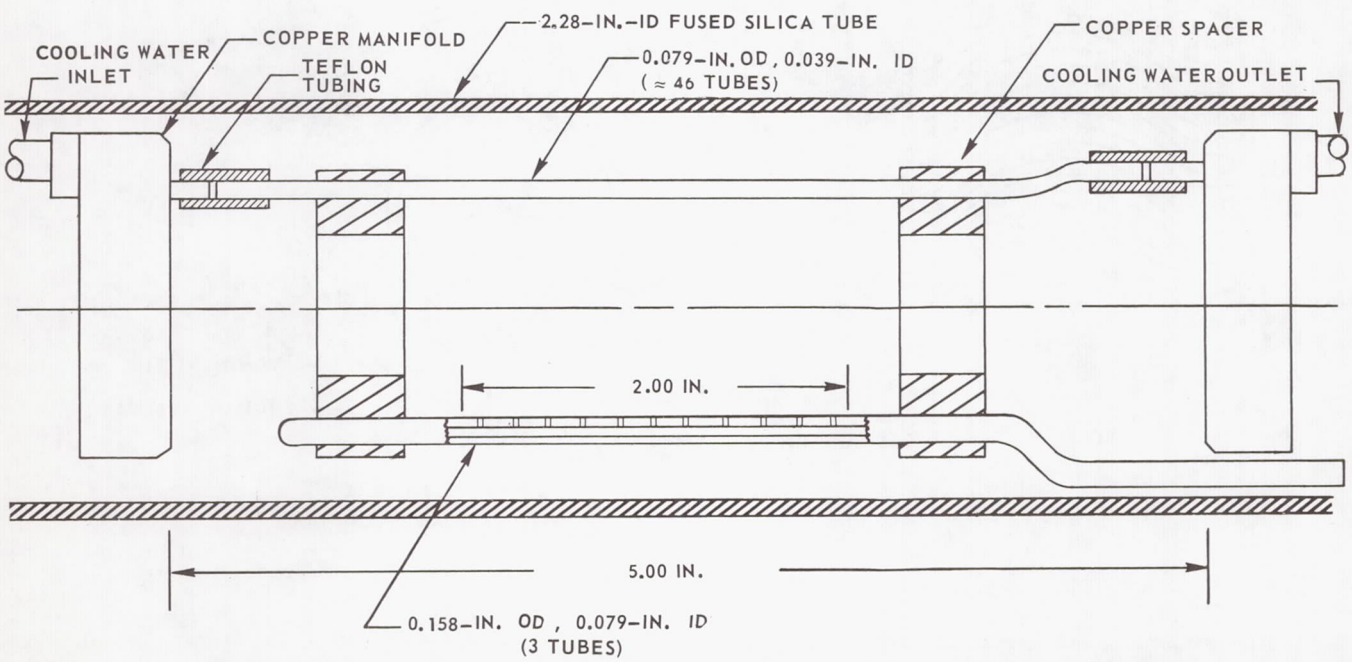

FIG. 35

TRANSPARENT-WALL MODEL WITH CIRCUMFERENTIAL COOLANT TUBES

SEE APPENDIX I

a) PHOTOGRAPH OF COIL

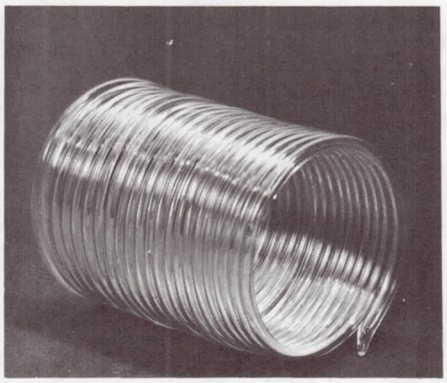

b) PHOTOGRAPH OF CUT COIL

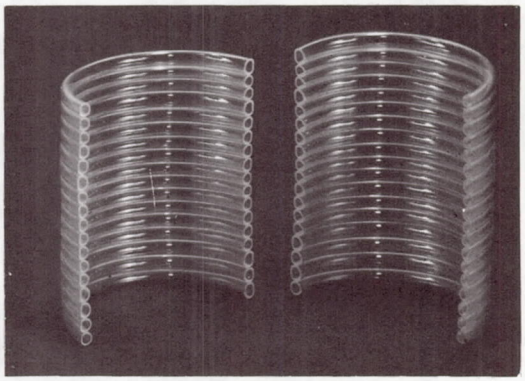

c) SKETCH OF POSSIBLE CUT AND BENT COIL

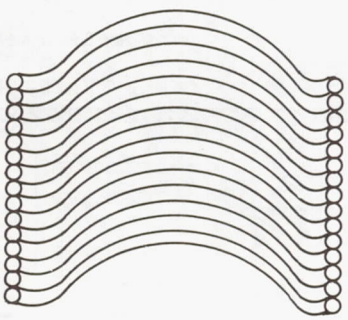

d) SKETCH OF PROPOSED MODEL CROSS-SECTION VIEW

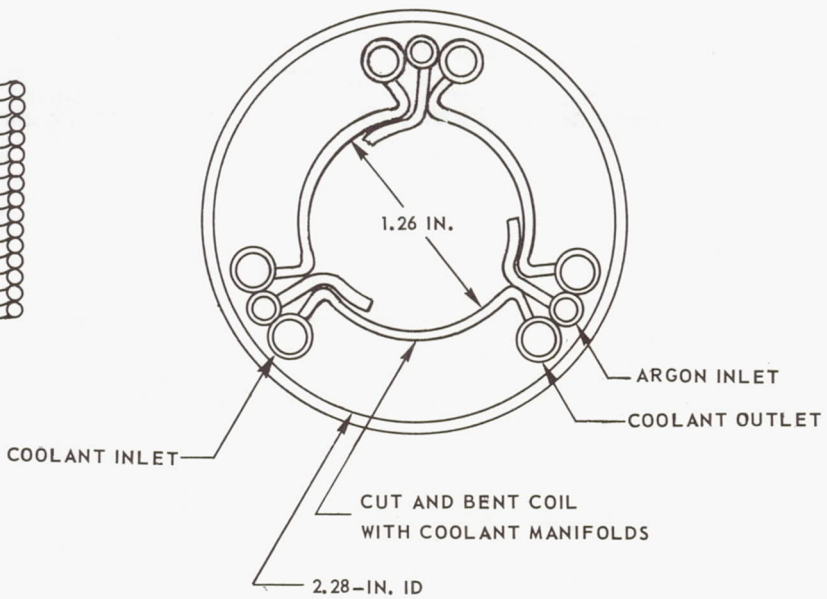

FIG. 36

PHOTOGRAPHS OF TRANSPARENT-WALL MODEL BEFORE AND AFTER HYDROSTATIC TESTING

SEE APPENDIX I

a) MODEL BEFORE TEST

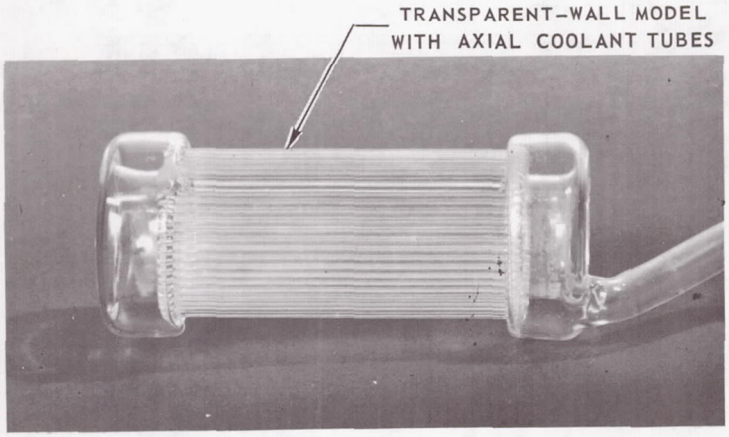

b) MODEL AFTER TEST

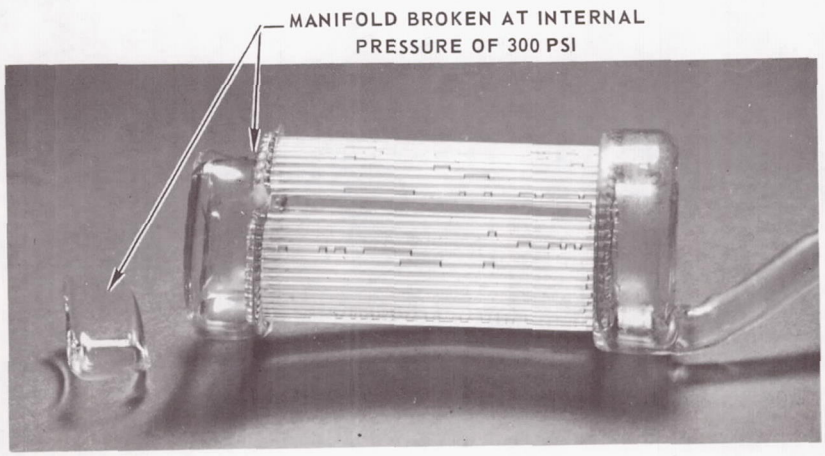

SKETCH OF SIMPLE GAS LOAD CONFIGURATION AND PHOTOGRAPH OF ARGON DISCHARGE

SEE APPENDIX II

a) SKETCH OF CONFIGURATION

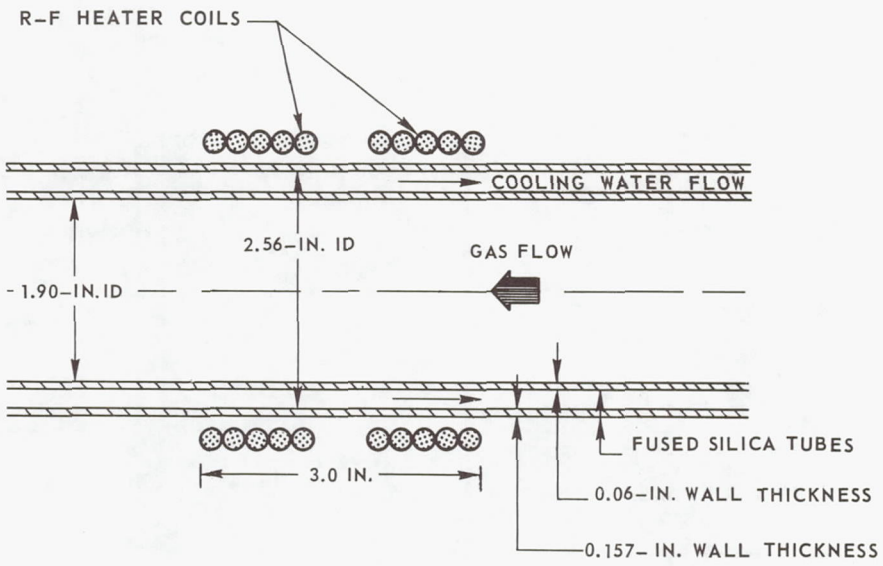

b) PHOTOGRAPH OF ARGON DISCHARGE WITH NO FLOW

PRESSURE, $P_D = 1.5$ ATM

$$\frac{\text{DISCHARGE DIAMETER}}{\text{INNER TUBE DIAMETER}} \approx 0.7$$

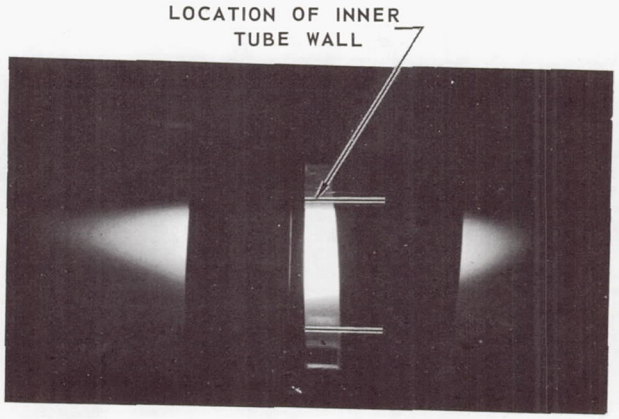

SKETCH OF SIMPLE GAS LOAD CONFIGURATION WITH SWIRL INJECTION AND PHOTOGRAPH OF ARGON DISCHARGE

SEE APPENDIX II

a) SKETCH OF CONFIGURATION

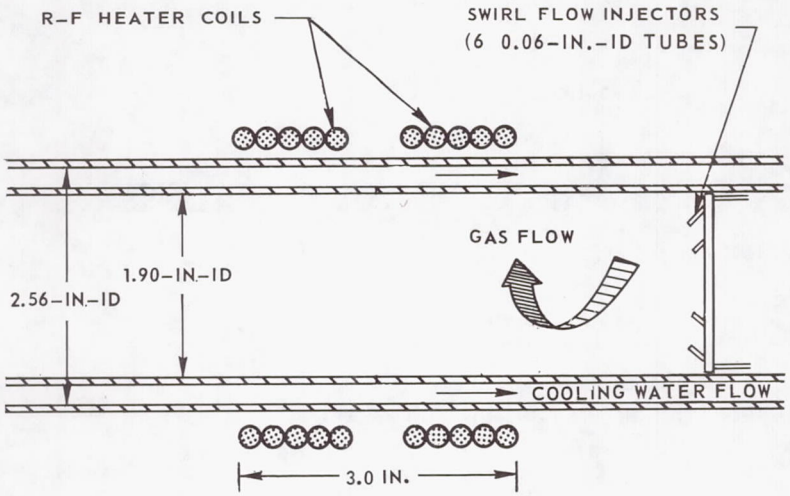

b) PHOTOGRAPH OF ARGON DISCHARGE

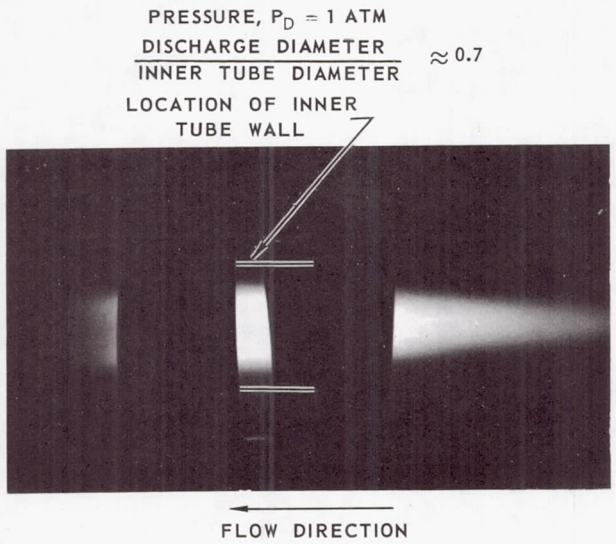

FIG. 39

SKETCHES OF VORTEX RADIANT ENERGY SOURCE CONFIGURATIONS EMPLOYED IN PRELIMINARY TESTS

SEE APPENDIX II

a) VORTEX CONFIGURATION WITH 1.75-IN.-DIA END WALLS

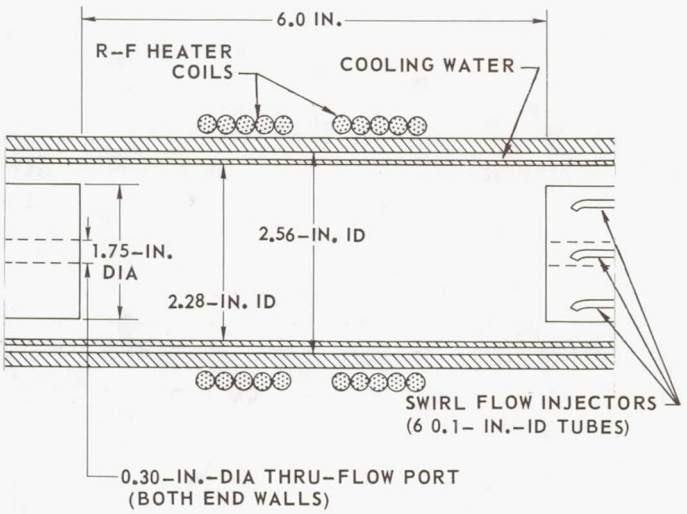

b) VORTEX CONFIGURATION WITH 0.4-IN.-DIA END WALLS

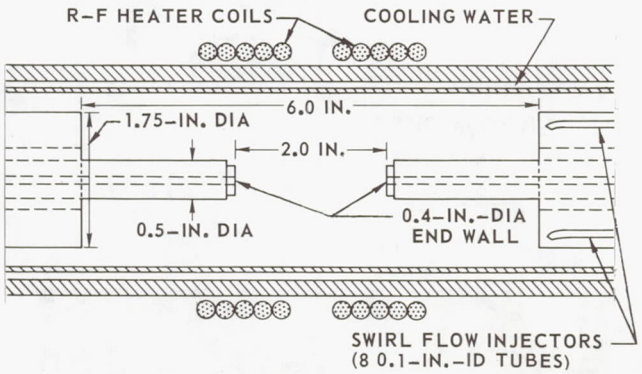

c) VORTEX CONFIGURATION WITH 0.8-IN.-DIA END WALLS

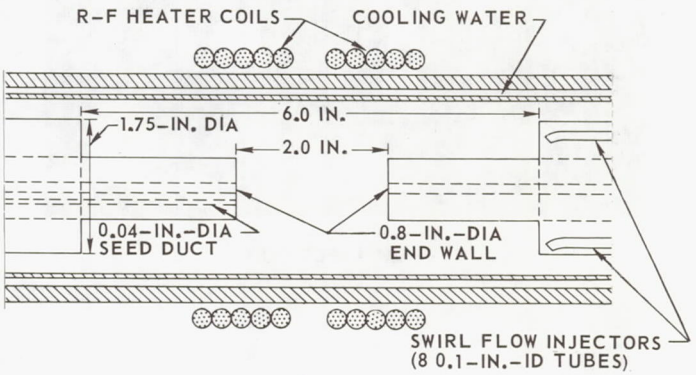

FIG. 40

PHOTOGRAPHS OF VORTEX CONFIGURATION EMPLOYED IN TESTS IN 80-KW R-F INDUCTION HEATER

SEE APPENDIX II

a) VORTEX CONFIGURATION WITH 1.125-IN.-DIA END WALLS

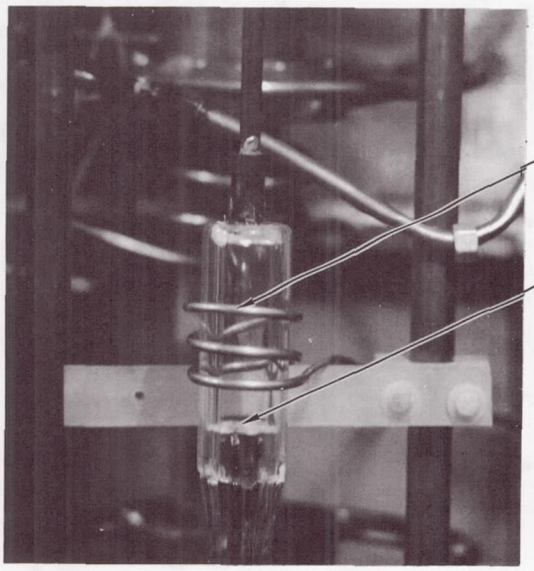

b) PHOTOGRAPH OF DISCHARGE

ARGON WEIGHT FLOW, $W_A = 0.0011$ LB/SEC

$\frac{\text{DISCHARGE DIAMETER}}{\text{INNER TUBE DIAMETER}} = 0.59$

POWER IN DISCHARGE, $Q_T = 3.4$ KW

DISCHARGE PRESSURE , $P_D = 1.0$ ATM

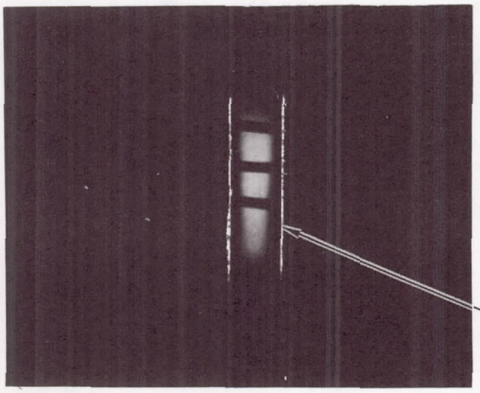

SUMMARY OF RESULTS OF TESTS EMPLOYING VORTEX CONFIGURATION WITH 1.125-IN.-DIA END WALLS

SEE APPENDIX II

FOR GEOMETRIC DETAILS OF MODEL INSTALLATION SEE FIG. 40

VORTEX TUBE RADIUS, $r_1 = 0.63$ IN.

DISCHARGE PRESSURE, $P_D = 1.0$ ATM

RADIATED POWER THROUGH PERIPHERAL WALL NOT MEASURED

SYMBOL	LENGTH OF MODEL, L-IN.	RANGE OF TOTAL DISCHARGE POWER, Q_T -KW
△	2.00	2.8-6.4
○	4.25	3.4-5.0

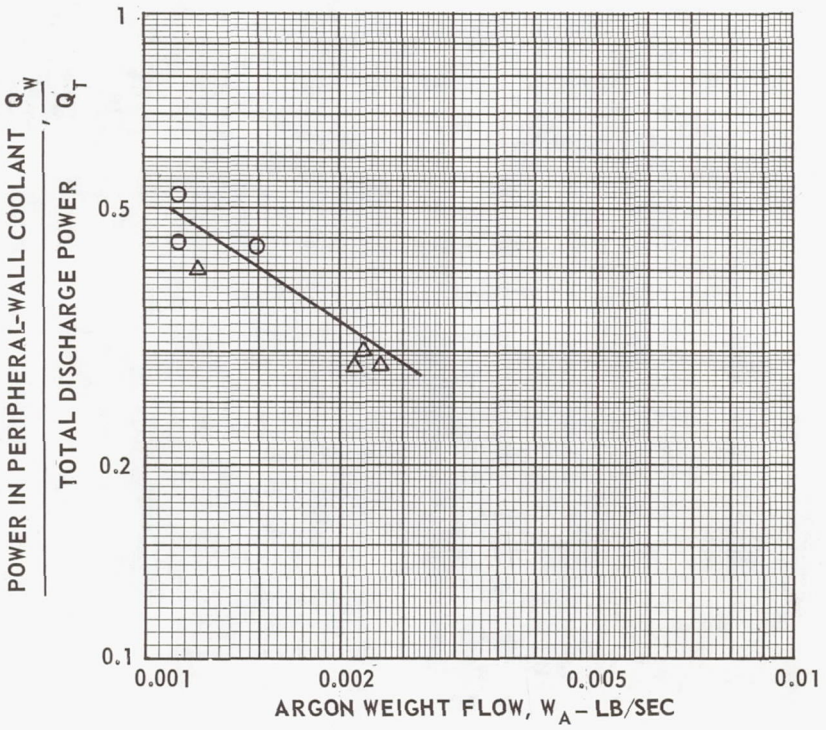

FIG. 42

SKETCHES OF MODELS EMPLOYED IN WATER VORTEX TESTS

SEE APPENDIX III

a) PERIPHERAL-WALL INJECTION MODEL

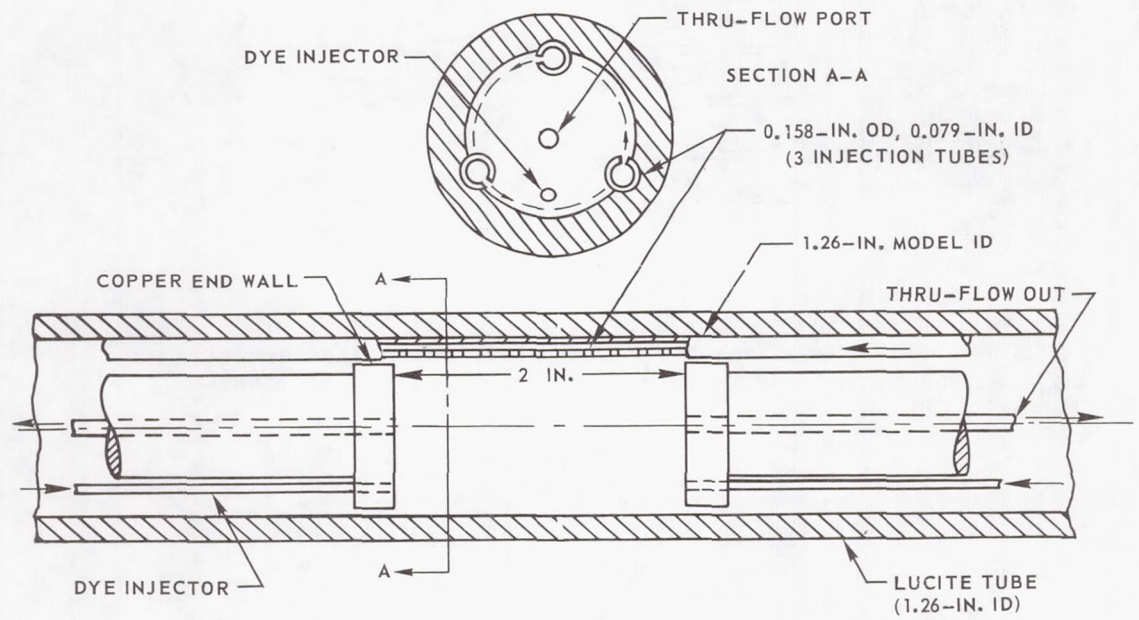

b) END-WALL INJECTION MODEL

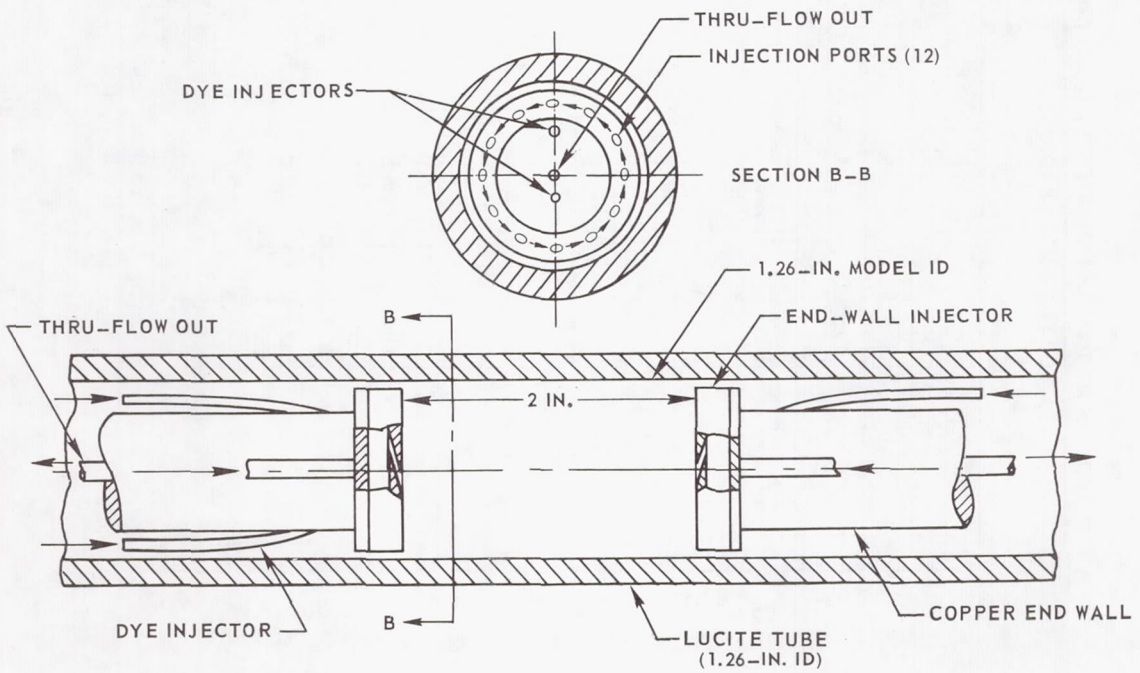

FIG. 43

EFFECT OF VORTEX INJECTION CONFIGURATION ON LOCATION OF RADIAL STAGNATION STREAMLINE FOR RADIAL – INFLOW VORTEXES

a) RADIAL – INFLOW FLOW PATTERN

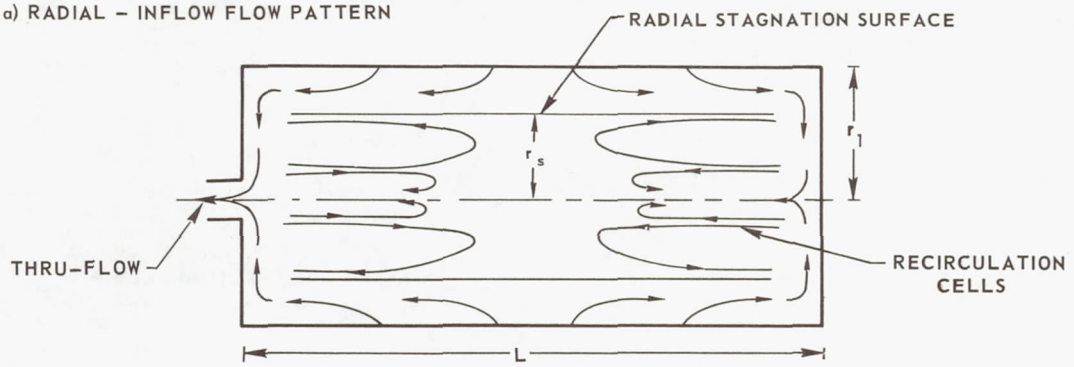

b) EFFECT OF VORTEX CONFIGURATION ON LOCATION OF RADIAL STAGNATION SURFACE (r_s MEASURED AT AXIAL MIDPLANE FROM PHOTOGRAPHS OF DYE PATTERNS)

SYMBOL	INJECTION CONFIGURATION	INJECTION AREA, A_j–SQ IN.
○	END – WALL	0.00754
△	PERIPHERAL	0.00370

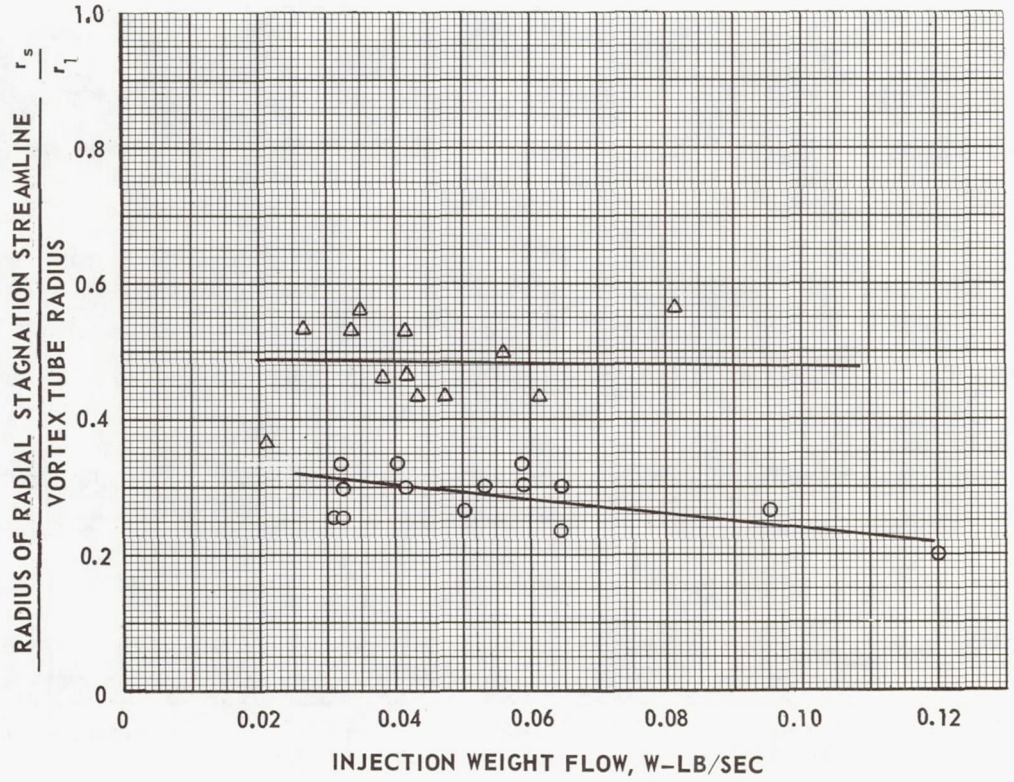

SCHEMATIC DIAGRAM OF FLOW SYSTEM IN HIGH REYNOLDS NUMBER TEST FACILITY

SEE APPENDIX IV

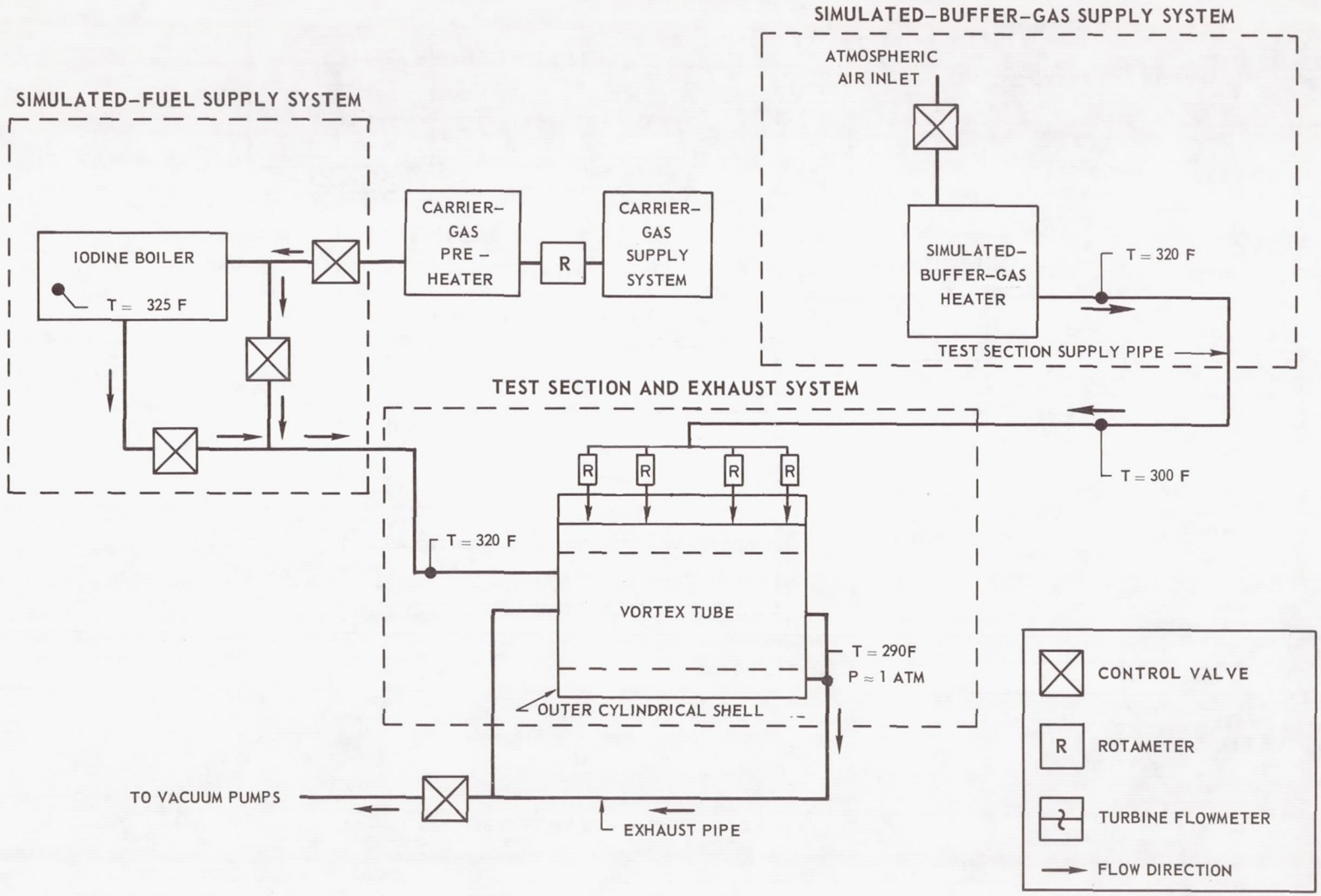

FIG. 44

SCHEMATIC DIAGRAM OF AXIAL ABSORPTOMETER

DETAILS OF FLOW NOT SHOWN
LIGHT BEAM TRAVERSES PERPENDICULAR TO PLANE OF THIS VIEW
SEE APPENDIX IV

TOP VIEW

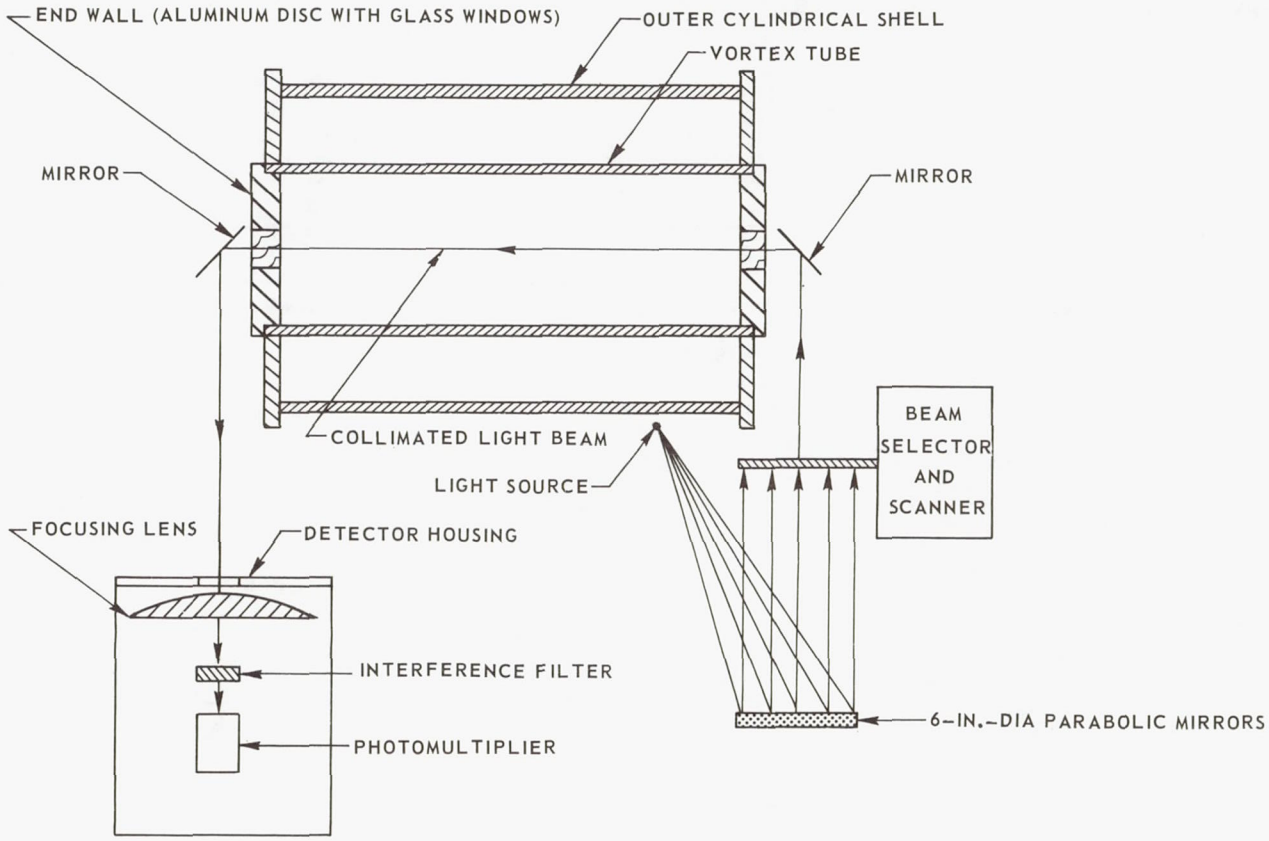

FIG. 45

GEOMETRY OF VORTEX TUBE EMPLOYED IN TESTS

SEE APPENDIX IV

a) PHOTOGRAPH OF DIRECTED-WALL-JET VORTEX TUBE

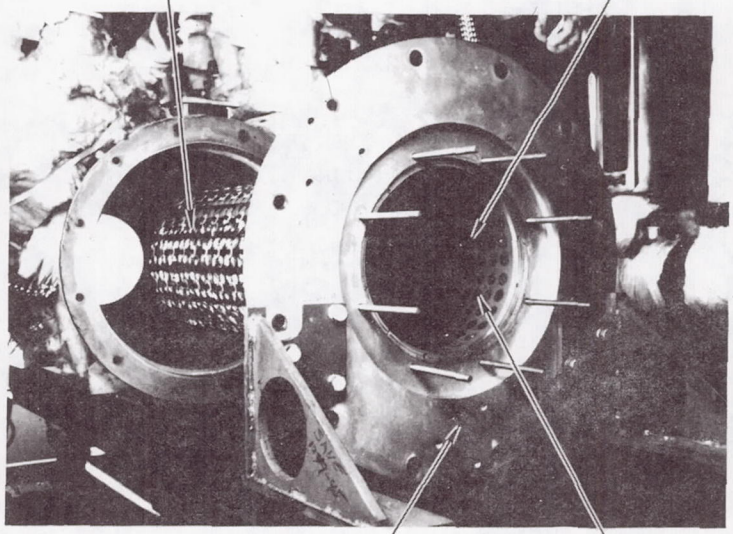

b) SKETCH OF VORTEX TUBE (ALL DIMENSIONS IN INCHES)

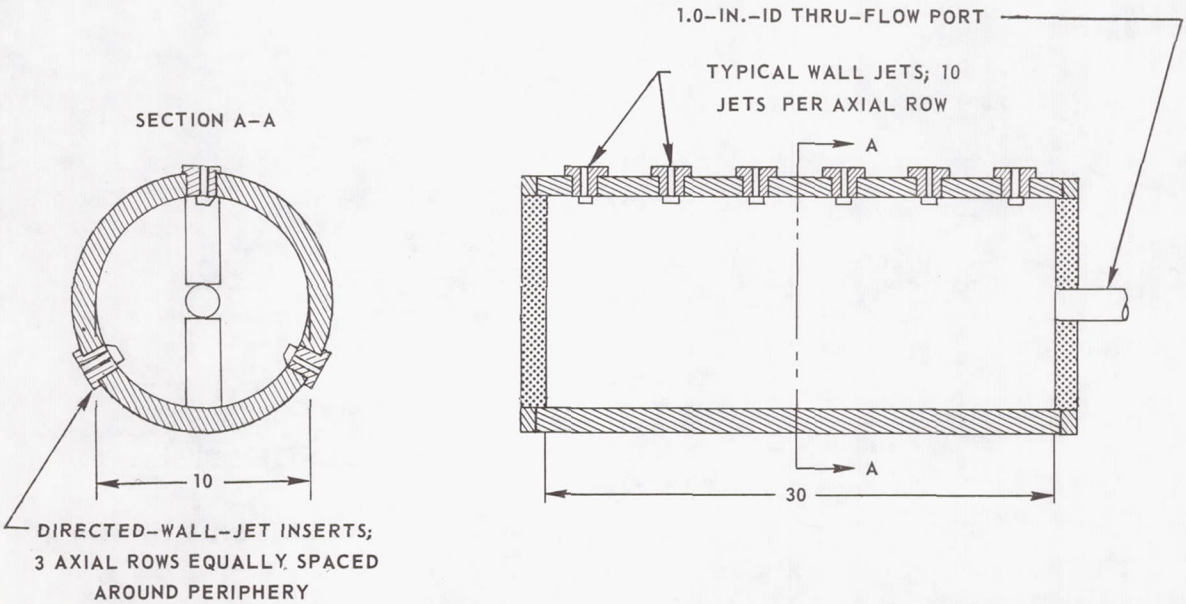

FIG. 47

DETAILS OF DIRECTED – WALL – JET INSERTS AND SIMULATED – FUEL INJECTION CONFIGURATION

SEE APPENDIX IV

ALL DIMENSIONS IN INCHES

a) DIRECTED–WALL–JET INSERTS

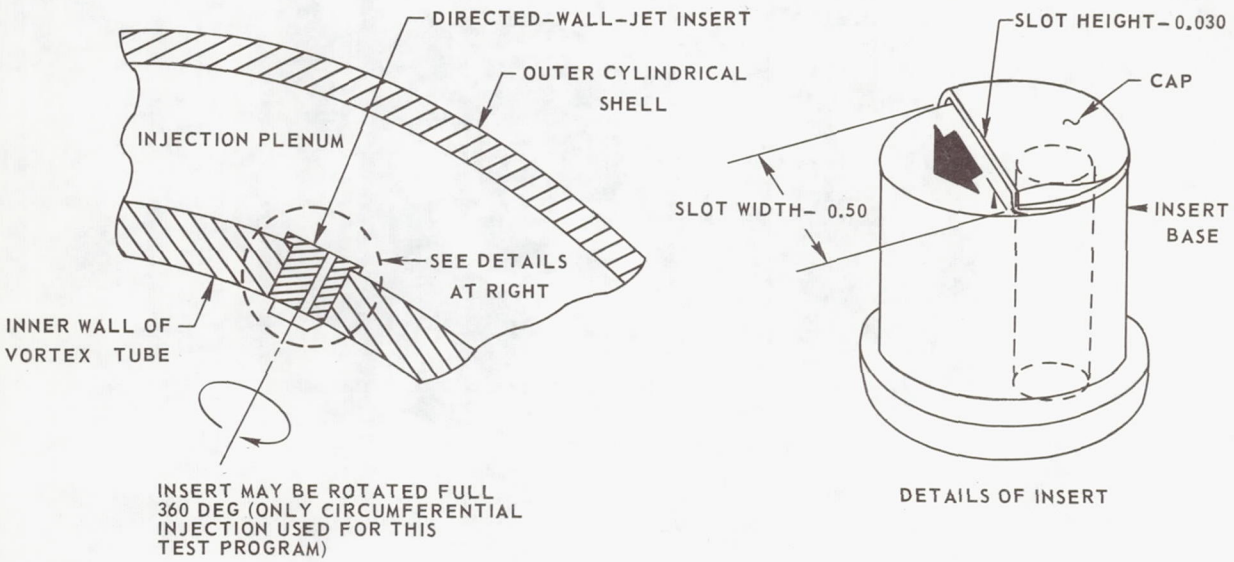

b) SIMULATED–FUEL INJECTION CONFIGURATION

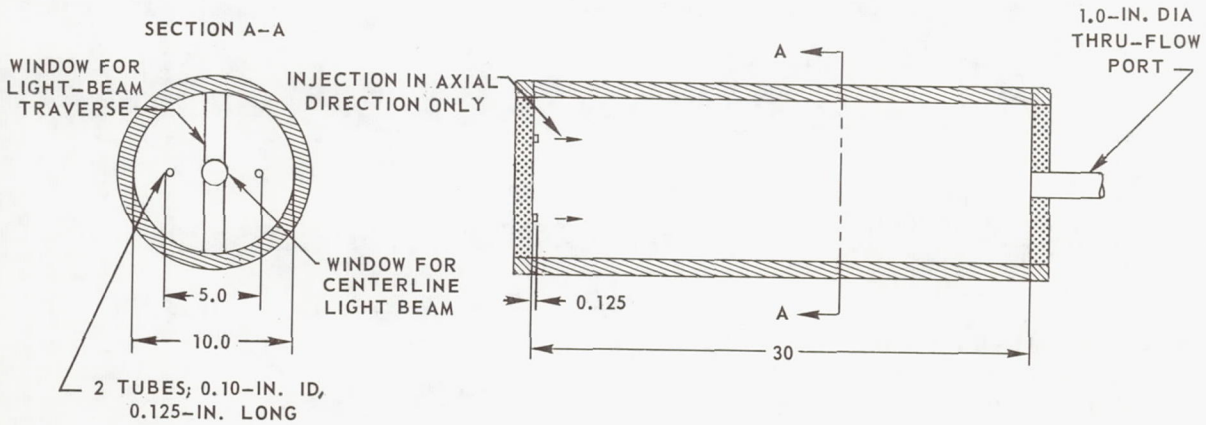

SUMMARY OF SIMULATED – FUEL CONTAINMENT RESULTS

SEE APPENDIX IV
SEE FIGS. 46 AND 47 FOR DETAILS OF CONFIGURATION
SIMULATED–BUFFER GAS DENSITY, $\rho_B \approx 0.055$ LB/FT^3

SYMBOL	SIMULATED FUEL	R_{e_r}
□	He/I_2	100
○	AIR/I_2	100
◐	AIR/I_2	200
●	AIR/I_2	360
△	SF_6/I_2	100

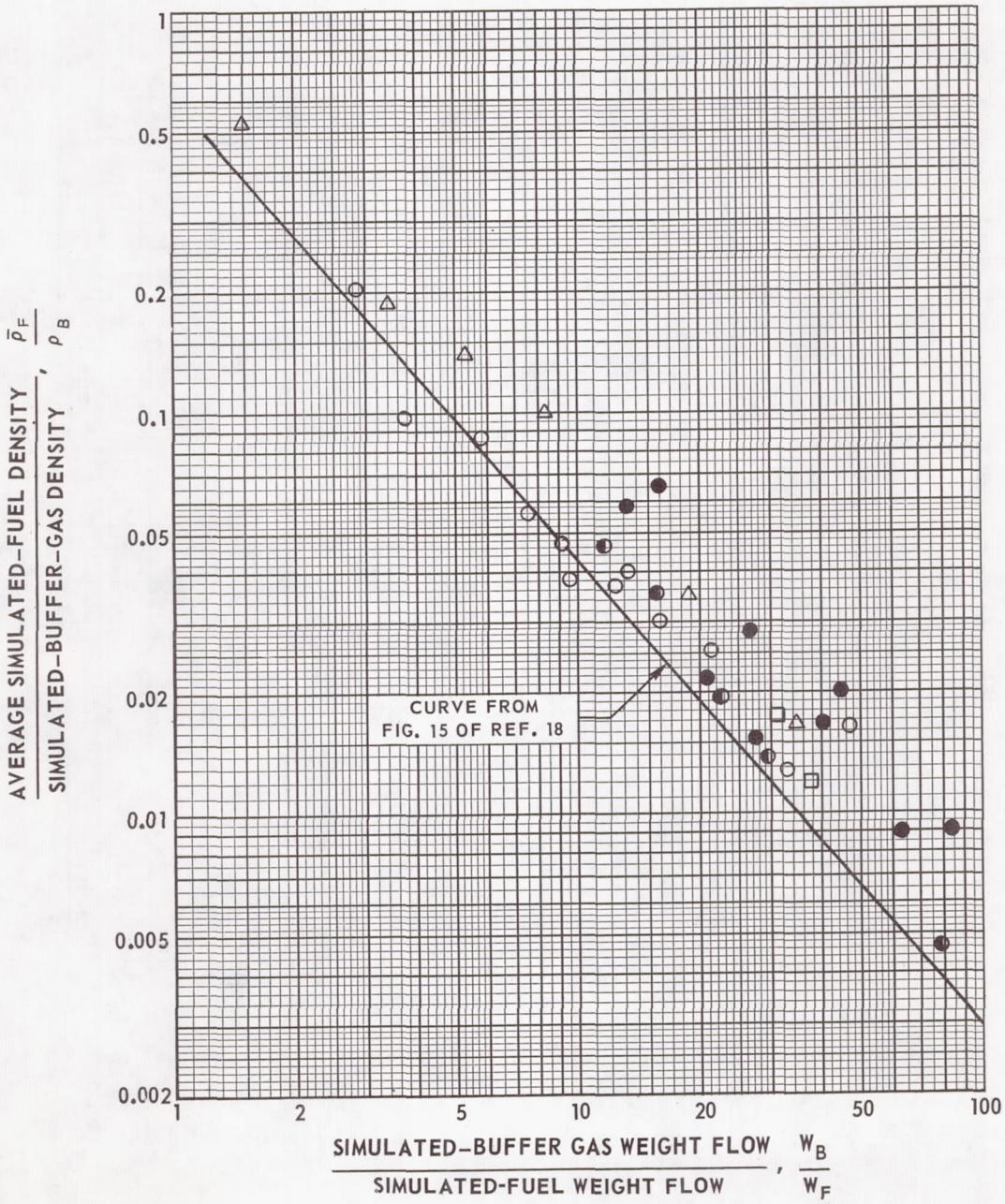

EFFECT OF RADIAL REYNOLDS NUMBER ON THE RADIAL DISTRIBUTION OF SIMULATED FUEL

SEE APPENDIX IV

SEE FIGS. 46 AND 47 FOR DETAILS OF CONFIGURATION

SIMULATED FUEL: AIR/IODINE

OPEN SYMBOLS DENOTE UPPER TRAVERSE

SOLID SYMBOLS DENOTE LOWER TRAVERSE

SYMBOL	Re_r	W_B/W_F	$(\rho V^2)_F/(\rho V^2)_B$	$\overline{P}_F$ – ATM	$\overline{\rho}_F$ – LB/FT^3
△	100	20.2	1.9	0.023	0.00137
○	100	16.1	3.1	0.024	0.00160
▷	200	20.2	2.0	0.012	0.00107
□	360	16.3	3.2	0.029	0.00217

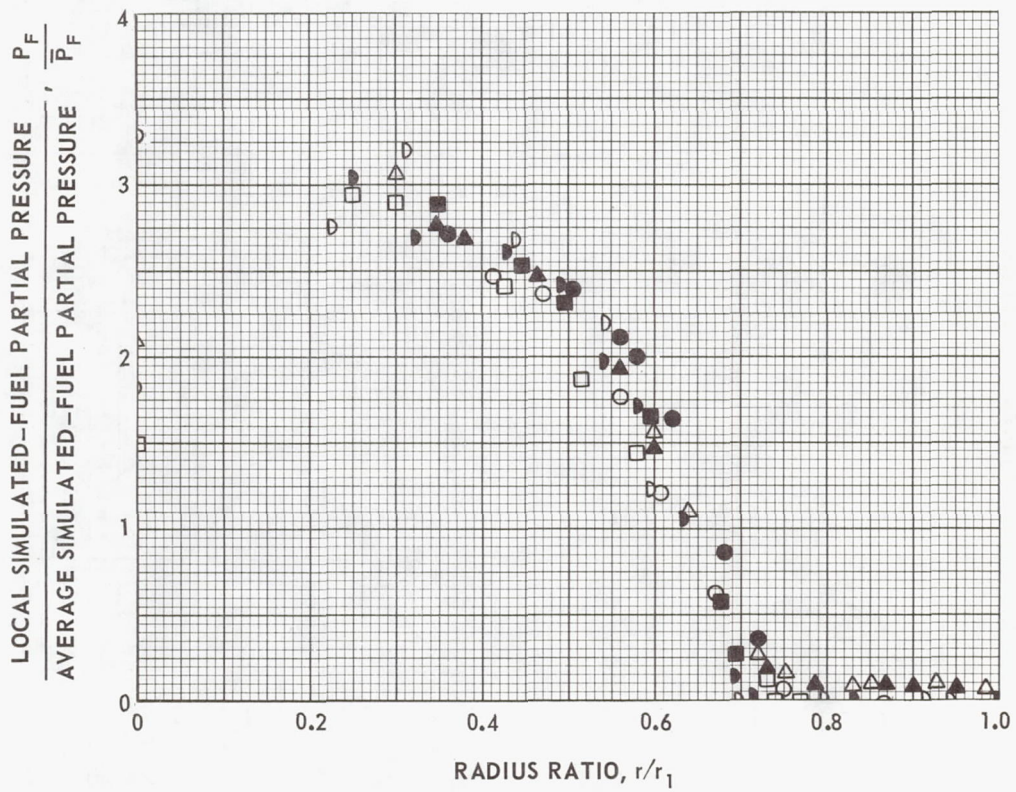

FIG. 50

RADIAL DISTRIBUTIONS OF SIMULATED FUEL OBTAINED WITH HELIUM/IODINE MIXTURE AS SIMULATED FUEL

W_B/W_F VARIED

SEE APPENDIX IV

SEE FIGS. 46 AND 47 FOR DETAILS OF CONFIGURATION

RADIAL REYNOLDS NUMBER $Re_r \approx 100$

FOR THESE DATA: $\rho_B \approx 0.055$ LB/FT^3, $P_1 \approx 1.0$ ATM, $W_B = 0.024$ LB/SEC

—— CURVE FAIRED THROUGH DATA

SYMBOL	W_B/W_F	$(\rho V^2)_F/(\rho V^2)_B$	$\overline{P}_F$ – ATM	$\overline{\rho}_F$ – LB/FT^3
△	86.0	0.6	0.050	0.00049
○	39.9	2.8	0.063	0.00064
◇	31.3	5.3	0.099	0.00092
□	21.3	10.7	0.117	0.00114

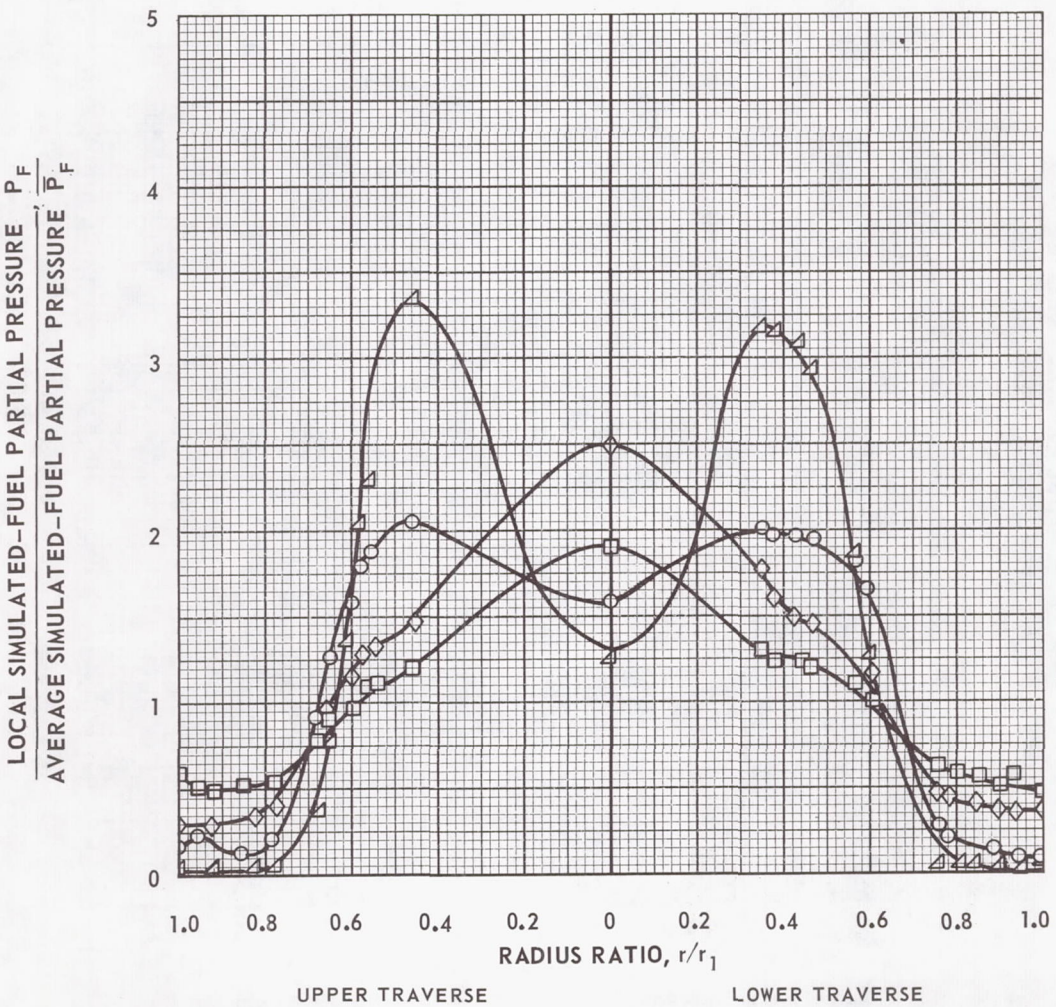

RADIAL DISTRIBUTIONS OF SIMULATED FUEL OBTAINED WITH AIR/IODINE MIXTURE AS SIMULATED FUEL

W_B/W_F VARIED

SEE APPENDIX IV

SEE FIGS. 46 AND 47 FOR DETAILS OF CONFIGURATION

RADIAL REYNOLDS NUMBER, $Re_r \approx 100$

FOR THESE DATA; $\rho_B \approx 0.055$ LB/FT^3, $P_1 \approx 1.0$ ATM, $W_B = 0.024$ LB/SEC

——CURVE FAIRED THROUGH DATA

SYMBOL	W_B/W_F	$(\rho V^2)_F/(\rho V^2)_B$	$\bar{P}_F$ – ATM	$\bar{\rho}_F$ – LB/FT^3
◇	33.5	0.7	0.014	0.00072
◁	12.6	4.9	0.032	0.00197
□	7.5	14.9	0.048	0.00218
○	5.4	24.2	0.084	0.00463

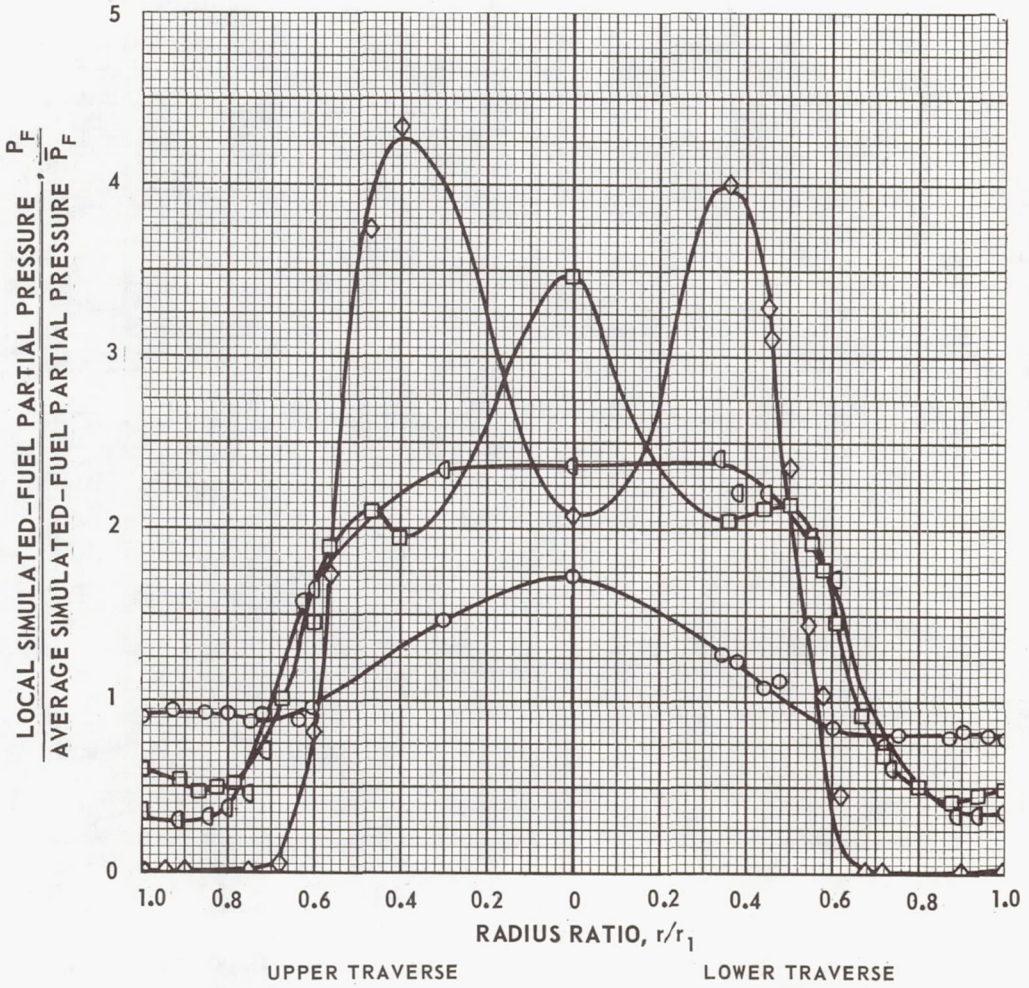

RADIAL DISTRIBUTION OF SIMULATED FUEL OBTAINED WITH SULFUR-HEXAFLUORIDE/IODINE MIXTURE AS SIMULATED FUEL

W_B/W_F VARIED

SEE APPENDIX IV

SEE FIGS. 46 AND 47 FOR DETAILS OF CONFIGURATION

RADIAL REYNOLDS NUMBER, $Re_r \approx 100$

FOR THESE DATA; $\rho_B \approx 0.055$ LB/FT^3; $P_1 \approx 1.0$ ATM, $W_B = 0.024$ LB/SEC

——— CURVE FAIRED THROUGH DATA

SYMBOL	W_B/W_F	$(\rho V^2)_F/(\rho V^2)_B$	$\overline{P}_F$ - ATM	$\overline{\rho}_F$ - LB/FT^2
△	19.4	0.5	0.008	0.0020
D	5.3	6.1	0.026	0.0076
□	2.9	20.1	0.038	0.0112
◇	1.5	76.0	0.107	0.0307

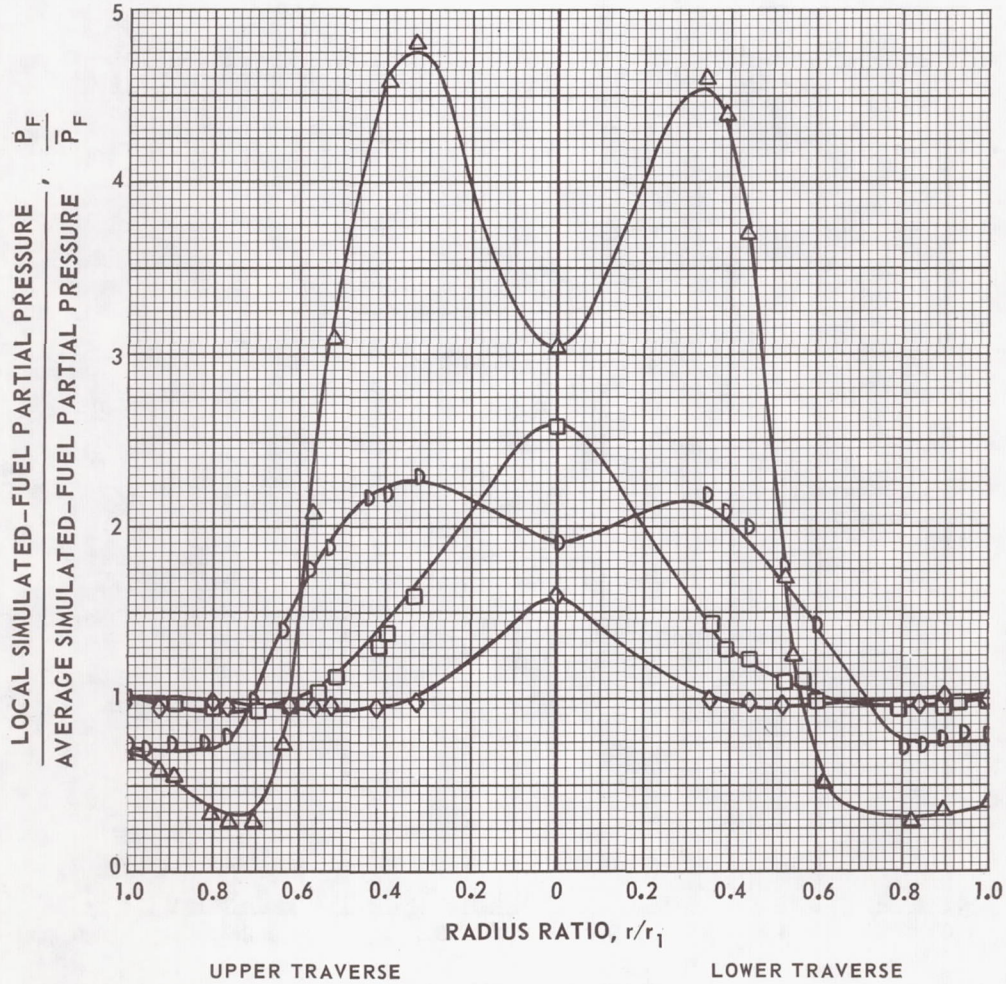

RADIAL DISTRIBUTIONS OF SIMULATED FUEL FOR LOW SIMULATED-FUEL INJECTION DYNAMIC PRESSURES

W_B/W_F VARIED TO MAINTAIN $(\rho V^2)_F/(\rho V^2)_B$ APPROXIMATELY CONSTANT

SEE APPENDIX IV

SEE FIGS. 46 AND 47 FOR DETAILS OF CONFIGURATION

RADIAL REYNOLDS NUMBER, $Re_r \approx 100$

FOR THESE DATA: $\rho_B \approx 0.055$ LB/FT^3, $P_1 \approx 1.0$ ATM, $W_B = 0.024$ LB/SEC

OPEN SYMBOLS DENOTE UPPER TRAVERSE

SOLID SYMBOLS DENOTE LOWER TRAVERSE

SYMBOL	$(\rho V^2)_F/(\rho V^2)_B$	SIMULATED FUEL	W_B/W_F	$\overline{P}_F$ – ATM	$\overline{\rho}_F$ – LB/FT^3
□	0.6	He/I_2	86.0	0.050	0.00049
○	0.7	AIR/I_2	33.5	0.011	0.00072
△	0.5	SF_6/I_2	19.3	0.008	0.00200

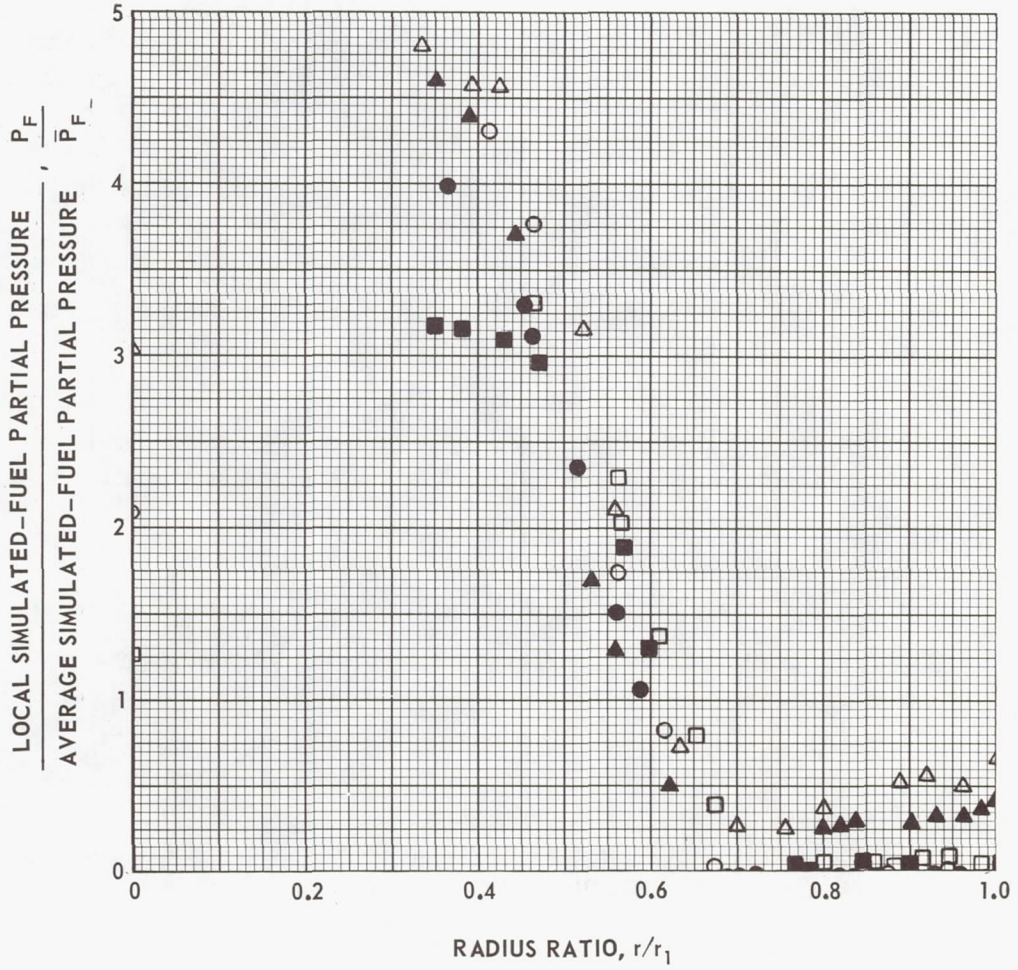

RADIAL DISTRIBUTION OF SIMULATED FUEL FOR HIGH SIMULATED-FUEL INJECTION DYNAMIC PRESSURES

W_B/W_F VARIED TO MAINTAIN $(\rho V^2)_F/(\rho V^2)_B$ APPROXIMATELY CONSTANT

SEE APPENDIX IV

SEE FIGS. 46 AND 47 FOR DETAILS OF CONFIGURATION

RADIAL REYNOLDS NUMBER, $Re_r \approx 100$

FOR THESE DATA; $\rho_B \approx 0.055$ LB/FT^3, $P_1 \approx 1.0$ ATM, $W_B = 0.024$ LB/SEC

OPEN SYMBOLS DENOTE UPPER TRAVERSE

SOLID SYMBOLS DENOTE LOWER TRAVERSE

SYMBOL	$(\rho V^2)_F/(\rho V^2)_B$	SIMULATED FUEL	W_B/W_F	$\overline{P}_F$ – ATM	$\overline{\rho}_F$ – LB/FT^3
□	5.8	He/I_2	26.6	0.071	0.00082
○	4.9	AIR/I_2	12.6	0.032	0.00197
△	6.1	SF_6/I_2	5.3	0.026	0.00758

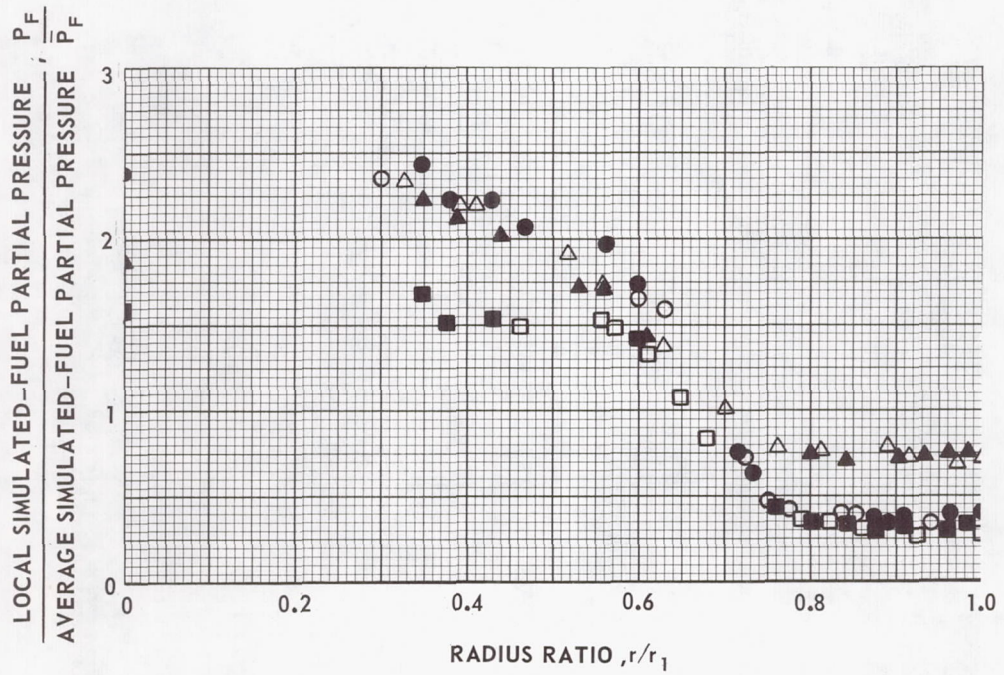

EFFECT OF SIMULATED-FUEL MOLECULAR WEIGHT ON THE AMOUNT OF SIMULATED FUEL NEAR THE VORTEX TUBE PERIPHERAL WALL

SEE APPENDIX IV

SEE FIGS. 46 AND 47 FOR DETAILS OF CONFIGURATION

——— CURVE FAIRED THROUGH DATA

SYMBOL	SIMULATED FUEL	Re_r
□	He/I_2	100
○	AIR/I_2	100
◐	AIR/I_2	200
●	AIR/I_2	360
△	SF_6/I_2	100

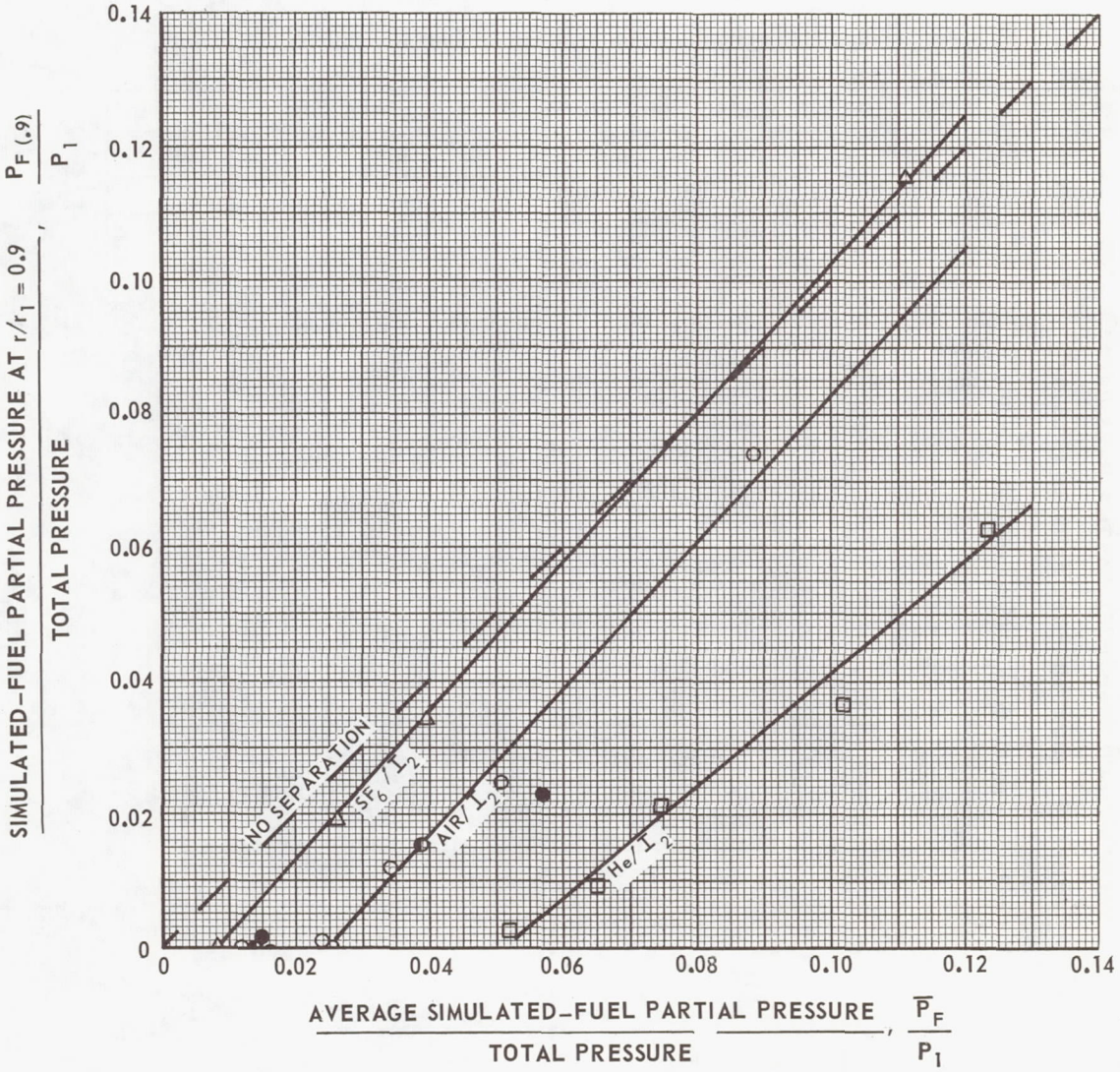

NASA-Langley, 1969 —— 22 CR-1311